SOVIET ATOMIC ENERGY

АТОМНАЯ ЭНЕРГИЯ
(ATOMNAYA ÉNERGIYA)

TRANSLATED FROM RUSSIAN

SOVIET ATOMIC ENERGY

An agreement with the Copyright Agency of the USSR (VAAP) makes available both advance copies of the Russian journal and original glossy photographs and artwork. This serves to decrease the necessary time lag between publication of the original and publication of the translation and helps to improve the quality of the latter. The translation began with the first issue of the Russian journal.

CONSULTANTS BUREAU, NEW YORK AND LONDON

SOVIET ATOMIC ENERGY

A translation of *Atomnaya Énergiya*

February, 1985

Volume 57, Number 2   August, 1984

CONTENTS

Engl./Russ.

CONTENTS

(continued)

Engl./Russ.

The Russian press date (podpisano k pechati) of this issue was 7/26/1984.
Publication therefore did not occur prior to this date, but must be assumed
to have taken place reasonably soon thereafter.

ARTICLES

AN EXPERIMENTAL STUDY OF EMERGENCY COOLING CONDITIONS IN RBMK

REACTORS ON LOAD DISCONNECTION

V. N. Smolin, V. I. Esikov, V. P. Shishov,   UDC 621.039.524.4
S. P. Kuznetsov, and V. S. Grigor'ev

When the internal equipment in a nuclear power station is deprived of current, the main circulation pumps (MCP) stop along with the feed pumps (FP), while the emergency shutdown (ES) equipment operates and the automatic shutoff valves ahead of the turbines are closed, which causes the pressure to increase and the safety valves to open. Then the pressure in the loop begins to fall, and the safety valves should close. After about 3 min, the emergency feed pumps (EFP) are switched on. It has been found with a simulation system and checked on the reactor that stable conditions are then set up in the loop by natural circulation (NC), and cooling the core does not cause any complications.

However, if one or more of the safety valves do not close properly, the pressure in the loop will continue to fall, and the rate of fall and the final value are dependent on the degree to which the safety valves fail to close. The rate of fall and the extent of the pressure fall influence the circulation parameters and the fuel-element cooling conditions, and the extent of these effects is examined here. Because it is very difficult to make analytical calculations for such conditions, one needs experiments on models. A test model for the RBMK has been built at the Power Engineering Research and Development Institute (V. N. Smolin et al., Voprosy Atomnaya Nauki i Tekhniki, Ser. Reaktorostroenie, Issue 1(8), 3 (1974)). This simulates closely the forced multiple circulation loop (FMCL) in a reactor, including the positions at the start and end of the hydraulic system and the main equipment. This facility provides hydraulic resistances and coolant circulation times in the incoming and outgoing pipes corresponding to those in the actual reactor. The upper and lower positions in the distributing group collectors (DGC) are simulated by means of appropriate loop sections. The volume and surface of the separator per fuel element are similar in the model to those in the reactor.

Figure 1 gives the cross sections of the loops in the model and reactor in relation to the relative loop length per fuel element (the experimental assembly contained seven heated rods). The model retained virtually the same relative loop volume per fuel element as in the reactor (0.045 and 0.044 m^3, respectively). The height distributions of this volume were also identical. The test methods involved reproducing the operations and circulation conditions in the model with the maximum possible similarity to the actual processes.

The initial state was that of stationary NC at a pressure of about 7.0 MPa, since the previous changes in loop parameters do not influence the subsequent processes. We also recorded the coolant flow rate through the experimental channel (EC), the feedwater flow rate, the pressure and level in the separator, the EC power, the coolant temperatures at the inlet and outlet to the heat-production zone, the temperatures of the fuel-element simulators in the EC, and the pressure differences across components of the circulation loop.

The model was used to examine emergency cooling conditions not only by means of EC when the feedwater supply to the separator is restored but also by means of forced circulation in a direct-flow scheme with the feedwater supplied directly to the DGC. To define criteria and parameters governing the occurrence of hazardous conditions, the restored flow rate for the feedwater was different from that provided by the EFP in certain experimenta. The end of the state with NC was taken as the time when the working conditions stabilized with a given final pressure in the separator and normal cooling in the heat-production zone or the point of fuel-element overheating. The purpose of the NC experiments was to determine the final pressure and the other circulation parameters for various rates of pressure reduction leading to fuel-element overheating. The end of the state with forced circulation was taken as the instant when the heat-production zone was cooled below the saturation temperature with the given rate

507
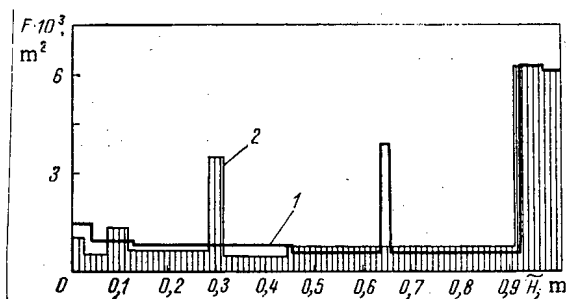
Fig. 1. Comparison of the cross sections of the model (1) and reactor (2) per fuel element by reference to the reduced height.
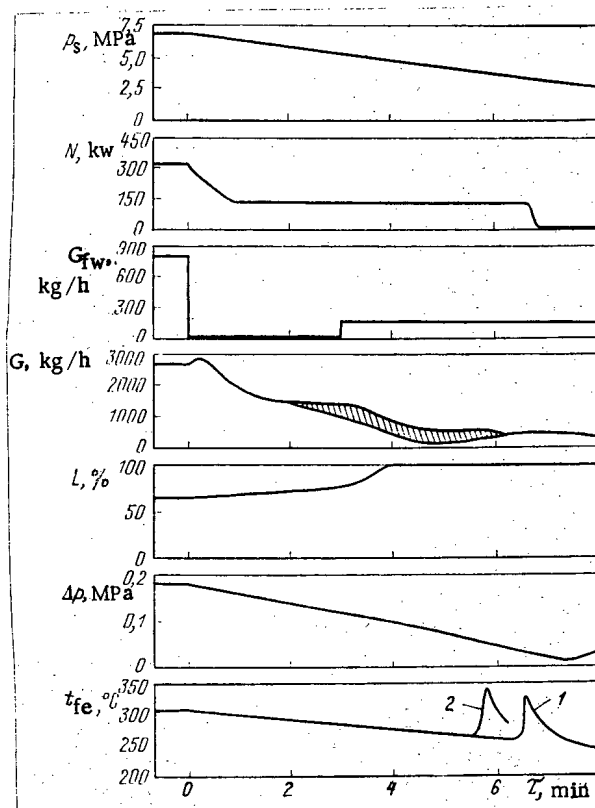
Fig. 2. Change in parameters in emergency cooling of the heat-production zone: 1) lower position of the DGC; 2) upper position of the DCG; p_s) pressure in separator; N) channel power; G_{fw}) feedwater flowrate; G) circulation flow rate; L) level in separator; Δp) pressure difference in outlet section; t_{fe}) fuel-element temperature; and the hatched region represents flow-rate pulsations.

of pressure fall and given feedwater flow rate or the instant of fuel-element overheating. The purpose of the experiments in the second method was to determine the minimum permissible pressure that does not lead to disruption of the normal cooling in the heat-production zone as affected by the reduction rate as coolant circulates from the EFP.

The initial state was always the same in all the experiments: the stationary state of NC with a pressure of 6.7 MPa in the separator, power 0.3 of nominal, average coolant temperature at the inlet to the heat-production zone 270°C, and coolant flow rate 0.35 of the nominal value. The average pressure reduction rate was 0.2-1.5 MPa/min, while the final value of the pressure was 0.68-4.8 MPa. The power was reduced to 0.1 of the nominal value. At the instant when the power was reduced and the pressure began to fall, the feedwater supply to the loop was halted, and then after 3 min it was restored with a flow rate of 0.1 of the nominal value.

Fig. 3

Fig. 4
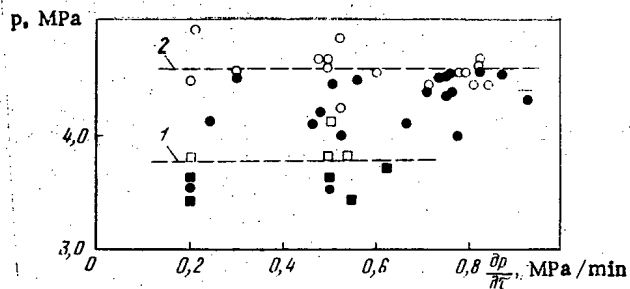
Fig. 3. Dependence of final pressure in the separator corresponding to normal cooling in the heat-production zone (○ and □) or fuel-element overheating (● and ■) on pressure reduction rate; ○ , ●) upper position of DGC; □ , ■) lower position of DGC; dashed line) limiting pressures for lower position of DGC (1) and upper position (2).
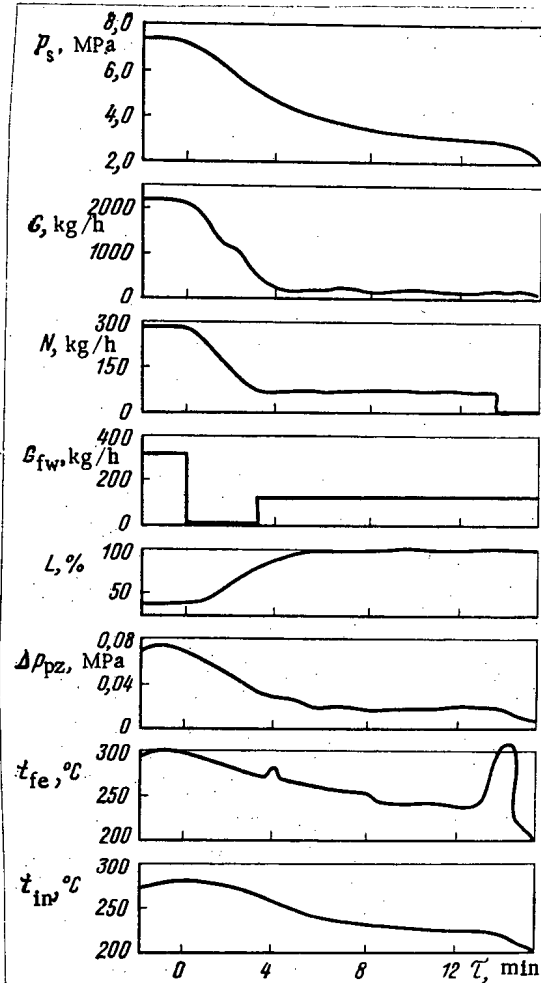
Fig. 4. Parameter variation in emergency cooling of the heat-production zone by forced circulation from the ECP with feedwater supplied to the DGC: t_{in}) temperature at the inlet to the zone, Δp_{pz}) pressure difference in the heat-production zone; for other symbols, see Fig. 2.

Figure 2 shows the typical behavior of the parameters during the transient states in NC accompanied by fuel-element overheating. When the feedwater is supplied with a flow rate close to the output of the ECP, fuel-element overheating sets in at the same separator pressure, no matter what the rate of pressure reduction. However, the final pressure is dependent on the FMCL scheme: It was 4.5 MPa with the upper position of the DGC or 3.8 MPa with the lower one (Fig. 3).

The experiments showed that if the loop is supplied with feedwater in an amount greater than that from the ECP, the final pressure is reduced. If the feedwater is supplied at a flow rate sufficient to maintain the pressure difference in the outlet part no less than 12 m of water column (this is close to the nominal feedwater flow rate in the model as reckoned for 100% reactor power), then a stable NC condition is set up in the loop, which does not lead to deviation from the normal cooling in the heat-production zone as the pressure falls in the range examined.

As the hydraulic system in the model simulates the FMCL closely, the actual changes in NC parameters on emergency cooling should be analogous and the experimental results should be

509

Fig. 5

Fig. 6
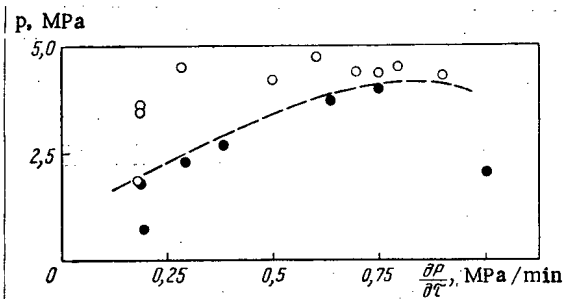
Fig. 5. Dependence of the minimum permissible pressure in the separator on **emergency cooling** by the supply of feedwater from the ECP to the DGC as affected by pressure reduction rate: ○) state with normal cooling in the heat-production zone; ●) state with fuel-element overheating.
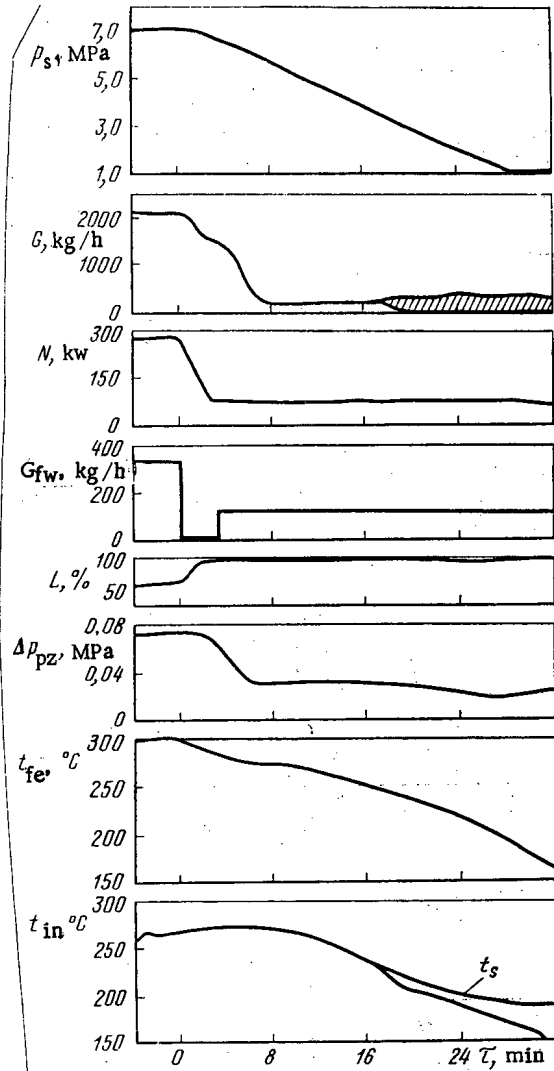
Fig. 6. Parameter variation in emergency cooling in the heat-production zone by forced circulation from the ECP with feedwater supply to the DGC. See Fig. 2 for symbols.

transferable directly to the reactor. To confirm this conclusion, we determined the separator filling times in the model and on the reactor, since this time is a decisive factor in these processes. We took a condition in which the pressure fell at 0.5 MPa/min (Fig. 2). With the coolant flow rate corresponding to the initial period under these conditions, the saturated water from the separator filled all the outlet and inlet sections, and the level in the separator began to rise at the end of the third minute. We determined the steam generation rate due to spontaneous boiling and the rate at which the steam was removed from the loop, and these data were used to estimate the rate at which the separator filled with water. The calculated separator filling time was 95 sec for the model at a pressure of 5.2 MPa, while the values for the reactor were 95 sec and 5.1 MPa, so there is good agreement between these values and also with the experimental data.

Therefore, if the pressure in the RBMK circulation loop falls below the saturation pressure because the safety **valves** fail to close and the loop is receiving an inadequate feedwater supply, then the coolant boils in the outlet part, which causes the separator to overfill,

510
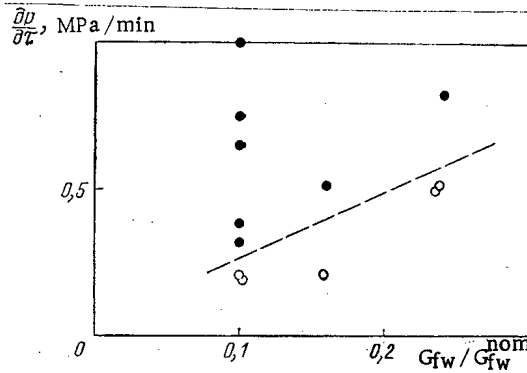
Fig. 7. Dependence of the permissible pressure reduction rate on the feedwater flow rate supplied to the DGC: ○) condition with normal cooling in the heat-production zone; ●) condition with fuel-element overheating.

while coolant is lost from the loop, and consequently there is a reduction in the NC flow rate through the core, while the fuel elements may overheat. To prevent this, it is necessary to supply the loop at a certain instant with water in an amount sufficient to maintain a heat of not less than 12 m of water column in the outlet pipe.

We examined the core cooling by forced circulation in the same sequence. At 3 min after the simulation of the emergency, which corresponded to power reduction and pressure fall at a given rate, feedwater was supplied directly to the DGC in an amount simulating the activation of the ECP. At the same time, the cutoff valves isolated the outlet part of the loop (this simulated the operation of the check valves after the MCP).

Figure 4 shows the parameter variation under one such set of conditions with the pressure falling at 0.3 MPa/min. Figure 4 shows that the parameter change is as in NC states up to the end of the third minute, and then the fall in pressure is accompanied by coolant loss in the form of a steam-water mixture after the feedwater is supplied to the DGC and the outlet part has been cut off, which is indicated by the ongoing overfilling of the separator and the monotonic fall in the pressure in the heat-production zone. Under these conditions, the normal cooling of the heat-production zone is disrupted at 2.3 MPa. It was characteristic that the feedwater front did not reach the heat-production zone, as was evident from the coolant temperature at the inlet to it, which was equal to the saturation temperature at the inlet pressure.

The experiments showed that for a given feedwater flow rate, the minimum permissible pressure increases with the pressure reduction rate (Fig. 5). Under all these conditions, it is characteristic that the coolant temperature at the inlet to the core is approximately equal to the saturation temperature. However, while the coolant temperature at the inlet to the heat-production zone remained below the saturation temperature until the minimum pressure was reached, which corresponds to that temperature, there was no fuel-element overheating. That condition can be provided by increasing the feedwater flow rate.

Figure 6 shows one of these cooling conditions with the loop pressure falling. It is evident that the fuel-element cooling by the feedwater having a temperature below the saturation value occurred at minute 18 and a pressure of 3.5 MPa with the pressure falling at a rate of about 0.2 MPa/min, that pressure exceeding the permissible value by 1.0 MPa. The ongoing pressure reduction in the loop and the stabilization at the level of 1.0 MPa did not cause fuel-element overheating. It was also found that the safe rate of pressure reduction increased with the feedwater flow rate to the DGC (Fig. 7).

As the hydraulic system and pipeline sections and lengths in the FMCL in the model corresponded completely to the FMCL in the reactor, we conclude that the circulation parameters should also be analogous, and therefore the experimental results on emergency cooling with feedwater supply to the DGC can be transferred directly to the reactor.

CONCLUSIONS

Pressure reduction in the FMCL of the reactor at rates of 0.2-1.5 MPa/min with a 3-min interruption in the feedwater, which is subsequently supplied to the separator with a flow-

rate of 10% of the nominal value, leads to the coolant boiling in the loop, which raises the water level in the separator, with water loss from the loop, and with a fall in hydrostatic head in the outlet part and disruption of the normal cooling in the heat-production zone when the pressure falls below the permissible value (3.8 MPa with the lower position for the DGC, or 4.5 MPa in the upper one).

If the feedwater is supplied to the separator at a flow rate sufficient to maintain the hydrostatic head in the outlet part at not less than 12 m of water column (this flow rate in the model corresponded to the nominal feedwater flow rate at 100% reactor power), then a stable NC condition is set up in the loop, which does not lead to disruption of the normal cooling in the heat-production zone even at pressures below the permissible value.

Emergency cooling by supplying feedwater to the DGC provides for normal cooling of the heat-production zone with larger falls in pressure than does cooling by the use of NC. If the feedwater is supplied in an amount providing for the coolant to enter the heat-production zone at a temperature below the saturation point, then normal fuel-element cooling is provided when the pressure falls below the minimum permissible value.

Activation of the ECP and feedwater supply to the DGC with a flow rate of 10% of the feed-pump output provides for normal cooling of the heat-production zone at pressure fall rates up to 0.2 MPa/min. To provide safety with emergency cooling at pressure reduction rates greater than 0.2 MPa/min, it is necessary to supply the DGC with a larger amount of feedwater from other sources in order that the heat-production zone should receive water at a temperature below the saturation point before the minimum pressure is reached.

SAFETY UNDER SERVICING COOLING CONDITIONS FOR RBMK REACTORS

V. N. Smolin, V. I. Esikov,
V. P. Shishov, V. P. Vasilevskii,
and V. S. Grigor'ev

The RBMK-1000 graphite-channel boiling-water reactor has 1693 fuel channels (FC) arranged in vertical holes in the graphite stack. Each channel is a body of tubular construction within which are located two fuel-element assemblies each containing 18 fuel elements which are flushed on the outside surface by the coolant [1].

The residual power production in the core when the reactor has been shut down is fairly substantial. For example, after a day it is 0.4% of the nominal power N_{nom}, i.e., 12.8 MW. After 30 days, this falls to 0.12% of N_{nom} and then remains virtually constant for a long time. This makes clear why it is not permissible to drain the core even after shutdown. Therefore, in conducting servicing on the forced multiple circulation loop (FMCL), it is necessary to organize core cooling.

One of the basic specifications for such a cooling system is that the cooling should be reliable and that safe access should be provided to the FMCL for examination or repair. This is attained by installing shutoff valves at various parts of the circuit to provide for draining, and also for organizing various core cooling modes.

During the design of the RBMK, three conditions of service cooling were provided in order to facilitate servicing (the corresponding schemes are shown in Fig. 1):

1) natural circulation with nominal water levels in the separators and the FMCL valves open;

2) interrupted natural circulation with the separators drained and the FMCL valves open; and

3) bubble mode with nominal water levels in the separators but with the pressure-regulating valves (PRV) at the inlet to the FC closed.
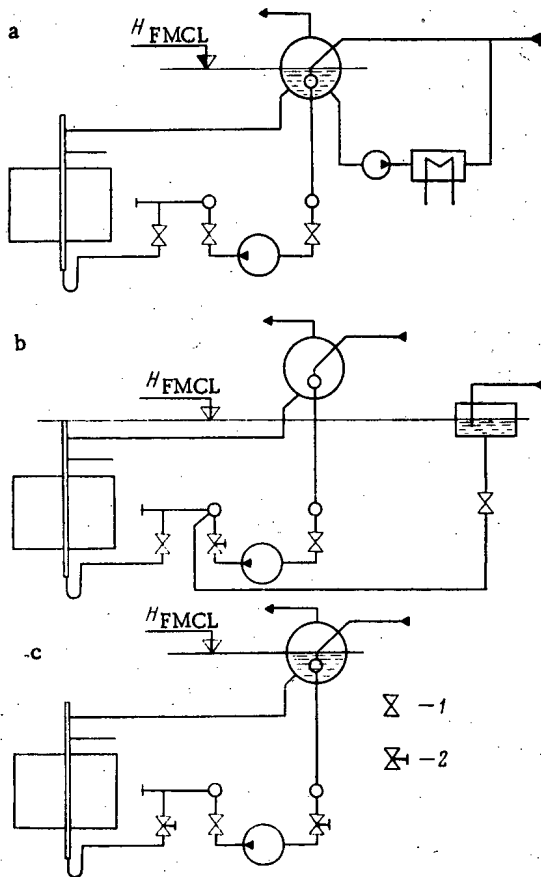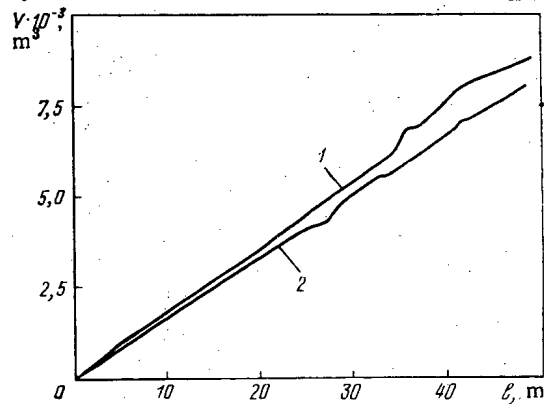
Fig. 1   Fig. 2

Fig. 1. Schemes for cooling the core in FMCL servicing: a) natural circulation; b) interrupted natural circulation; c) bubble mode; 1) valves open; 2) valves closed; H_{FMCL}) water level in FMCL.

Fig. 2. Volumes of hydraulic systems in relation to length for an experimental channel (1) and a fuel channel (2) as referred to one fuel element.

Natural circulation in the FMCL is provided by cooling the water in the outlet section of the loop, for which one uses the ordinary flushing and cooling system. The coolant heated in the core is transferred by the cooling pumps from the water tapping points in the separators to the flushing cooler, where the temperature is reduced by heat transfer to the water in the intermediate circuit. The cooled water passes to the feed pipelines and then to mixers at the inlet, which thereby cools the circuit. This condition is used for ordinary reactor cooling, in repairing the main circulation pumps (MCP), and also in servicing the pressurized and suction pipes, as well as for preliminary cooling of the reactor and FMCL before the start of servicing.

In the state of interrupted natural circulation, the separators are drained and communicate with the atmosphere. The core is supplied by spontaneous flow from a servicing tank connected to the pressurized collectors in the FMCL by special pipes. The gate valves in the MCP may be closed, i.e., it is possible to drain the FMCL as well. In this state, one can service the separators, the pipelines, the suction collectors, and the MCP pipelines with their valves. Here, to provide for safety, special rubber—metal plugs are inserted in the pipelines from the collectors and the MCP.

In the third state, the PRV at the inlet to the FC are closed, and the level in the separators is nominal. Under these conditions, one can repair the equipment and the FMCL pipes on the section from the inlet gate valves on the MCP to the PRV. This mode of cooling is widely used in general replacement of failed transducers in the flowmeters and PRV. In the latter case, a special freezing system provides ice plugs in the water pipelines.

513
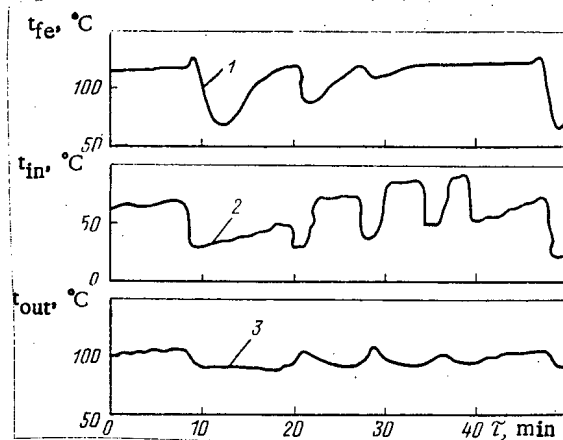
Fig. 3. Time variations in the temperatures of fuel-element simulator (1), of the coolant at the channel inlet (2), and at the outlet (3) with a water level in the FMCL above the horizontal part of the SWP.

Before implementation on the RBMK, the modes of core cooling were examined with a model at the Power Engineering Research and Development Institute. A detailed description of the model has been given in [2], which includes simulation of the FMCL. The lengths and cross sections of the water pipes have been made such that the hydraulic resistances, circulation times, and volumes of the various parts per fuel element corresponded to the FMCL in the reactor (Fig. 2), and the same applied to the heat-production zone, the exit part of the channels, and the steam-water pipes (SWP). The mutual dispositions of the collector, heat-production zone, channel outlet, and separator in the model were also identical with those in the FMCL in the reactor. The heat-production zone in the experimental channel was a bundle of seven rods simulating fuel elements of length 7 m and outside diameter 13.5 mm, which were arranged in a triangular lattice with a pitch of 16 mm. The heat was produced by passing direct current through the rods. The simulation principles led us to believe that the hydrodynamic and thermophysical processes in the hydraulic system of the model would be identical with those in the fuel channels.

Tests with the model showed that one got the usual natural circulation in the FMCL with the separators filled with water to the nominal level and the PRV open, and this provided reliable cooling at any pressure.

When the water level falls below the ends of the SWP tubes with the PRV open at atmospheric pressure in the separator, one gets interrupted natural circulation, in which there is no bubbling of the steam formed in the heat-production zone through the layer of water in the SWP. In this mode, the water is periodically ejected by the steam from the upper part of the channel and the SWP into the separator and is drained into the descending part. The difference in hydrostatic pressures also causes periodic entry of water from the descending part into the heat-production zone. This also provides reliable channel cooling if the steam ejected from the separator is compensated by supplying the loop with water and the water level in the FMCL is above the horizontal part of the SWP (Fig. 3).

When the water level in the FMCL falls below the horizontal part of the SWP (with the PRV open), the picture is very different. In that case, the steam displaces the water from the volumes above the heat-production zone into the upper part of the channel and then into the SWP. Here again, water from the descending section flushes the heat-production zone. However, this process continues until the horizontal part of the SWP and some of the vertical part have filled with water to equalize the hydrostatic pressures in the descending pipes and the channel. Then the filling of the heat-production zone with water ceases, and the water boils, so the temperatures of the simulation rods increase considerably (Fig. 4). This shows that it is impermissible for the water level in the FMCL to fall below the horizontal part of the SWP even with the valve at the inlet to the channel open.

We examined the cooling in the FC with the valve at the inlet closed at atmospheric pressure in the separator or with an excess pressure in it (up to 0.6 MPa), while the power level in the experimental channel corresponded to 0.8-1.7% of the power in a maximally loaded FC. In the first case, the separator communicated with the atmosphere, while in the second the separator was supplied with compressed air.

514
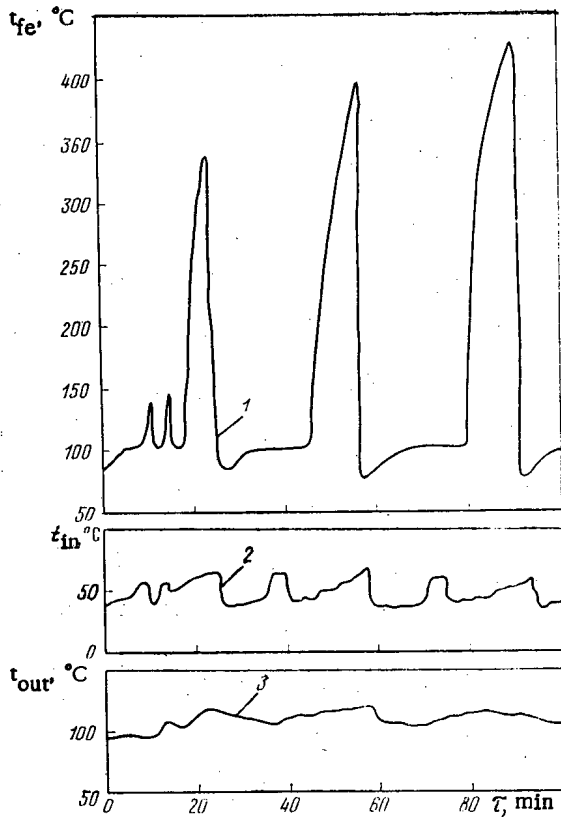
Fig. 4

Fig. 5

Fig. 4. Time variations in the temperatures of fuel-element simulator (1), of the coolant at the channel inlet (2), and at the outlet (3) with a water level in the FMCL below the horizontal part of the SWP.
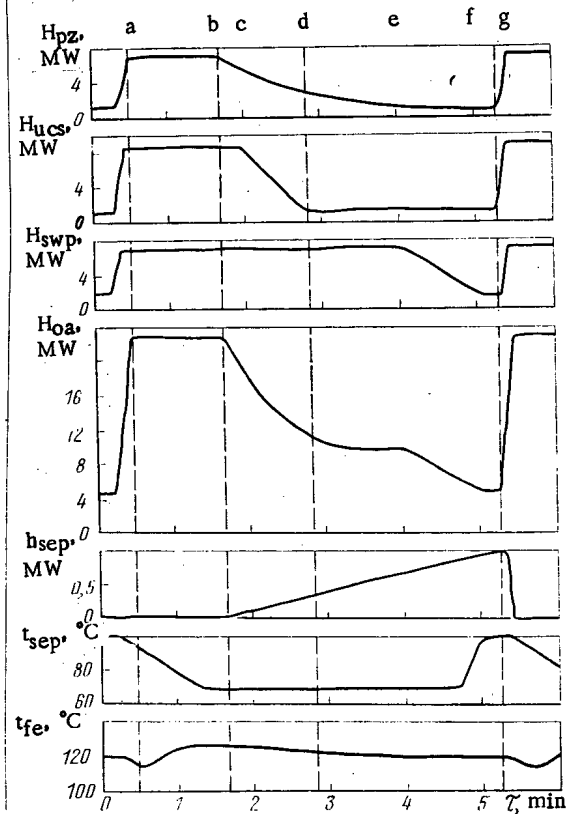
Fig. 5. Variations over time in the parameters of the hydraulic system in the model at atmospheric pressure in the separator with acceptable channel power. Here and in Fig. 6: H_{pz}, H_{ucs}, H_{swp}, and H_{oa} are the pressure differences in the heat-production zone, upper channel section, steam—water pipe, and in the system overall, while h_{sep} is the water level in the separator, and t_{sep} and t_{fe} are the temperatures in the separator and in a fuel element.

The changes in hydrostatic head in various parts of the channel indicate the state of the coolant in the loop and the processes occurring there under conditions of reliable cooling with atmospheric pressure in the separator (Fig. 5). At the instant corresponding to point a, the entire hydraulic system in the channel is filled with water from the separator. During time a–b, the water in the core is heated to the saturation temperature, as is evident from the stabilization of the saturation temperature at a pressure equal to the hydrostatic head at the level where the thermocouple lies. Point b corresponds to the start of bulk boiling in the core, as is evident from the reduction in hydrostatic pressure not only in the core but also generally. The retention of unchanged pressures in the upper channel section UCS above the core and in the SWP in period b–c indicates that the steam does not bubble through the water in the hydraulic system above the core, but instead the growing steam bubble displaces the water into the free volume of the separator (see the water level in the separator in Fig. 5). The period c–d corresponds to the steam displacing the water from the UCS, while d–e corresponds to displacement of the water from the horizontal part of the SWP (the hydrostatic pressure in the lifting part of the SWP remains unchanged). During period e–f, the steam displaces the water from the vertical part of the SWP, and at time g the steam reaches the separator, at which point the coolant temperature at the inlet to the separator becomes equal to the saturation temperature. When the steam enters the separator, it condenses, which produces avalanche filling of the entire hydraulic system with water from the separator (point g in Fig. 5). This figure shows that during the period b–g the separator gradually fills with water and then suddenly empties to flush the circuit. The process re-

515
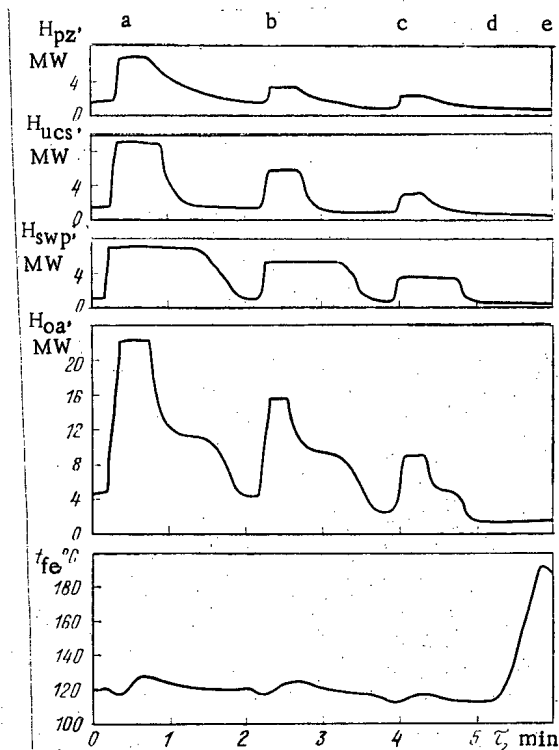
Fig. 6. Time course of the parameters in the hydraulic system in an experimental channel at atmospheric pressure in the separator with channel power above the permissible level.

peats in subsequent cycles. A characteristic feature is that the pressures in parts of the circuit in a given part of the cycle attain the same values as in the previous cycle. This cyclic process persists for any length of time for a constant channel power and constant water temperature in the separator.

The experiments showed that the period of this cycle is dependent on the channel power, decreasing as the power increases. Also, if the water temperature in the separator is below 70°C, there are water-hammer effects during the filling of the channel with water and the condensation of the steam there.

When a certain channel power is exceeded, the course of the process alters (Fig. 6). The hydrostatic pressures in the channel as a whole and in the individual parts in each successive cycle are reduced relative to the previous cycle, which indicates reduced water entry into the hydraulic system. Finally, the heat-production zone becomes almost entirely free from water, and then the steam begins to be superheated and the temperatures of the separator rods rise to an impermissible level.

When there is excess pressure in the separator, the process is very different. When the valve at the channel inlet is closed, the water in the heat-production zone is heated to the saturation temperature, and then steam begins to form. The resulting steam bubble increases in volume and displaces the water from the hydraulic system into the separator, thus filling part of the heat-production zone, the upper channel section, and part of the SWP. In all such experiments, the process was accompanied by steam superheating in the core and a substantial increase in the rod temperature at any pressure exceeding atmospheric and at power levels corresponding to the FC power from 20 to 50 kW. It seems that when there is excess pressure in the separator, the bulk steam generation in the core is less, and it is insufficient to displace the water from the entire hydraulic system. Only in that case could the steam reach the separator, where it would condense and the system would be filled by water.

Therefore, this study of the FC cooling conditions with the inlet valve closed has shown that reliable element cooling can be provided with atmospheric pressure in the separator by the hydraulic system being filled periodically with water from the separator. The maximum permissible power level indicated by the studies on the model is 25 kW for the real FC.

516

These experiments with the model on the cooling of the RBMK core have led us to formulate technological specifications covering safety during reactor operation if the circulation ceases and parts of the FMCL are drained, which have been inserted in "Engineering Rules for Operating Nuclear-Power Station Units Containing RBMK Reactors."

1. Transfer of the FC to bubble mode, i.e., closing the valves at the inlet, is allowed not earlier than 72 h after shutting down the reactor in order to reduce the residual power to a permissible level if the following conditions are met:

   a) water levels in the separators above the ends of the upper series of SWP;

   b) the water temperature in the separators should be not less than 80-90°C in order to avoid hydraulic shocks in the SWP; and

   c) the pressure in the separator is atmospheric.

2. It is forbidden to reduce the water levels in the separators below the ends of the SWP if the FC have closed inlet valves.

3. In all cases where parts of the FMCL are drained, the water level should not fall more than 1 m below the heads of the FC, and then it is necessary to provide a constant supply of cold water to the core. Also, studies on servicing conditions involving water level reduction in the loop have enabled us to establish the limiting positions for the upper and lower water levels in the servicing tank, which is connected to the FMCL to supply the core when the outlet system is drained. Results obtained with interrupted natural circulation have enabled us to formulate specifications for the forced cooling system operating during servicing without boiling.

LITERATURE CITED

1. N. A. Dollezhal' and I. Ya. Emel'yanov, The Channel Nuclear Power Reactor [in Russian], Atomizdat, Moscow (1980).
2. V. N. Smolin et al., Aspects of Nuclear Science and Engineering, Reactor Design Series [in Russian], Issue 1(8) (1974), p. 3.

GAS PHASE IN EXPERIMENTAL FUEL ELEMENTS WITH COMPACT

URANIUM DIOXIDE, IRRADIATED IN THE SM-2 REACTOR

A. P. Kirillovich, V. Sh. Sulaberidze,   UDC 621.039.546
Yu. I. Pimonov, V. N. Shulimov, Yu. G.
Lavrinovich, A. S. Biryukov, and
V. N. Kupriyanov

The intensive development of investigations of gas release from nuclear fuel is dictated by practical problems of increasing the efficiency of fuel elements and the safety of their subsequent reprocessing. A considerable amount of experimental data has been accumulated already about the kinetics of escape of gaseous fission products from uranium dioxide [1, 2], and the mechanism and development of numerical models of gas release were studied in [3, 4].

However, information about the chemical and isotopic compositions of the gas phase and about the behavior of gaseous fission products in irradiated fuel elements with compact uranium dioxide is very limited. This circumstance does not allow methods for calculating the release of gaseous fission products from nuclear fuel to be verified by means of direct measurements, and the amount of technological gases (oxygen, hydrogen, carbon compounds, etc.) which can affect the efficiency of the fuel elements [1, 5], to be estimated. The results of investigations of the amount and composition of the gaseous phase and the behavior of krypton, xenon, and helium in fuel elements with compact uranium dioxide and irradiated in the SM-2 reactor are presented below.

TABLE 1. Filling the Fuel Element, and also the Residual Background of the Sampling System

Gas being analyzed	Content, vol. %				
	He	$N_2 + CO$	O_2	Ar	CO_2
High-purity grade bottled He (TU-51-940-80)	$99,999\pm5,9$	$0,00063\pm0,00012$	$0,00010\pm0,00002$	$0,000040\pm0,000008$	$0,000070\pm0,000014$
Gas filling fuel elements Nos. 0021-0023	$99,93\pm5,9$	$0,040\pm0,008$	$0,01\pm0,002$	$0,0080\pm0,0016$	$0,0060\pm0,0012$
Background of sampling system:					
before purging with He	$99,96\pm5,9$	$0,20\pm0,004$	$0,010\pm0,002$	$0,009\pm0,002$	$0,00030\pm0,00002$
after purging with He	$99,98\pm5,9$	$0,010\pm0,002$	$0,0010\pm0,0002$	$0,00030\pm0,00005$	$0,00020\pm0,00004$
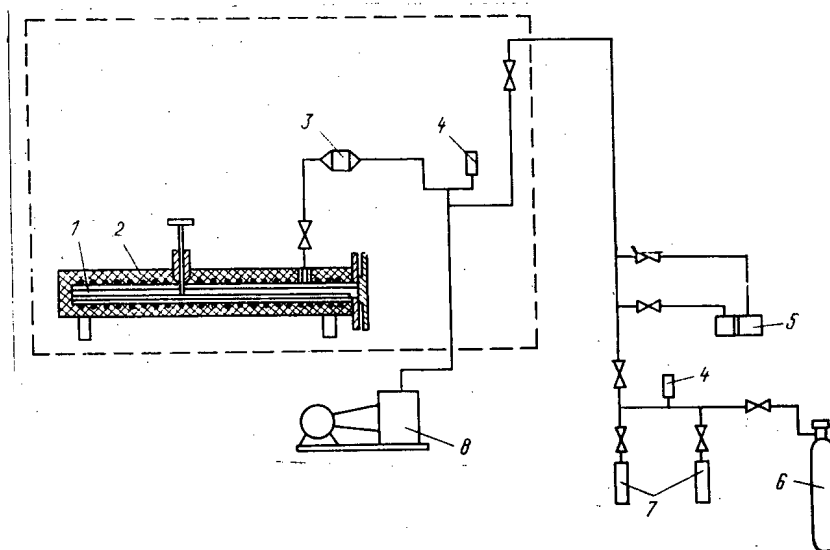
Fig. 1. Diagram of the gas sampler with the fuel-element puncturing device: 1) fuel element; 2) device for puncturing irradiated fuel elements; 3) filter; 4) PMT-4m lamp; 5) differential micromanometer; 6) helium bottle; 7) ampules for sampling the gas; 8) vacuum pump.

METHOD

Irradiation of the experimental fuel elements was carried out in a cell of a channel of the low-temperature water loop of the SM-2 research reactor. The design of the irradiation facility, the pressure gauge in the fuel element, and the irradiation procedure were described earlier in detail in [2]. The error in determining the linear power of the fuel element amounted to ±7%, the average burnup ±8%, and the total error in determining the amount of gas in the fuel elements during irradiation did not exceed ±10%. When preparing fuel elements 0021, 0022, and 0023, the composition of the filling gas and the purity of the helium were monitored by the mass-spectrometric method. The results of the analyses are given in Table 1.

Measurement of the Amount and Composition of the Gas Medium under the Jacket of the Irradiated Fuel Elements. After cooling (from 5 to 15 months), measurements of the pressure and sampling of the gas phase in the irradiated fuel elements were carried out by means of the sampling system (Fig. 1), located in a shielded chamber. The fuel element was placed in a device for puncturing the can, provided with a heater. The sampling system was hermetically sealed and pumped out with a vacuum pump to a pressure of 1.6-2.6 Pa.

In the absence of inleakage during 30-40 min, the sampling system together with fuel elements 0021, 0022, and 0023 was purged for 30 min with helium at a pressure of 40 kPa in order to reduce the background from oxygen, nitrogen, and other gases. After pumping out the system to 4 kPa, samples of the residual gas were taken and pumping out was continued to a

pressure of 1.6 to 2.6 Pa. Then the system was filled again with helium up to 4 kPa, held in this state for 30 min and, having sampled the residual gases (see Table 1), it was pumped out to 1.6–2.6 Pa. The can was then punctured, and the gas released was sampled in the ampules. The amount of gas in the fuel element was determined by measuring the pressure (grade of accuracy of the instrument 1.5) with a known volume of the system.

The investigation of the chemical and isotopic compositions of the gas in the irradiated fuel elements was carried out by the mass-spectrometric method similar to that described in [6]. An MI-1201 mass spectrometer was used for the measurements and was additionally provided with a system for admitting the gas. The method of comparison with the sample to be analyzed with a control gas mixture, prepared from certificated gases (i.e., additionally verified for purity), was used.

<div align="center">RESULTS AND DISCUSSION</div>

The principal irradiation parameters and the characteristics of the experimental fuel elements, taken from [2], are presented in Table 2. The fuel cores of the experimental fuel elements, with a cladding of Kh18N10T steel, were assembled from a plug of compacted uranium dioxide enriched to 10% in ^{235}U. The density of the fuel in fuel element 001 was 10.43 ± 0.03 g/cm^3, and in the remaining fuel elements it was 10.0 ± 0.1 g/cm^3. The temperature of the can during irradiation was 200°C.

The results of the determination of the quantity and composition of gas in the fuel elements after irradiation and cooling are given in Table 3. It can be seen that there is satisfactory coincidence between the data on the quantity of gas under the fuel element can, obtained during intrareactor measurements, and with puncturing of the can. The principal components of the gaseous medium in the irradiated fuel elements (Table 3) are Xe, He, and Kr, the volume content of which varies depending on the original quantity of filling gas and the conditions of irradiation of the fuel elements. In addition to gaseous fission products and He in the irradiated fuel elements, Ar (0.001-0.06%), H_2 (<0.01%), CO, CO_2, O_2, and N_2 are present. The relative content of these gases is small, but increases significantly by desorption from the fuel. The increase of the O_2 content in fuel elements 0021 and 0023 after irradiation by more than a factor of 3 and 30, respectively (see Tables 1-3), apparently is related also with the liberation of this element during fission of the oxide fuel. According to estimates, the fraction of unbound O_2 amounts to ~0.05% of the O_2 liberated for fuel element 0023. Although the effect of O_2, N_2, CO, H_2, and moisture on the fuel element efficiency is still insufficiently studied, in order to avoid interaction with the can and the fuel, it is necessary to strive for a reduction of the content of these gases in the fuel elements.

Experimental data about the release of Xe and Kr during irradiation and during subsequent heating of the fuel elements after puncturing the can, and also the calculated buildup and

TABLE 2. Irradiation Parameters and Characteristics of Experimental Fuel Elements

Characteristic	Fuel element			
	001	0021	0022	0023
Mass of fuel in fuel element, g	181,5	174,3	174,0	173,4
Average burnup of uranium atoms over fuel element, %	4,40	3,95	4,80	3,58
Range of variation of average linear power, kW/m	44—82	25—50	30—85	20—45
Post-irradiation cooling, months	5	15	15	14,3
Quantity of filling gas, cm^3/fuel element*	95	104	98	9,5
Free volume in fuel element, cm^3	1,52± ±0,05	1,60± ±0,05	1,63± ±0,05	1,69± ±0,05

*Fuel element 001 was filled with helium and air; the other fuel elements, with helium.

TABLE 3. Quantity and Composition of the Gas Phase during Irradiation of Experimental Fuel Elements

No. of fuel element	Quantity of gas, n. cm³		Content, vol. %							
	intrareactor determination	puncturing of can.	Xe	Kr	He	Ar	O₂	N₂ + CO	CO₂	H₂
001	168±4	171±9	30,62±0,40	4,64±0,83	41,67±0,80	0,001±±0,0001	4,10±0,15	18,90±0,31	0,063±0,006	0,010±±0,001
0021	160±4	169±3	37,86±2,04	6,20±0,37	55,72±3,32	0,0037±±0,007	0,019±0,008	0,17±0,022	0,03±0,004	<0,010
0022 *	190±5	8,6±3,1	57,28±1,14	10,3±0,4	29,9±2,1	0,06±0,005	0,091±0,007	1,58±0,19	0,141±0,012	<0,010
0023	50±2	64,4±3,1	73,91±2,9	11,25±0,56	14,8±1,2	0,04±0,008	0,05±0,007	0,18±0,002	0,10±0,01	<0,01

*Escape of gas occurred when the fuel element can was punctured.

TABLE 4. Yield of Xe and Kr from Uranium Dioxide during Irradiation and Subsequent Heating of the Fuel Elements

Gas	Fuel element	Quantity of gas released, n. cm³					Calculated buildup of gas,† cm³/fuel element	Yield of gaseous fission products, % of calc.	
		during puncting of can (t = 20°C)	during heating of fuel			during puncturing of can and heating of fuel elements		during puncturing of can	during puncturing of can and heating of fuel element
			240	390	620				
Xenon	001	52,36	Not measured				145	36,1	Not calculated
	0021	64,0	Not measured		17,41	81,41	124	51,6	65,6
	0022	4,92	9,50	1,51	2,98	18,91	151	Not calculated	
	0023	47,6	0,26	1,76	14,17	63,79	112	42,5	56,9
Krypton	001	7,93	Not measured				25	31,7	Not calculated
	0021	10,48	Not measured		2,66	13,14	22	48.4	59,7
	0022	0,88	1,67	0,23	0,36	3,14	26	Not calculated	
	0023	7,24	0,039	0,306	1,97	9,55	20	36,2	47,7

*Duration of heating of fuel element: at 240°C, 1.5h; at 390°C, 18 h; and at 620°C, 20 h.
†Fraction of gaseous nuclides of Xe and Kr taken from [9].

TABLE 5. Relative Content of Xe and Kr

Fuel element	Xe/Kr	
	experiment	calculated [4]
001	6,60±1,5	5,81
0021	6,15±0,7	5,81
0022	5,99±0,37	5,78
0023	6,97±1,5	5,81

yield of gaseous fission products from the fuel, are presented in Table 4. The yield of Kr and Xe from irradiated uranium dioxide amounts to 31.7–51.6% of the calculated buildup. Heating of the fuel elements to a temperature of 240–620°C led to the additional release of ~14% Xe and 11% Kr (fuel elements 0021 and 0023). The remaining quantity of gaseous fission products is entrapped in the cavities and crystal lattice of the uranium dioxide, but can be released [6] by heating to 1500–1600°C and during chemical processing, for example, during fluorination of the fuel. An estimate, taking into account the relative yield of Xe and Kr during fluorination [6], showed that in fuel elements 0021 and 0023, the relative fraction of gaseous fission products in the crystal lattice of uranium dioxide did not exceed 10%; i.e., the gas entrapped is found mainly in the pores. This coincides well with the results of a detailed consideration of the distribution of gaseous fission products in uranium dioxide [7].

Together with the study of the yield of gaseous fission products during heating of the fuel elements, the quantity of helium released from the fuel in those same conditions was measured. The additional yield of helium when the fuel element was heated to 620°C did not exceed 2.3% (fuel element 0023), measured when the can was punctured. This means that the
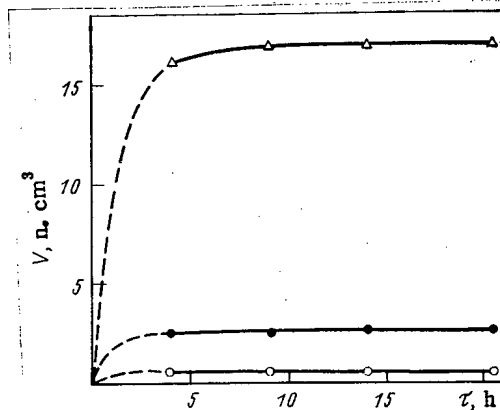
Fig. 2. Dependence of the yield of helium ($\bigcirc$), krypton ($\bullet$), and xenon ($\triangle$) from irradiated uranium dioxide at 620°C on the holding time: ———) experiment; -----) extrapolation.

TABLE 6. Isotopic Composition of Kr and Xe in Irradiated Fuel Elements

Fuel element	Content of nuclide, vol. %							
	Kr				Xe			
	83	84	85	86	131	132	134	136
001	14,0±0,5	27,6±0,2	7,1±0,1	51,3±0,5	11,1 ± 0,1	17,0±0,1	29,2±0,2	42,7±0,4
0021	13,38±0,12	27,96±0,19	7,86±0,26	50,44±0,30	10,58±0,14	17,76±0,020	28,89±0,03	41,81±0,09
0022	12,72±0,15	28,10±0,28	6,98±0,28	52,19±0,91	10,80±0,13	17,81±0,11	29,18±0,10	42,03±0,14
0023	13,58±0,9	29,12±0,66	6,79±0,42	50,50±0,24	10,45±0,22	17,77±0,05	29,73±0,05	42,05±0,13

content of helium in the fuel is small and amounts to ~0.004 cm^3/g UO_2. It should be emphasized that the quantity of helium accumulated as the result of nuclear reactions is considerably less than its content in the gas medium of the fuel element.

When studying the sorption of helium by uranium dioxide in the irradiated fuel elements, filled with this gas to a high pressure (5.4 MPa), the content of adsorbed helium in the fuel was determined [8] as equal to ~0.0057 cm^3/g UO_2. The kinetics of the release of Xe, Kr, and He from irradiated uranium dioxide at 620°C is shown in Fig. 2. Holding of fuel element 0022 after puncturing the can for 100 h at 20°C did not lead to a marked increase of the amount of gaseous fission products and helium released.

Table 5 shows the measured and calculated ratios of Xe/Kr in the gaseous medium in the irradiated fuel elements. The calculations by the procedure developed in [4], taking into account the nonidentical diffusion coefficients of Xe and Kr in the fuel [3], give ratios which are too low by comparison with the calculated ratios. This can be due to several causes: by radioactive decay of ^{85}Kr, by the formation of ^{136}Xe by the reaction ^{135}Xe$(n,\gamma)^{136}$Xe, and by fission of the accumulated ^{239}Pu nuclei. The contribution of each of these processes can be estimated by means of an analysis of the isotopic compositions (Table 6), found by direct mass-spectrometric measurements.

The ratios of the mass numbers 83/86, 83/85, 83/84, 85/86, 131/134, and 133/134 correspond to the yields of nuclides from the fission of ^{235}U nuclei in the thermal neutron spectrum (average deviation ±10%, maximum does not exceed ±15%). This confirms the weak effect of the decay of ^{85}Kr and the buildup of ^{239}Pu. The measured ratios of the mass numbers 131/136, 132/136, and 134/136 are less than the calculated ratios by a factor of 1.6-1.8, which is explained by the above-mentioned reactions. Related with this, the buildup of ^{136}Xe increases the Xe/Kr ratio by a factor of 1.2 approximately, and the rate of formation of gaseous fission products by a factor of 1.16-1.17. With respect to the total quantity of gas under the can, this corresponds to ~8% for fuel elements 001, 0021, and 0022, filled with helium to a high pressure (1.77-2.49 MPa) and ~13% for fuel element 0023, the initial gas pressure in which was significantly lower (0.206 MPa).

As the mean statistical relative deviation of the calculated data from the experimental data amounts to ±13%, the buildup of ^{136}Xe which complicates the procedure for calculating the gas release [4], in this case cannot be disregarded. The relative contents of Xe and Kr

in the gas medium in the irradiated fuel elements, and the data about their release by heating to 620°C show that the yield of Xe is higher than the yield of Kr. This circumstance is not always taken into consideration in calculations of the gas release from nuclear fuel.

CONCLUSIONS

A complex procedure has been developed for the study of gas release from nuclear fuel, including reactor measurements and post-reactor determination of the amount and composition of the gas medium in the fuel elements at room and elevated temperatures. In fuel elements with compact uranium dioxide (density 10.0-10.43 g/cm^3), in addition to gaseous fission products and the helium introduced, Ar, H_2, O_2, CO, CO_2, and N_2 are present, and after irradiation their quantity exceeds the initial quantity, measured for unirradiated fuel elements, by a factor of several.

The yield of Xe and Kr under the can of the fuel elements during irradiation of uranium dioxide in the SM-2 reactor amounts to ~30-50%, but the measured ratio of Xe/Kr exceeds the calculated ratio by a factor of 1.2, because of the reaction $^{135}Xe(n, \gamma)^{136}Xe$. The content in the fuel of adsorbed helium is equal to ~0.004 $n.cm^3/g$ UO_2. The data obtained can be used for physics and technological calculations, and also for refining the procedure for the determination of gas release.

LITERATURE CITED

1. B. V. Samsonov and V. Sh. Sulaberidze, Analytical Review of the Scientific-Research Institute of Atomic Reactors [in Russian], Vol. 16, Dimitrovgrad (1977).
2. V. Sh. Sulaberidze et al., Preprint of the Scientific-Research Institute of Atomic Reactors [in Russian], Dimitrovgrad, P-26(541) (1982).
3. V. Sh. Sulaberidze and A. V. Pershin, At. Energ., 53, No. 3, 158 (1982).
4. V. Sh. Sulaberidze and A. V. Pershin, Preprint of the Scientific-Research Institute of Atomic Reactors [in Russian], Dimitrovgrad, P-19(584) (1983).
5. V. A. Tsykanov et al., Preprint of the Scientific-Research Institute of Atomic Reactors [in Russian], Dimitrovgrad, P-5(271) (1976).
6. A. P. Kirillovich et al., Preprint of the Scientific-Research Institute of Atomic Reactors [in Russian], Dimitrovgrad, 31(439) (1980).
7. H. Zimmerman, Nucl. Technol., 28, 127 (1976).
8. K. Vinjamuri and D. Owen, Nucl. Technol., 47, No. 1, 119 (1980).
9. V. I. Polikarpov et al., Monitoring the Leak Tightness of Fuel Elements [in Russian], Gosatomizdat, Moscow (1962).

INFLUENCE OF THE TEXTURE OF PRISMATIC PLANES ON THE ANISOTROPY
OF DEFORMATION OF IRRADIATED ZIRCONIUM ALLOYS

Yu. N. Knizhnikov and V. V. Kolomytkin　　　　　　　UDC 621.039.531:669.296

The rate at which the dimensions of zirconium alloy members change as a result of deformation under irradiation often determines the service life of these members. For example, the service life of the fuel channels (FC) of RBMK reactors [1] is limited by an increase in the tube diameter until contact is made with the surrounding graphite stacking. In the case of fuel-element cans, crumpling of the cans as a result of an azimuthally anisotropic buildup of strain can be the limiting process [2]. Under reactor conditions the service life is also affected by radiation-induced growth, leading to a substantial change in the length of the members.

In a correct consideration of the deformation behavior of hcp zirconium alloys it is necessary to take into account the anisotropy of changes in the dimensions of the fabricated tube. In the case of fuel channels, as a consequence of radiation-induced creep the diameter of a tube made of an anisotropic material may increase twice as slowly as in a tube of isotropic material [3]. Because of the lower rate of creep in the circumferential direction for the anisotropic material, the time until the fuel-element can crumples can also increase severalfold [2].

When considering the creep strain of an anisotropic material, use is made of so-called anisotropy coefficients, which are defined by analogy with coefficients for describing anisotropic plastic strain [4] and enter into the pertinent deviator expressions for the creep rate. For a tube these coefficients are determined experimentally from the ratios of the strains under different loading conditions (e.g., uniaxial or biaxial loading) [5].

A polycrystalline alloy based on α-Zr can have a texture that is formed during fabrication of the tubes. Usually, for anisotropy calculations the texture is considered for $\{0002\}$ basal planes or the basis vectors of the crystallites relative to the axis of the tube. Such a texture is characterized by the orientation factors F_R, F_T, and F_A of the basis vectors relative to the tube axis. These factors essentially are the averaged squared cosines of the angles of the basis vectors to the respective coordinate axes. Usually, the direct polar diagram drawn in the plane perpendicular to the tube radius is employed for such averaging (Fig. 1).

A texture model, permitting the anisotropy coefficients to be calculated on the basis of x-ray measurements of the texture of the tube material, has been proposed and tested under reactor conditions [6]. In this case, however, only the basal texture was considered and it was assumed that the orientation of the rotation of the crystallites relative to the basis vectors is equiprobable, i.e., there is no texture of the prismatic planes.

Nevertheless, a number of experimental facts [7] indicate the existence of a texture of prismatic planes. We know of only one paper [8] about the influence of this texture on the plastic strain, but only the mechanism of dislocation slip along prismatic planes was analyzed. In the light of this it is desirable to consider the influence of the texture of prismatic planes on the deformation of zirconium alloys as applied to the main mechanisms of radiation-induced creep and growth.

In hcp metals the basal and prismatic $\{10\bar{1}0\}$ planes are energetically advantageous for slip [9]. In this case, for a network of line dislocations as well as for dislocation loops formed under irradiation only Burgers vector of the type $\mathbf{b} = {}^1/_3<11\bar{2}0>$ are observed. From the axial symmetry of the hcp structure it follows that there are three differently oriented $\{10\bar{1}0\}$ planes, along which line dislocations move, and three $\{11\bar{2}0\}$ planes, where dislocation loops are formed.

　　　　523
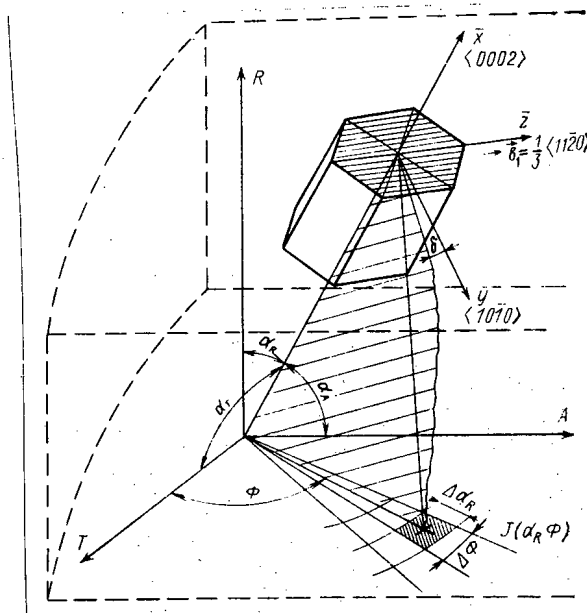
Fig. 1. Orientation of a crystallite relative to the tube axis. Construction of the basal texture diagram $(x, y, z) \leftarrow [L_{in}(\alpha_R, \Phi, \delta)] \rightarrow (R, T, A)$, $\sigma_{ij} = l_{im} l_{jn} \sigma_{mn}$, $i, j = x, y, z$, $\varepsilon_{mn} = l_{im} l_{jn} \varepsilon_{ij}$, $m, n = R, T, A$.

We assume that both the density of the line dislocations and the density and average size of the loops are the same in the corresponding, differently oriented planes. In this model crystallite deformation processes in the directions of the vectors $\mathbf{b_1}$, $\mathbf{b_2}$, $\mathbf{b_3}$, turned 60° relative to each other, are equiprobable.

For each concrete deformation mechanism we can calculate the reduced stresses from an external load for a given vector $\mathbf{b}$ and the values found for the strain can be recalculated with allowance for the orientation of the crystallite. For this purpose we use the tensor expressions

$$\sigma_{ij}^b = l_{im} l_{jn} \sigma_{mn},$$
where $i, j = x, y, z;\ m, n = R, T, A;$
$$\varepsilon_{hl} = l_{ih} l_{jl} \varepsilon_{ij}^b,$$
where $i, j = x, y, z;\ k, l = R, T, A.$ \hfill (1)

In expressions (1) we have used components of the $\| l \|$ matrix of coordinate transformations obtained by three rotations through angles of α_R, Φ, and δ, where the angle δ specifies the orientation of the crystallite relative to the x axis. In the case of a prismatic texture the preferred orientation of the crystallites relative to the external system of coordinates was observed.

For further calculation of the strain of specimens cut from a textured tube, the contributions to the strain from individual oriented grains must be averaged, assuming as usual that these contributions are additive.

In order to distinguish the characteristics of the strain anisotropy, we arbitrarily assume that the structure factors, reflecting the dependence of the strain on the external conditions (stresses, temperature, neutron flux intensity) and on the microstructural characteristics of the material, have a value of 1. Since in the range of the operating stresses of reactor structures the creep mechanisms depend linearly on the stress [10], the following estimates are made for unit stress. We calculate the strain under uniaxial loading of specimens cut in the circumferential and axial directions of the tube. For the assumptions made above these strains are equal to the anisotropy coefficients C_{TT} and C_{AA} [6].

The influence of the texture of prismatic planes for different mechanisms of deformation under irradiation is illustrated by the results of calculations (Fig. 2) using the example of

524
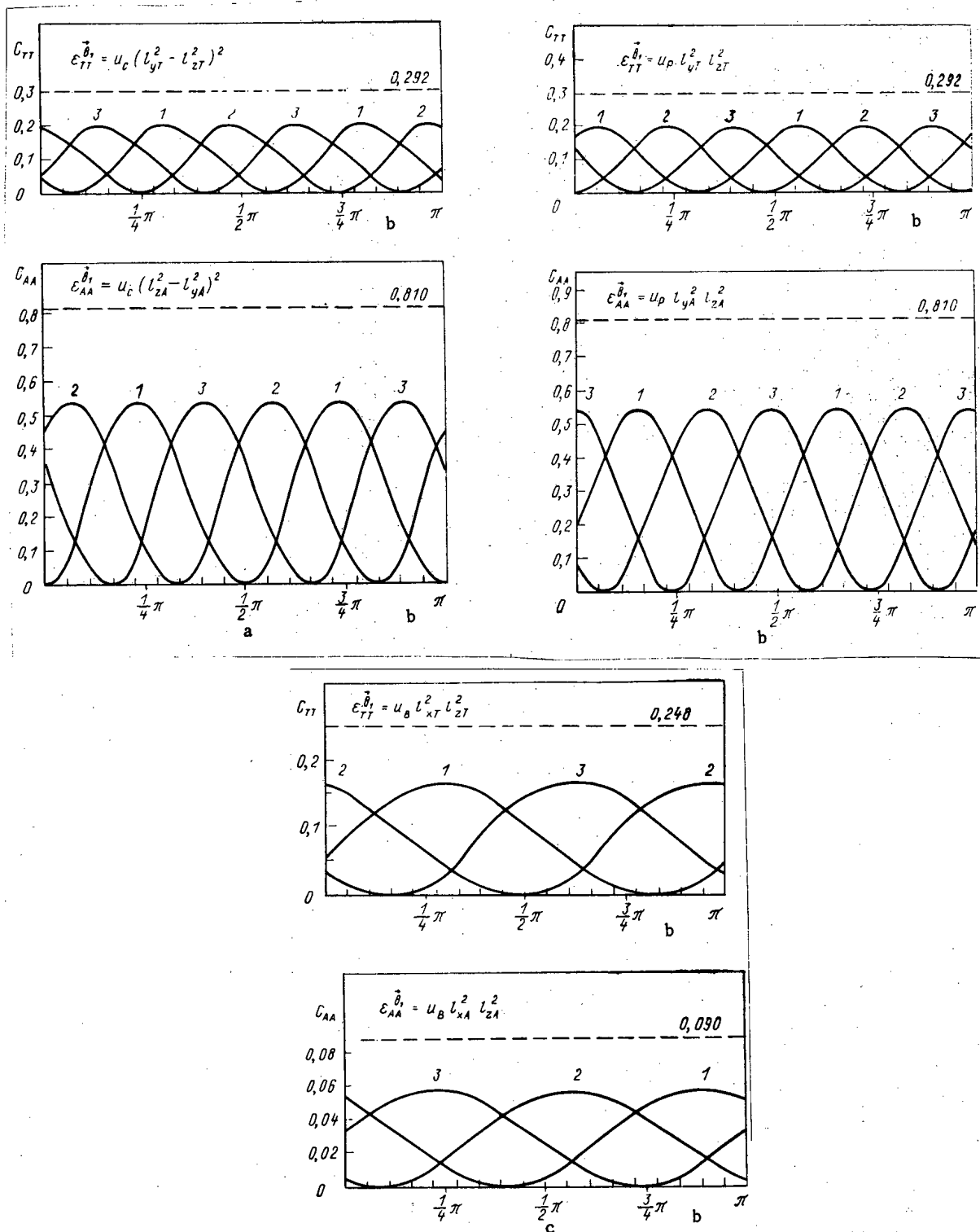
Fig. 2. Dependence of the contributions ε_{TT} and ε_{AA} to the strain from the rotation angle δ of a crystallite for the SIPA mechanism (a), the mechanisms of slip along prismatic (b) and basal (c) planes (averaging over a typical basal texture). In Fig. 2a we have $\varepsilon_{TI}^{b_1} = u_c(l_{zT}^2 - l_{yT}^2)^2$.

the typical texture of basal planes for fuel channels made of the alloy Zr + 2.5% Nb [11]. For such a texture the orientation factors of the basis vectors are $F_R = 0.44$, $F_T = 0.46$, and $F_A = 0.10$. Using the computational texture model, we can show that averaging the strain over the texture under consideration is equivalent to using an idealized ("concentrated") texture with the angular coordinations $\hat{\alpha}_R = 48°$ and $\hat{\Phi} = \pm 25°$; hence (see Fig. 1) $\hat{\alpha}_A = 71.5°$ and $\hat{\alpha}_T = 47.5°$.

525

The mechanism of the climb of dislocations and dislocation loops [stress-induced preferential adsorption (SIPA) of point defects] is supported by experiments and correctly describes radiation-induced creep over a wide range of external conditions. In our calculations for zirconium alloys with an anisotropic distribution of sinks for point defects we use a simplified expression for creep strain as a consequence of the climb of dislocations (from [6]):

$$\varepsilon^{b} = u_{c}(\sigma_{\parallel} - \sigma_{\perp}), \tag{2}$$

where ε^{b} is the strain in the direction of $\mathbf{b}$, u_{c} is the structure factor for the mechanism of climb per unit time, and $\sigma_{\parallel}$ and $\sigma_{\perp}$ are the stress components in the directions parallel and perpendicular to $\mathbf{b}$. It must be pointed out that when a more stringent dependence of the creep strain on the stress components [12] is used in the calculations the coefficients in formula (2) change by roughly 10% but all the conclusions concerning the influence of the prismatic texture remain valid.

For the vector $\mathbf{b}_1$ (z axis) shown in Fig. 1 we have $\sigma_{\parallel} = \sigma_{zz}$ and $\sigma_{\perp} = \sigma_{yy}$. The component σ_{xx}, parallel to the dislocation line, is absent from formula (2). Then, when expressions (1) are taken into account the strains in the crystallite, normalized to the external axes, are described by the equalities

$$e_{TT}^{b_1} = u_{c}(l_{zT}^{2} - l_{yT}^{2})^{2};$$
$$e_{AA}^{b_1} = u_{c}(l_{zA}^{2} - l_{yA}^{2})^{2}. \tag{3}$$

Figure 2a gives the contributions (labeled 1, 2, 3) to the respective strains ε_{TT} and ε_{AA} for different rotation angles δ of the crystallite, from the possible strains in the directions of $\mathbf{b}_1$, $\mathbf{b}_2$, $\mathbf{b}_3$ during the climb of dislocations. The sum of these contributions is constant. Upon averaging the strains over the assumed basal texture, apart from the structure factor we get $C_{TT} = \sin^{4}\hat{\alpha}_{T}$ and $C_{AA} = \sin^{4}\hat{\alpha}_{A}$, which indicates the lack of a dependence on the prismatic texture.

For the mechanism of prismatic slip of dislocations in the direction of the vector $\mathbf{b}_1$ (the z axis in Fig. 1) the normalized shear stress in the prismatic plane has the form $\sigma_{yz} = l_{yn}l_{zn}\sigma_{nn}$, where σ_{nn} are the components of the external stresses. Then the strains in the crystallite, normalized to the external axes, are described by the expressions

$$e_{TT}^{b_1} = u_{P}l_{yT}^{2}l_{zT}^{2}; \quad e_{AA}^{b_1} = u_{P}l_{yA}^{2}l_{zA}^{2}. \tag{4}$$

Figure 2b shows the dependences of the contributions to the strain from the rotation angle of the crystallite for slip in the directions of $\mathbf{b}_1$, $\mathbf{b}_2$, $\mathbf{b}_3$. Upon averaging the strains over the texture diagram, we find that the total strain of the specimen does not depend on the prismatic texture and, apart from the structure factor, we have $C_{TT} = \sin^{4}\hat{\alpha}_{T}$ and $C_{AA} = \sin^{4}\hat{\alpha}_{A}$, as in the case of the climb of dislocations.

For the mechanism of the slip of line dislocations in the basal plane of a crystallite in the direction of the vector $\mathbf{b}_1$ (z axis) the normalized shear stress is $\sigma_{xz} = l_{xn}l_{zn}\sigma_{nn}$. Then the strains in the crystallite, normalized to the external axes, can be written as

$$e_{TT}^{b_1} = u_{B}l_{xT}^{2}l_{zT}^{2}; \quad e_{AA}^{b_1} = u_{B}l_{xA}^{2}l_{zA}^{2}. \tag{5}$$

Figure 2c gives the contributions to the strain for different directions of the slip and a varying rotation angle δ of the crystallite. Averaging the strain over the basal texture apart from the structure factor we find that $C_{TT} = \cos^{2}\hat{\alpha}_{T}\sin^{2}\hat{\alpha}_{T}$ and $C_{AA} = \cos^{2}\hat{\alpha}_{A}\sin^{2}\hat{\alpha}_{A}$. The radiation-induced growth of the crystallite under consideration (see Fig. 1) is characterized by an increase in the transverse dimensions, i.e., ε_{zz} and ε_{yy}, as a result of the growth of extra planes. The axial dimensions ε_{xx} decrease, thus ensuring that the volume is conserved. Therefore, $\varepsilon_{xx} = -(\varepsilon_{yy} + \varepsilon_{zz})$. Estimates made within the framework of the assumptions adopted here show that the prismatic texture, if it does indeed exist, does not affect the resulting strain.

Thus, with the assumptions made the radiation-induced creep and growth of reactor structures made of zirconium alloy with an arbitrary basal texture do not depend on the texture of the prismatic planes. Anisotropy of plastic deformation under the influence of the prismatic texture, however, cannot arise at different dislocation densities in the respective prismatic planes; this also holds for line dislocations as well as for dislocation loops in

526

particular. Such a situation could occur as a result of a different accumulation of dislocation loops in different prismatic planes, e.g., because of residual stresses in the tube. The contributions to the strain for the individual directions will then predominate, and this could lead to anisotropy of strain in the reactor structure.

LITERATURE CITED

1. N. A. Dolezhal' and I. Ya. Emel'yanov, Channel-Type Nuclear Power Reactor [in Russian], Atomizdat, Moscow (1980).
2. Yu. N. Knizhnikov, V. N. Kuznetsov, and P. A. Platonov, Preprint IAÉ-3021, Institute of Nuclear Energy, Moscow (1978).
3. E. Ibrahim and R. Holt, J. Nucl. Mater., 91, 311 (1980).
4. R. Hill, Mathematical Theory of Plasticity [Russian translation], Gostekhteorizdat, Moscow (1957).
5. P. Ross-Ross, V. Fidleris, and D. Fraser, Can. Metall. Q., 11, No. 1, 101 (1972).
6. R. Holt and E. Ibrahim, Acta Met., 27, 1319 (1979).
7. Ya. D. Vishnyakov et al., Theory of Texture Formation in Metal Alloys [in Russian], Nauka, Moscow (1979).
8. E. Ibrahim, Scripta Metall., 15, 361 (1981).
9. A. A. Predvoditelev and O. A. Troitskii, Dislocations and Point Defects in Hexagonal Metals [in Russian], Atomizdat, Moscow (1973).
10. V. V. Kolomytkin, Preprint IAÉ-2938, Institute of Nuclear Energy, Moscow (1978).
11. V. Goncharov et al., J. Nucl. Mater., 90, 224 (1980).
12. A. Ryazanov and V. Borodin, Radiat. Effects, 56, 179 (1981).

ION- AND ELECTRON-STIMULATED LOW-TEMPERATURE DESORPTION OF GASES

DISSOLVED IN METALS

N. P. Katrich and V. N. Kanishchev

UDC 548:539.12.04

For a further understanding of radiation-stimulated gas desorption [1, 2] it is desirable to measure, under the same conditions, the desorption stimulated by different radiation (with respect to defect formation): a beam of heavy ions possessing an energy substantially higher than the threshold of lattice atomic displacement, and an electron beam of an energy much below the threshold.

The results given in this paper were obtained on an apparatus which was described earlier in [2] and which was not redesigned apart from the target chamber (Fig. 1). Two targets 1 are clamped by stainless steel disks to two hollow copper holders. By means of a massive copper vessel 2 and thin-walled molybdenum tubes 3 the chamber is divided into two compartments. The first, working compartment (I), which the irradiated surfaces of the targets face, is connected to two RMO-4s partial-pressure gauges. The rate at which gas is pumped out of the compartment is determined by the conductivity of the calibrated apertures 4 and amounts to 3 $dm^3 \cdot sec^{-1}$ for hydrogen at room temperature. The pump rate from the second compartment (II), which the surfaces of the target holders and the connecting tubes face, is roughly ten times the pump rate from the working compartment. A target 1 mm thick and 12 mm in diameter was cut from commercial-grade polycrystalline copper and zone-refined monocrystalline niobium. Molybdenum-ion beams with an energy of 6.5-7 keV ($i_+ = 0.015$ μA) and electron beams with an energy of 20-500 eV ($i_e = 20$-80 μA) and 4-9 keV ($i_e = 0.005$-0.05 μA) were used. The high-energy electron beam was formed in the same gun as the beam of Mo^+ ions, for which purpose the sign of the extraction potential was changed. The area of the irradiated spot on the target was ~0.1 cm^2. The flux of low-energy electrons was used in a two-electrode system, in which the target was the anode and a tungsten spiral 5 (see Fig. 1) a few millimeters away from the target was the cathode. The area of the irradiated spot in this case was 0.3-0.4 cm^2.

The vacuum engineering preparation of the apparatus and the technique used to measure the desorption characteristics were described earlier in [2]. The measurements began at a pressure of ~10^{-8} Pa. Isothermal desorption was studied at the temperature of liquid nitrogen. The investigations of thermally activated desorption were carried out while the target holder was heated from 78 to 293°K at a rate of ~0.1°K·sec^{-1}. The temperature of the holder in the direct proximity of the target was measured with a Chromel–Alumel thermocouple. To preclude possible error in the measurements owing to sorption processes on the nonworking surface of the target holder we used a monitoring target during the study of thermally activated desorption. Both holders (see Fig. 1) were cooled when one target was being irradiated. After the irradiation, at first one and then the other heater was heated and the signals of thermally stimulated desorption from the irradiated and unirradiated targets were compared. The desorption rate (sec^{-1}) was calculated from the formula

$$dn/dt = n_1 \left[p(t) - p_0 \right] w. \tag{1}$$

The coefficients of isothermal and thermally stimulated desorption, respectively, were determined from the formulas

$$\alpha = \frac{dn}{dt} \frac{q}{i}; \tag{2}$$

$$\alpha_T = \int_{t_0}^{\infty} \frac{dn}{dt} \, dt \, \frac{q}{i\vartheta}, \tag{3}$$

where n_1 is the number of gas particles per cubic decimeter at a pressure of 133 Pa, p_0 is the initial partial pressure of the gas (Pa), $p(t)$ is the partial pressure of the gas at the time t of the measurement, w is the rate of pumping from the target chamber (dm^3·sec^{-1}), i is the ion or electron beam current (A), q is the electron charge (C), ϑ is the duration of irradiation (sec), and t_0 is the time at which target heating begins. The integral $\int_{t_0}^{\infty} \frac{dn}{dt} dt$ was calculated by means of graphical integration.

Figure 2 shows the isothermal desorption curves (dependence of dn/dt on t) for hydrogen (curves 3, 4, and 5) and a gas of mass number 28 (M = 28) (curves 1 and 2) from copper cooled to 78°K under bombardment with 6.7-keV Mo$^+$ ions (i_+ = 0.015 µA) (curves 2 and 4) and 300-eV electrons (i_e = 20 µA) (curves 1 and 3). From the signals corresponding to mass numbers 12, 14, and 16 we can conclude that the gas with M = 28 consists of N, CO, and C_2H_4. Despite the large difference in the mass, energy, and flux of the bombarding particles, the curves for desorption under ion and electron bombardment are very similar. The initial spike on the isothermal desorption curves for ion [1] and electron [3] bombardment is attributed to the desorption of gas adsorbed on the surface of the target, while the quasisaturation of the desorption rate, which is observed during prolonged bombardment, is attributed to the diffusion of impurities from the bulk of the target to the surface. This division of the desorption into surface and bulk components is very arbitrary since it is not yet known what mechanisms are responsible for either the low-temperature stimulated diffusion of gaseous impurities [4] or the final stage of stimulated desorption of the gas [5].

Acceleration of the diffusion of gaseous impurities in a metal under the effect of electron bombardment has not been considered, to our knowledge. This may be due to the difficulties encountered in separating the effects due to target heating and electron excitation. Thus, in [3] it was shown that under isothermal electron bombardment (j_e = 2–20 mA·cm^{-2}) over the temperature range 80–600°K gas diffusion from the bulk to the surface of a metal can make a substantial contribution to the desorption rate, but nothing is said about the nature of the bulk diffusion of gaseous impurities.

Experiments to establish the dependences of the desorption rate on the current i_e of bombarding electrons with an energy of up to 500 eV showed that dn/dt ~ i_e to within 2% when i_e varies from 2 to 80 µA. Therefore, desorption, and along with it diffusion, are not a result of heating of the surface layer of the target during electron bombardment. As in the case of ion bombardment [2], when the electron bombardment stops, the isothermal desorption signal (curve 5 on Fig. 2) falls off much more slowly than would follow from the actual pump rate.

528
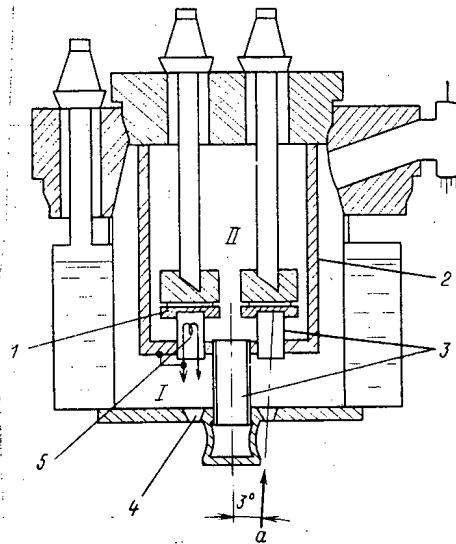
Fig. 1. Diagram of target chamber:
(a is a beam of e^-Mo^+).
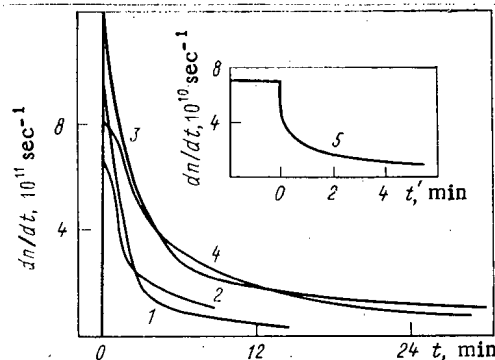
Fig. 2. Desorption rate dn/dt of gas from copper at 78°K as a
function of the time: t = 0 is the time of application of an
electron or ion beam to the target (1-4) and t' = 0 is the time
at which the electron beam is removed from the target (5).

If the data given in Fig. 2 are substituted into formula (2), we see that $\alpha^+ \gg \alpha^-$,
where α^+ and α^- are the isothermal desorption coefficients for ion and electron bombardment,
respectively. The result obtained supports the well-known fact that the efficiency of iso-
thermal desorption is much higher under ion bombardment than under electron bombardment. This
property of ion treatment is utilized extensively to purify the surface of a solid from ad-
sorbed gases [6].

Figure 3 shows the curves of thermally stimulated desorption (the dependence of dn/dt
on the temperature T of the target) of hydrogen and as gas with M = 28 after bombardment of
copper with 300-eV electrons at a current of i = 20 μA (curves 1 and 2) and 7-keV ions (i =
0.015 μA) and thermally stimulated hydrogen after bombardment of niobium with 6.7-keV Mo^+ ions
(i = 0.015 μA) (curve 3) and 4-keV electrons (i = 0.025 μA) (curve 4). In each of the four
cases the bombardment lasted for 10 min. Curves I and II in Fig. 3 correspond to heating of
the irradiated target and the unirradiated monitoring target, respectively. Figure 3c shows
curves obtained under the same conditions as the curves in Fig. 3b but using a single-section
target chamber (without the shield 2 in Fig. 1). From Figs. 3b and 3c we see how sorption
processes on the nonworking surface of the target holder can distort the results of measure-
ments and how efficient a two-compartment target chamber design is in isolating the useful
signal from the total signal of thermally stimulated desorption. Upon comparing the corre-
sponding curves in Fig. 3, we can assume that a general mechanism exists for gas desorption
stimulated by ionizing radiation.

529
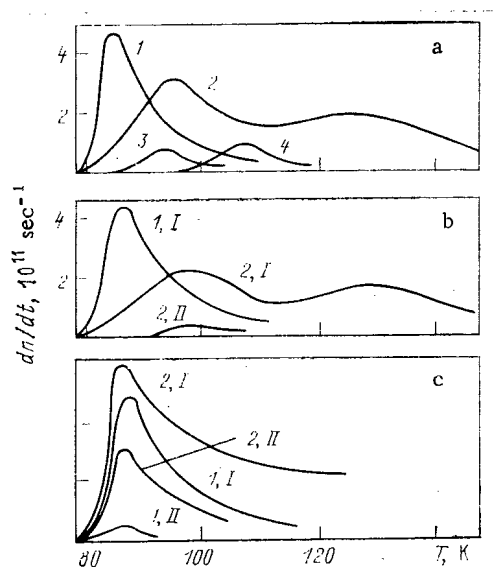
Fig. 3.

Fig. 4.

Fig. 3. Temperature dependence of gases from copper and niobium during annealing after bombardment for 10 min.
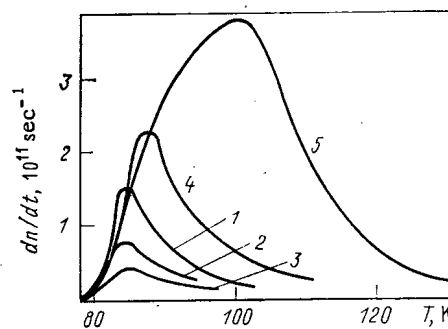
Fig. 4. Temperature dependence of the rate of hydrogen desorption from copper during annealing of the same target: 1-3) 10-min bombardment with 100-eV electrons (i_+ = 80 µA); 4, 5) 12-min bombardment with ions and with 6.7-keV electrons (i = 0.015 µA), respectively.

Whereas the inequality $\alpha^+/\alpha^- \gg 1$ was satisfied in all the cases considered, the ratio of the coefficients α_T^+ and α_T^- corresponding to thermally stimulated desorption after ion and electron bombardment proved not to be constant: It was much larger than 1 (curves 1 and 2 of Fig. 3a and curves 1, I and 2, I of Fig. 3b), close to 1 (curves 3 and 4 of Fig. 3a), and was even less than 1. As shown by the results of an experiment on cyclical bombardment of the same copper target (Fig. 4) the higher efficiency of thermally stimulated desorption after electron bombardment ($\alpha_T^+ < \alpha_T^-$) than after ion bombardment can be attributed to the higher penetrating power of the electrons. In this experiment one cycle consists of cooling the target to 78°K, bombarding it, and heating it to 293°K. In each of the first three cycles the target was bombarded with 100-eV electrons (i = 80 µA) for 10 min (curves 1-3). Then it was bombarded with ions (fourth cycle, curve 4) and electrons (fifth cycle, curve 5). The irradiation parameters in the fourth and fifth cycles were the same: particle energy 6.7 keV, beam current 0.015 µA; duration of bombardment 20 min. The decrease in α_T with an increasing number of cycles (curves 1-3, Fig. 4) as well as the decrease in α with a growing irradiation dose (see Fig. 2) can be explained by depletion of the surface layer of the target in gaseous impurities. The desorption rate should then depend on the impurity content. The ions penetrate to a considerably smaller depth into the metal than the electrons do and, therefore, the energy absorbed per unit volume of the metal is much higher during ion bombardment than during electron bombardment. Estimates show [7] that 8-keV Mo^+ ions and 200-eV electrons have roughly the same effective depth range of ~20 Å (1 A = 10^{-10} m) in copper [6]. The energy of the ions is converted mainly into energy exciting the electronic subsystem of the solid [4]. The higher efficiency with which gaseous impurities are removed from the surface layer of the target under ion bombardment can be explained by the higher density of electronic excitations (curve 4, Fig. 4). As a result of ion and electron bombardment the impurity distribution over the surface layer of the target changes markedly. The surface layers are depleted in impurities as compared with deeper-lying layers. Then in the case of electron bombardment even a comparatively low excitation density at a depth "unaffected" by ions can lead to a more pronounced desorption effect (curve 5, Fig. 4) than under ion bombardment. The result of cyclical bombardment (see Fig. 4) did not change when in one cycle during the bombardment and some time after the bombardment before the onset of heating of the target the residual hydrogen pressure changed from roughly 10^{-8} to 10^{-5} Pa, while the residual pressure of the gas with M = 28 changed from 10^{-8} to 10^{-6} Pa. It can thus be concluded that the vacuum conditions do not affect the stimulated purification of the target from gaseous impurities, i.e., the low-temperature desorption was irreversible. In view of this the assumption is that the impurity

530
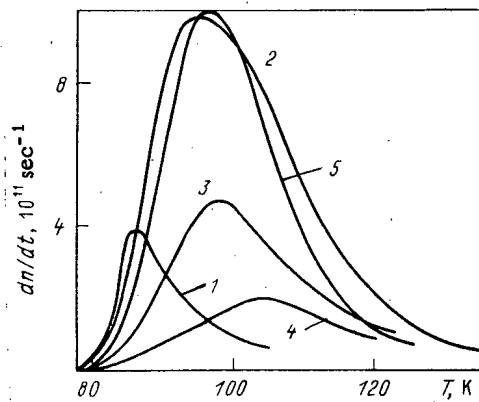
Fig. 5. Dependence of desorption rate on the temperature during annealing: 1-4) hydrogen desorption from copper after electron bombardment; 1) energy of bombarding electrons 500 eV, i_e = 20 μA, duration of bombardment 6 min; 2) 4.5 keV, 0.005 μA, 40 min; 3) 5.8 keV, 0.015 μA, 20 min; 4) 9.2 keV, 0.02 μA, 15 min; 5) calculation.

center itself is an accumulator of activation energy and the process of stimulated desorption is a method of relaxation of electronic excitations in a metal containing gaseous impurities.

From Fig. 4 we see that the maximum of the curve of thermally stimulated desorption after bombardment of copper with electrons possessing an energy of a few kiloelectron volts (curve 5) is observed at a higher temperature T_m (the temperature of the maximum) than after ion bombardment (curve 4). A similar displacement of T_m also appears for niobium (curves 3 and 4, Fig. 3a). The tendency for the maximum of the curve of thermally stimulated desorption to be displaced to a higher temperature as the electron energy is increased is clearly seen from Fig. 5. As will be shown below the displacement of T_m is consistent with the concepts about layer-by-layer removal of gaseous impurities from a target by ionizing radiation: The deeper the bombarding particle penetrates into the target, the larger the volume that undergoes outgassing.

Volume diffusion of gaseous impurities when an electron-bombarded target heats up is also indicated by the fact that after sufficiently prolonged low-temperature electron bombardment the number of gas particles released is sufficient for several monoatomic layers. For example, integration of curve 2 of Fig. 5, that was obtained when the copper target heated up after 40-min bombardment with 4.5-keV electrons (i = 0.005 μA), indicates desorption of $3 \cdot 10^{14}$ hydrogen molecules, i.e., $3 \cdot 10^{15}$ cm^{-2}. For thermally stimulated desorption of gas particles it is necessary that the excited states of electrons, leading to stimulated diffusion, relax after the particles reach the surface of the target. Hence, besides mass transfer stimulated desorption should also be accompanied by a transfer of the energy of the electronic excitation.

Thus, radiation-stimulated desorption of gases from metals can be represented by the following scheme. When ionizing radiation acts on the metal, in addition to the formation of complexes of different kinds [1, 2], there is excitation of some impurity centers which migrate over the metal lattice, and reach the surface of the target, where the system gas particle-metal undergoes final decomposition.

If it is assumed that the process of thermally stimulated desorption is limited by the volume diffusion of the excited impurity centers, in the absence of internal sinks the concentration of excited impurity centers in the target at a distance x from the surface at a time t is given by the solution of the following boundary-value problem on the half-plane $(0 \leq x < \infty)$:

$$D \frac{\partial^2 c}{\partial x^2} = \frac{\partial c}{\partial t} ; \tag{4}$$

$$c(0, t) = 0; \tag{5}$$

$$c(x, 0) = \varphi(x), \tag{6}$$

531

where $D = D_0 \exp[-E/k(T_0 + \beta t)]$ is the diffusion coefficient, $D_0 = \mathrm{const}$, E is the diffusion activation energy, $T_0 = 78°K$, and β is the heating rate ($K \cdot \mathrm{sec}^{-1}$).

By the introduction of the new independent variable

$$\tau = \int_0^t D_0 \exp[-E/k(T_0 + \beta y)]\, dy \tag{7}$$

Eq. (4) is reduced to the equation of isothermal diffusion [8]. The measured desorption rate dn/dt is related to the concentration gradient near the surface by

$$\frac{dn}{dt} = SD\,\frac{\partial c}{\partial x}\Big|_{x=0}, \tag{8}$$

where S is the area of the irradiated spot.

When the solution of the problem (4)-(6) [9] with allowance for expression (7) is substituted into equality (8), we get

$$\frac{dn}{dt} = S(4\pi)^{-1/2} D_0 \tau^{-3/2} \exp[-E/k(T_0 + \beta t)] \int_0^\infty \varphi(x) \exp\left[-\frac{x^2}{4\tau}\right] x\, dx. \tag{9}$$

The number of excited impurity centers that have not yet reached the surface of the target is

$$m = S\int_0^\infty c(x, t)\, dx = \frac{2S}{\sqrt{\pi}} \int_0^\infty \varphi(x) \left\{ \int_0^{x(4\tau)^{-1/2}} \exp[-z^2]\, dz \right\} dx. \tag{10}$$

Since the initial distribution $\varphi(x)$ is not infinite, the integration in expression (10) is, in fact, carried out to a finite x'. From a certain time the relation

$$\int_0^{x(4\tau)^{-\frac{1}{2}}} \exp[-z^2]\, dz = x(4\tau)^{-\frac{1}{2}} \exp\left[-\frac{x^2}{4\tau}\right] \tag{11}$$

will be satisfied with acceptable accuracy. In practice this means that the rms distance over which the impurities migrate in a time t is several times a characteristic coordinate h in the initial distribution $\varphi(x)$.

Substituting relation (11) into expression (10) and comparing the result with Eq. (9), we can see that

$$\frac{dn}{dt} = \frac{D_0}{2\tau} m \exp\left[-\frac{E}{kT}\right]. \tag{12}$$

Using the approximation for expression (7) for $E \gg kT$ [10], we can simplify relation (12) to the form

$$\frac{dn}{dt} = \frac{\beta E}{2kT^2} m. \tag{13}$$

When even such a comparatively simple initial distribution $\varphi(x)$ as a Gaussian distribution with center at $x = h$ is substituted into the expression (9), we arrive at an involved expression for dn/dt. Certain conclusions, which are valid for any initial distribution, can be obtained, however, upon considering the example in which N excited impurity centers for $t = 0$ are concentrated in a plane at a distance h from the surface of the target, i.e., when

$$\varphi(x) = \frac{N}{S}\,\delta(x - h). \tag{14}$$

Upon substituting equality (14) into expression (9), we find

$$\frac{dn}{dt} = Nh(4\pi)^{-1/2} D_0 \tau^{-3/2} \exp\left[-\frac{E}{kT} - \frac{h^2}{4\tau}\right]. \tag{15}$$

It can be easily checked that dn/dt reaches its maximum on condition that

532
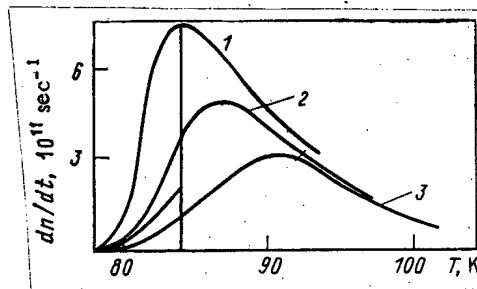
Fig. 6. Dependence of rate of hydrogen desorption from copper on the temperature during annealing after electron bombardment.

$$\sqrt{\frac{2D_0}{h^2} \frac{kT_m}{\beta E}} \exp\left\{-\frac{E}{kT_m}\right\} \approx 1.$$ \hfill (16)

From expression (16) it follows that T_m increases with increasing h. This example enables us to interpret one more distinctive feature of thermally stimulated desorption of hydrogen, observed after both ion and electron bombardment of copper and niobium (Fig. 6). In these experiments, after 12-min bombardment of the target with 300-eV electrons (i = 40 μA) the target holder heated up to $T_m \simeq 84°K$ (curve 1) at a rate of $0.1°K \cdot sec^{-1}$, after which the holder temperature was lowered to 78°K in several seconds, i.e., the process of thermally stimulated desorption was interrupted. Heating was next resumed at the previous rate (curve 2). The heating was interrupted one time (curve 2) or several times (curve 3) at the same temperature. It is seen from Fig. 6 that after each interruption of the heating the maximum of the thermally stimulated desorption curve is displaced increasingly toward higher temperatures. In the case when $\varphi(x) \sim \delta(x - h)$ we can show that if the heating is interrupted at the temperature $T_m = T_{m1}$, determined by expression (16), upon reheating the condition for $T_m = T_{m2}$ will have the form

$$\sqrt{\frac{2D_0}{h^2(1 + \sqrt{3})} \frac{kT_{m2}}{\beta E}} \exp\left[-\frac{E}{kT_{m2}}\right] = 1.$$ \hfill (17)

From a comparison of expressions (16) and (17) it is seen that the displacement of T_m upon a second heating is equivalent to the characteristic coordinate of the initial distribution of the excited impurity centers being moved deep into the target.

The activation energy value E that does not depend on the initial distribution $\varphi(x)$ enables us to calculate the dependence dn/dt(T) from formula (9) with a given $\varphi(x)$ and to compare the calculated curve with the experimental curve 2 in Fig. 5; upon approximating the latter by means of expression (13) in the temperature range 108–124°K we obtained E = 0.18 ± 0.01 eV. This is less than half the known activation energy for the diffusion of hydrogen in copper [11], probably because the displacement of an excited impurity center requires a lower activation energy. The dependence of dn/dt on T (curve 5), calculated from formula (9) for E = 0.18 eV and

$$\varphi(x) = \frac{N'}{S\sqrt{2\pi\sigma}} \left\{ \exp\left[-\frac{(x-h)^2}{2\sigma}\right] - \exp\left[-\frac{(x+h)^2}{2\sigma}\right] \right\},$$

where $N' = 2.3 \cdot 10^{14}$ is the number of particles and $\sigma = 0.3 \, h^2$, is given in Fig. 5 (curve 5) and differs less from the experimental dependence (curve 2) than do those obtained when in formula (9) we substitute $\varphi(x) \sim \delta(x - h)$ and $\sim \exp[-x^2/2\sigma]$, where h and σ are variable constants. The action of ionizing radiation on a solid in the subthreshold energy range should lead to a redistribution of the dissolved gases (segregation of impurities along grain boundaries, filling of cavities in the solid with gas, etc.).

LITERATURE CITED

1. N. P. Katrich and N. S. Sidel'nikova, in: Production and Properties of Single Crystals and Scintillators [in Russian], No. 3, Izd. VNIImonokristallov, Kharkov (1979), p. 68.
2. N. P. Katrich and V. N. Kanishchev, At. Energ., 53, No. 6, 379 (1982).

3. L. Peterman, in: Sorption Processes in a Vacuum [in Russian], Atomizdat, Moscow (1966), p. 162.
4. V. S. Vavilov, A. E. Kiv, and O. R. Niyazova, Mechanisms of the Formation and Migration of Defects in Semiconductors [in Russian], Nauka, Moscow (1981).
5. V. N. Ageev, Poverkhnost'. Fiz., Khim., Mekh., No. 4, 1 (1982).
6. A. R. Shul'man and S. A. Fridrikhov, Secondary-Emission Methods of Investigating Solids [in Russian], Nauka, Moscow (1977).
7. H. Schiott, Radiat. Effects, 6, 107 (1970).
8. L. L. Kunin et al., Problems of Degassing Metals [in Russian], Nauka, Moscow (1972).
9. V. Ya. Arsenin, Methods of Mathematical Physics and Special Functions [in Russian], Nauka, Moscow (1974).
10. A. C. Damask and J. G. Diens, Point Defects in Metals, Gordan and Breach (1964).
11. E. Fromm and E. Gebhardt, Gases and Carbon in Metals [Russian translation], Metallurgiya, Moscow (1980).

ABSORPTION PARAMETERS OF DEUTERIUM IONS IN MOLYBDENUM

A. A. Pisarev and V. N. Tsyplakov   UDC 533.924

A great deal of attention has been devoted in recent years to the study of absorption (capture and retention) of the ions of hydrogen isotopes by metals in connection with a program of investigation of the interaction of the ion component of a plasma with materials. A large number of papers in this domain have been published recently. However, it is evident when they are compared that the results obtained, notwithstanding their qualitative agreement, often differ significantly quantitatively. One of the possible causes are differing experimental conditions. Therefore, the effect of a number of factors on the measured capture parameters is analyzed in this paper. Molybdenum and deuterium ions are selected as the objects of investigation, since molybdenum is one of the most actively studied materials [1-9], and by using deuterons instead of protons one can avoid the difficulties associated with the presence of residual hydrogen in a vacuum, the sample, and the surrounding structures.

Equipment and Procedure. We used a sample of brand MChVP polycrystalline molybdenum (99.95% purity) with a thickness of 0.2 mm annealed in a 10^{-4} Pa vacuum at 1700°K for 1 h. It was irradiated with beams of D_2^+ and D_3^+ ions having an energy per deuteron E_d = 3-11 keV in doses of $5 \cdot 10^{14} - 5 \cdot 10^{18}$ deuterons/cm² at a flux density of $(0.6-14) \cdot 10^{14}$ deuterons/(cm²·sec) in a $5 \cdot 10^{-5}$ Pa vacuum with a target temperature of 100-1000°K. If the flux density is not indicated in the figures, it is equal to $3 \cdot 10^{14}$ deuterons/(cm²·sec). After irradiation the target is heated in the very same vacuum chamber with a continuous temperature increase in time right up to 1700°K. In the course of the irradiation and subsequent heating the generation rate of deuterium gas was recorded. For calibration of the device we placed a shield of nickel heated to 800°K under a beam of D_2^+ ions. It is known that at this temperature all the imbedded deuterium escapes from the nickel into the vacuum at a dose $\geq 1 \cdot 10^{16}$ deuterons/cm² [10].

The dependence of the generation rate of deuterium gas on time in the course of the experiment is given in Fig. 1a as an example. The calibration on nickel prior to bombardment of the molybdenum and the change in the rate of gas generation from molybdenum upon irradiation (the interval t_1-t_2), after its conclusion (t_2-t_3), and during the subsequent heating (t_3-t_4) are shown. It is evident that during irradiation the reverse gas generation gradually increases due to thermal and radiatively stimulated processes and after its conclusion it rapidly decreases due to cessation of the action of the ion beam, and in the subsequent heating liberation occurs in several stages — the gas generation curve consists of several peaks, which are caused by the liberation of deuterium located in different capture centers having different binding energies. The gas generation spectra obtained upon heating after irradiation with different ion doses are shown in Fig. 1b (the results of thermodesorption experiments are discussed in detail in [11]). It is evident that as the dose increases low-temperature peaks appear and grow more and more in the spectrum which are produced by liberation of

0038-531X/84/5702-0534$08.50
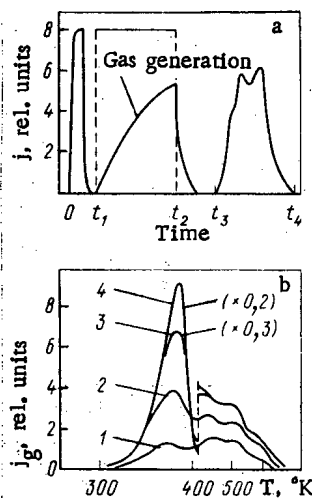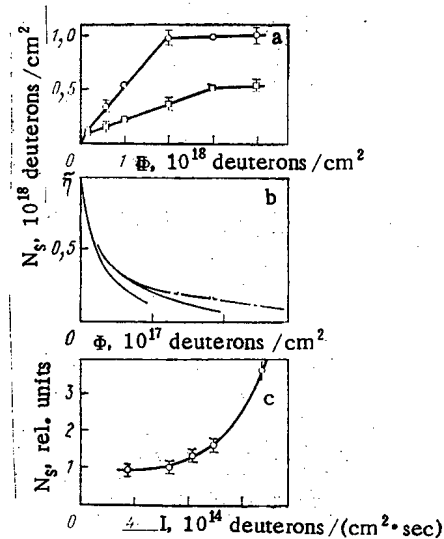
Fig. 1

Fig. 2

Fig. 1. Time dependence of the gas generation rate (a) in the course of irradiation and heating (b) in the course of the increase in temperature after irradiation in various doses by D_2^+ ions having an energy of 15 keV at 280°K: a) 0 — introduction of the ion beam onto the nickel shield; t_1 — introduction of the ion beam onto the molybdenum target; t_2 — cessation of irradiation (the area under the rectangle t_1-t_2 is equal to the irradiation dose); and t_3, t_4 — the start and finish of heating of the target after irradiation; b) 1-4 — irradiation doses of $1.4 \cdot 10^{17}$, $3 \cdot 10^{17}$, $10 \cdot 10^{17}$, and $30 \cdot 10^{17}$ deuterons/cm^2, respectively.

Fig. 2. The effect of the irradiation dose Φ and the ion flux density I on the capture parameters: a) dose dependences of the number of particles N_S liberated upon heating for ion densities of 13.5 ($\bigcirc$) and 4.2 ($\square$); b) dose dependences of the imbedding coefficient $\tilde{\eta}$ for flux densities of 0.73 (——), 2.0 (middle curve), and 3.2 (—•—); c) the dependence of N_S on the flux density with a dose of $1 \cdot 10^{17}$ deuterons/cm^2. The flux density on a and b is indicated in units of 10^{14} deuterons/(cm$^2 \cdot$sec), the irradiation temperature is 280°K, and the D_2^+ ions have an energy of 15 keV.

deuterium gas which is more weakly bound in the metal. At high irradiation doses the low-temperature peaks predominate, i.e., most of the imbedded deuterium is capable of escaping rapidly into the vacuum.

One can calculate the following parameters from the gas generation curves of Fig. 1a: the re-emission coefficient $\beta = j_r/I$, the imbedding coefficient $\tilde{\eta} = 1 - \beta = \partial N_0/\partial \Phi$, and the capture coefficient $\eta = N_0/\Phi$, where j_r is the rate of reverse gas liberation from the sample in the course of irradiation, I is the flux of ions onto the target, N_0 is the number of captured particles, deuterons/cm^2, and Φ is the irradiation dose, deuterons/cm^2. It is evident that in the general case $\tilde{\eta} \neq \eta$. In the published papers the parameters $\tilde{\eta}$ and η are called the same — the capture coefficient or the capture efficiency, which introduces additional uncertainty when comparing the result of different papers.

It is evident from Fig. 1a that in the interval t_1-t_2 the area of the rectangle is equal to the radiation dose Φ, the number of captured particles $N_0 = \Phi - \int_{t_1}^{t_2} j\,(t)\,dt$, and the number

of particles liberated during the heating after irradiation is $N_s = \int_{t_3}^{t_4} j\,(t)\,dt$. A check of

the balance of particles has shown that $\Phi = \int_{t_1}^{t_4} j\,(t)\,dt$.

If the irradiation temperature is low, the value $N_a = \int_{t_2}^{t_3} j\,(t)\,dt$ is small; if in the

course of the heating all the captured gas is removed from the sample, $N_0 = N_S$. In this case the capture parameters can be determined from the area of the gas generation curves $j_g(t)$ during the heating after irradiation. The $j_g(t)$ curves are called the gas generation spectra
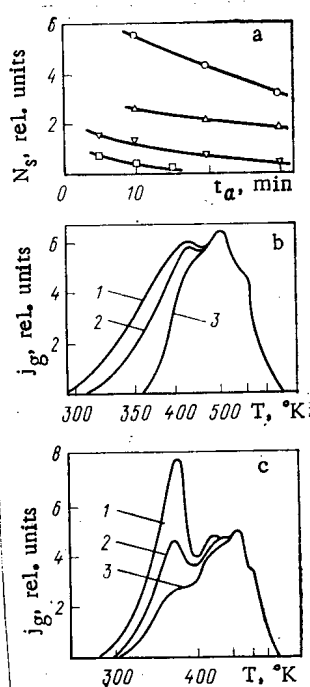
Fig. 3.
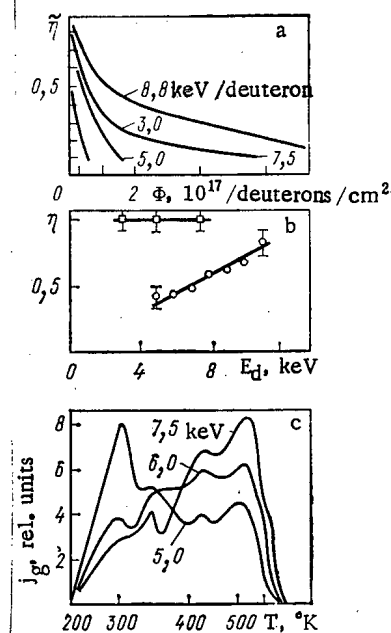
Fig. 4

Fig. 3. The effect of the time t_α and the exposure temperature of the target after irradiation T_α (a) on the number of particles liberated from the target upon heating and (b, c) on the nature of the gas generation spectra. The irradiation temperature is $T_i = 280°K$, and the D_2^+ ions have an energy of 15 keV; a) dose of $4 \cdot 10^{16}$ deuterons/cm^2, $T_\alpha = 430$ ($\bigcirc$), 455 (Δ), 480 (∇), and 500°K ($\square$); b) dose of $1 \cdot 10^{17}$ deuterons/cm^2, $T_\alpha = T_i = 280°K$, exposure time $t_\alpha = 10$ min, 2 h, and 15 h for curves 1, 2, and 3, respectively; c) dose of $6 \cdot 10^{17}$ deuterons/cm^2, $T_\alpha = T_i = 280°K$, flux density and exposure time for curves 1, 2, and 3, respectively, are $I = 1 \cdot 10^{15}$, $1 \cdot 10^{15}$, and $3.4 \cdot 10^{14}$ deuterons/$(cm^2 \cdot sec)$ and $t_\alpha = 10$, 60, and 10 min.

Fig. 4. The effect of the ion energy on the capture and gas generation parameters: a) dose dependence of the imbedding coefficient for different values of the energy (numbers next to the curves), $T_i = 280°K$, flux density, respectively, of $6 \cdot 10^{13}$, $7 \cdot 10^{13}$, $32 \cdot 10^{13}$, and $40 \cdot 10^{13}$ deuterons/$(cm^2 \cdot sec)$; b) dependence of the capture coefficient on the ion energy for a dose of $6 \cdot 10^{16}$ deuterons/cm^2, $T_i = 280$ ($\bigcirc$) and 100°K ($\square$); and c) gas generation spectra upon heating from $T_i = 100°K$ for a dose of $1.2 \cdot 10^{16}$ deuterons/cm^2 (numbers next to the curves give the ion energy).

or the thermodesorption spectra, since they usually consist of several peaks. One can determine the capture parameters more accurately from the re-emission curve $j_r(t)$ in the course of irradiation; however, these parameters are often determined from the gas generation spectra $j_g(t)$, since one can simultaneously obtain information about the activation energy of the gas generation process and the number of particles liberated from capture centers of different kinds.

Experimental Results and Discussion. We measured the capture parameters in this paper both from the gas generation curves in the course of irradiation and from the gas generation spectrum with subsequent heating. We studied experimentally the effect of the irradiation dose, the ion energy, the ion flux density, the temperature during irradiation, the time between irradiation and heating, the temperature, and the exposure time after irradiation.

It is shown in Fig. 2 how the irradiation dose and the ion flux density affect the measured characteristics. It is evident that as the irradiation dose increases the number of captured particles increases (see Fig. 2a) and the capture and imbedding coefficients decrease (see Fig. 2b). The decrease of $\tilde{\eta}(\Phi)$ occurs due to saturation of the centers which strongly bind deuterons (this is confirmed by the gas generation spectra given in Fig. 1b). At large doses the particles, having a low binding energy, are capable of easily escaping from the metal in the course of irradiation or after its conclusion. However, it is significant that at an imbedding temperature $T_i = 280°K$ $\tilde{\eta}$ does not decrease to zero right up to a dose greater

536
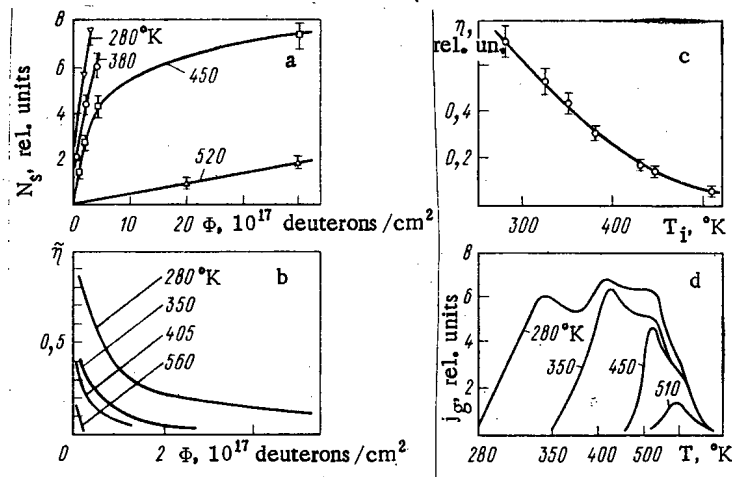
Fig. 5. The effect of irradiation temperature on the capture and gas generation parameters (D_2^+ ions with an energy of 15 keV: a) dose dependence of the number of particles in the gas generation spectrum N_s for different values of the imbedding temperature T_i (numbers next to the curves); b) dose dependence of the imbedding coefficient $\bar{\eta}$ for different values of T_i; c) dependence of capture coefficient η on the imbedding temperature T_i; d) the gas generation spectra for different values of T_i (numbers next to the curves).

than 10^{18} deuterons/cm² both in the measurements during irradiation and in the measurements from the gas generation spectra. This may be caused by diffusion of deuterium from the imbedding zone into the interior of the metal.

As the flux density increases the number of captured particles increases (see Fig. 2c). This is evidently caused by the fact that a shorter time passes until attainment of a specified dose, and consequently a smaller number of particles have time to be liberated into the vacuum during this time. If the diffusive mobility of the particles is high, then $N_s < N_0$ with complete liberation upon heating, i.e., part of the deuterium escapes in the interval t_2-t_3 (see Fig. 1a). In this case the capture coefficients measured from the gas generation spectra turn out to be smaller than those measured from re-emission during irradiation.

It is shown in Fig. 3a how the time ($t_\alpha = t_3 - t_2$) and the exposure temperature after irradiation T_α affect the number of particles which have remained in the sample. It is evident that as t_α and T_α increase the number of particles in the target decreases (N_s is measured). In the absence of the action of an ion beam this may be caused only by thermally stimulated processes of diffusion and gas generation. It is evident that first of all particles which are bound most weakly should be liberated most rapidly. This is precisely what is shown by Fig. 3b — as the time t_α increases the low-temperature peaks, which characterize weakly bound particles, decrease in the thermodesorption spectra obtained after irradiation and subsequent exposure in a vacuum. It is shown in Fig. 3c that a decrease in the flux density leads to a similar effect due to an increase in the time of irradiation to a specified dose. However, it is evident from a comparison of curves 2 and 3 of Fig. 3c that at the identical temperature ($T_i = T_\alpha$) the gas generation proceeds more strongly in the course of irradiation than after it. Actually, for a dose of $6 \cdot 10^{17}$ deuterons/cm² and a flux density of $1 \cdot 10^{15}$ deuterons/(cm²·sec) the irradiation time amounts to ~10 min (curve 2), and for a flux density of $3.4 \cdot 10^{14}$ deuterons/(cm²·sec) it amounts to about 30 min (curve 3). Curve 2 is obtained 60 min after the irradiation, and curve 3 — in 10 min. Thus although the overall time for curve 2 is about 70 min, it is only ~40 min for curve 3, and curve 2 lies above curve 3. This may indicate the existence of radiatively stimulated processes of gas liberation during ion imbedding.

It is shown in Fig. 4 how the energy of the ion beam affects the capture coefficients and the gas generation spectra. It is evident from Figs. 4a and b that at 280°K $\bar{\eta}(E_d)$ and $\eta(E_d)$ increase. This may be caused by an increase in the range depth, i.e., the diffusion path from the imbedding zone to the boundary, from which gas liberation occurs, and by an increase in the number of lattice defects which are capable of strongly binding deuterons.
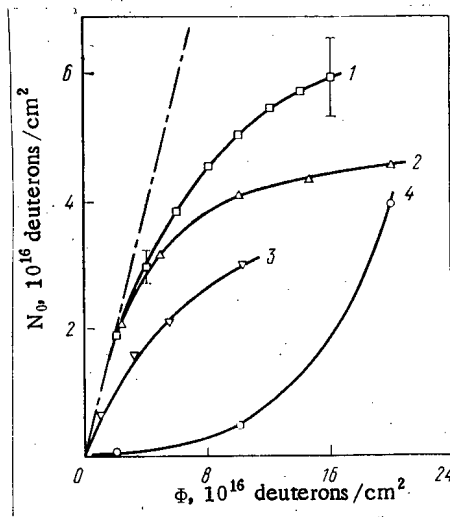
537

Fig. 6. Dose dependences of the number of deuterons absorbed
in molybdenum: 1) data of this paper with E_d = 5 keV, I = $6 \cdot 10^{13}$
deuterons/(cm²•sec), and T_i = 280°K; 2) [9], E_d = 6 keV, I =
$1 \cdot 10^{15}$ deuterons/(cm²•sec), and T_i = 300°K; 3) [5], E_d = 8 keV,
I = $1 \cdot 10^{13}$ deuterons/(cm²•sec), and T_i = 300°K; and 4) [7], E_d =
9 keV, the value of I is not indicated, and T_i = 300°K ($-\bullet-$
represents η = 1).

Actually (see Fig. 4b), for a low irradiation temperature, at which diffusion is "frozen,"
the capture coefficient is close to unity over the entire energy range investigated: The dif-
fusion path at low temperature is much less than the mean free path of the ions and no gas gen-
eration occurs independently of what distance the particles are located from the surface.
Moreover, it follows from Fig. 4c that the higher the ion energy, the more particles are con-
tained in traps with a high binding energy. Upon an increase of temperature diffusion of
deuterium in the imbedding solution and the liberation of deuterium from weakly bound defects,
the fraction of which decreases as the ion energy increases, are possible; therefore, $\tilde{\eta}(E_d)$
at 280°K increases in Fig. 4b. The role of defects has been discussed in more detail in [12,
13].

The effect of the irradiation temperature is shown in Fig. 5. The capture coefficient de-
creases comparatively rapidly to zero as the temperature increases. The number of particles
which are retained in the molybdenum at the increased temperature is determined by the number
and type of lattice defects. As T_i increases first the deuterons contained in the metal with
a low binding energy escape into the vacuum. This is clearly visible from Fig. 5d — as T_i in-
creases the low-temperature peaks in the $j_g(t)$ spectra gradually decrease and disappear. Such
a transformation of the gas generation spectra confirms in addition that upon heating after
irradiation actually the gas generation curves consist of several peaks, since in the opposite
case a proportional decrease of the entire curve as a whole would be observed.

The majority of the known data on absorption of deuterons in molybdenum has been obtained
for different irradiation parameters. Therefore, their comparison is often difficult. The
dose dependences of the number of captured deuterons according to the data of [5, 7, 9] and
this paper are presented in Fig. 6 as an example. It is evident that the discrepancy in the
results is large, although the irradiation parameters are similar. One can draw the invalid
conclusion from Fig. 6 that the number of captured particles decreases as the ion energy in-
creases. Analysis of the effect of the different experimental parameters permits sorting out
the causes of the mismatch of curves 1-4 of Fig. 6. Curves 1 and 2 are obtained by direct
measurements of the reverse gas flows directly in the irradiation process, and curves 3 and
4 are obtained some time after the the end of irradiation. As follows from Fig. 3a, one
should expect in the latter case a decrease in the number of particles in the target. There-
fore, just curves 3 and 4 lie below curves 1 and 2 in Fig. 6. Moreover, for measurements af-
ter the end of irradiation the time interval t_2-t_3 between irradiation and measurement is
significant (see Fig. 1). However, it is not indicated in [5, 7]; therefore, the discrepancy
between them should not be surprising. In addition, the difference between curves 3 and 4
is possible due to the different methods of determination of the deuterium content; curve 3

is obtained by the method of nuclear reactions in a layer ~0.5 μm thick, and curve 4 is obtained by the method of surface etching with simultaneous recording of gas generation. In the latter case the layer being analyzed is smaller, and the instrumental error is greater at a low deuterium concentration. The difference between curves 1 and 2, which are obtained by the identical method, can be explained as the effect of the irradiation temperature. Notwithstanding the fact that the ion energy and the flux density for curve 2 are higher, one could, according to Figs. 2 and 4a, expect a larger value of N_0; the temperature for curve 2 is somewhat higher, and this can lead to lower values of the capture efficiency (see Fig. 5a).

Conclusions. The capture parameters of deuterium ions in molybdenum have been studied in this paper. It has been shown that the capture coefficients decrease as the dose and the irradiation temperature increase and they increase as the energy and flux density of the ions increases. Upon heating after irradiation or exposure in a vacuum even at room temperature the number of deuterons captured in molybdenum decreases. At a raised temperature the capture coefficients measured from the gas generation spectra with heating after irradiation turn out to be smaller than the coefficients measured from the gas generation right during the irradiation. It has been established in measurements of the spectra of deuterium gas generation that the accumulation of deuterium in molybdenum occurs with a different binding energy of the deuterons in the metal. As the deuterium accumulates in the sample, those sites at which the deuterium is most strongly bound are gradually filled up and saturated. At large doses most of the deuterium is poorly retained in the metal and can be liberated into a vacuum either in the course of irradiation or during the subsequent heating. First of all, the deuterium is liberated most rapidly from the weakly bound states. It has been shown that in addition to thermal gas generation processes there is gas generation stimulated by the ion beam retarded in the sample. The contribution of radiatively stimulated gas generation at a low temperature and a high irradiation dose is especially important. A comparative analysis has been made of the results obtained by different authors, and the possible causes for the discrepancy between the experiments have been explained. It has been shown that the various results can be produced both by a difference in the irradiation parameters (which are sometimes assumed without justification to be unimportant and are not even indicated in the papers) and by a difference in measurement procedures.

<div style="text-align:center">LITERATURE CITED</div>

1. N. P. Katrich, At. Energ., 26, No. 3, 307 (1969).
2. A. A. Pisarev, V. M. Sotnikov, and V. G. Tel'kovskii, in: Collection of the Lectures of the Second All-Union Symposium "The Interaction of Atomic Particles with a Solid Body," ONTI IAÉ, Moscow (1972), p. 240.
3. S. Erents, Vacuum, 24, No. 10, 445 (1974).
4. G. McGracken, Rep. Prog. Phys., 38, 241 (1975).
5. S. Picraux, J. Bøttiger, and N. Rud, J. Nucl. Mater., 63, 110 (1976).
6. C. Braganza, G. Carter, and G. Farrell, Nucl. Instrum. Methods, 132, 679 (1976).
7. V. Kh. Alimov, A. E. Gorodetskii, and A. P. Zakharov, Dokl. Akad. Nauk SSSR, 253, No. 1, 88 (1980).
8. R. Schulz, R. Behrisch, and B. Scherzer, J. Nucl. Mater., 93-94, Part B, 608 (1980).
9. R. Yamada et al., J. Nucl. Mater., 101, 100 (1981).
10. S. Erents and G. McGracken, Brit. J. Appl. Phys. (J. Phys. D), 2, Ser. 2, 1397 (1969).
11. A. A. Pisarev, V. G. Tel'kovskii, and V. N. Tsyplakov, At. Energ., 51, No. 1, 31 (1981).
12. A. A. Pisarev and V. N. Tsyplakov, Zh. Tekh. Fiz., 49, 1758 (1979).
13. A. E. Gorodetskii, A. P. Zakharov, and V. M. Sharapov, Zh. Fiz. Khim., 54, No. 11, 2874 (1980).

DEHYDRATION OF THE STEAM-GENERATING CHANNEL DUE TO
COOLING LOOP DEPRESSURIZATION

É. I. Liverant, A. P. Proshutinskii,   UDC 621.039.586.024.44
and E. M. Staviskii

The design of safety systems for nuclear power plants must be based on a knowledge of the processes involved in the development of emergency situations. Among the important characteristics of accidents connected with depressurization of the circulation loop are the time before the start of critical fuel-element heating (time of dehydration of the reactor's steam-generating channel) and the dynamics of variation in the coolant discharge and density.

The dehydration time τ_{cr} was calculated in [1] on the basis of the model of homogeneous coolant expansion from the time of instantaneous discharge drop to the relative enthalpy level $x = 1$. The initial steam content along the channel was taken into account in [2]. However, the change in the coolant discharge at the channel inlet during the time of the drop and the slippage factor in coolant entrainment were not considered. Moreover, the variations in the coolant density and discharge during the dehydration process were not estimated in these papers.

The proposed method makes it possible to calculate the value of τ_{cr} and the coolant parameters: the relative enthalpy, the density ρ, and the velocity W, during the dehydration process. The model takes into account the duration of the drop stage and the time of final evaporation of the moisture remaining in the film on the wall after removal of the steam-water flow from the flow core. The model is based on the following assumptions: With the drop in the discharge, the coolant velocity at the channel inlet W_{in} varies exponentially; entrainment of the liquid from the flow core occurs in the process of homogeneous expansion for a pressure p and thermal load q that are constant with respect to the time τ and the coordinate z; after the liquid has left the flow core, there remains on the channel wall a film, whose parameters can be determined by means of the relationships for a steady-state annular dispersion flow.

Calculation of the Removal Stage. The variation in the coolant velocity at the channel inlet is given by

$$W_{in}(\tau) = W_a \exp(-\Omega\tau), \tag{1}$$

where W_a is the velocity before the application of perturbation ($\tau = -0$); and Ω is a parameter determining the rate of the discharge drop ($\Omega = \infty$ corresponds to the instantaneous drop in discharge).

According to [3], the equations of energy and mass conservation, transformed for a Lagrangian coordinate system, are given by

$$Dx/D\tau = \Gamma[v'/(v'' - v') + x(\tau, z)]; \tag{2}$$
$$dz/d\tau = W_{in}(\tau) + \Gamma[z - z_0(\tau)], \tag{3}$$

where $\Gamma = 4q(v'' - v')/rd$; v' and v'' are the specific volumes of water and steam at the saturation line, r is the evaporation heat, z_0 is the coordinate of the incipient boiling boundary, and $d = 4f/\Pi_{he}$ is the thermal diameter of the channel (f is the through cross section, and Π_{he} is the heated perimeter).

Solving Eq. (2), we find the time of arrival of a liquid particle at the incipient boiling boundary:

$$\tau_0 = \frac{\tau}{\Gamma} \ln[1 + x(\tau, z)(v''/v' - 1)]. \tag{4}$$

In order to solve Eq. (3), we must know the relationships governing the displacement of the

---

incipient boiling boundary, which, with an allowance for expression (1), have the following form:

for $\tau_0 \le 0$

$$z_0(\tau_0) = W_a \tau_e, \tag{5}$$

where $\tau_e = \Delta i_u d/(4qv')$ is the time of coolant motion through the economizer section, and Δi_u is the enthalpy of underheating of the liquid with respect to saturation at the channel inlet.

For $0 < \tau_0 \le \tau_e$

$$z_0(\tau_0) = W_a(\tau_e - \tau_0) + \frac{W_a}{\Omega}[1 - \exp(-\Omega\tau_0)]; \tag{6}$$

while, for $\tau_0 > \tau_e$

$$z_0(\tau_0) = \frac{W_a}{\Omega}\exp(-\Omega\tau_0)[\exp(\Omega\tau_e) - 1]. \tag{7}$$

The position of the incipient boiling boundary z_0 at any instant of time τ is determined from the condition $\tau_0 = \tau$.

With an allowance for expressions (5)-(7), Eq. (3) has four solutions:

1) before the onset of perturbation:

for $\tau \le 0$ and $\tau_0 \le 0$, the solution of Eqs. (3) and (4), (5),

$$x(-0, z) = \frac{4qv'}{dr\,W_a}(z - W_a\tau_e); \tag{8}$$

2) for $0 < \tau \le \tau_e$; $\tau_0 < \tau_e$, the solution of Eqs. (2) and (4), (6):

$$x(\tau, z) = \frac{4qv'}{dr}\left[\frac{z + W_a(\tau - \tau_e)}{W_a} - \frac{1 - \exp(-\Omega\tau)}{\Omega}\right]; \tag{9}$$

3) for $\tau > \tau_e$; $\tau_0 \le \tau_e$, with an allowance for expressions (4), (7):

$$x(\tau, z) = \frac{v'}{v'' - v'}\left\{\frac{z\Gamma}{W_a} + \frac{\Gamma}{\Gamma + \Omega}\left[\frac{1 - \exp(-\Omega\tau_e)}{\Omega}\Gamma + 1\right]\exp(-\Omega\tau) + \Omega\frac{\exp[\Gamma(\tau - \tau_e)]}{\Gamma + \Omega} - 1\right\}; \tag{10}$$

4) for $\tau > \tau_e$; $\tau_0 > \tau_e$:

$$x(\tau, z) = \frac{v'}{v'' - v'}\left(\left\{\frac{z(\Gamma + \Omega)}{\Omega}\exp[\Omega(\tau - \tau_e)] + \exp(-\Omega\tau_e)\left[1 + \Gamma\frac{1 - \exp(\Omega\tau_e)}{\Omega}\right]\right\}^{\Gamma/(\Gamma + \Omega)} - 1\right). \tag{11}$$

Equations (9) and (10) determine the steam content at the z section at the instant of time τ for a liquid particle that is located in the channel when the perturbation occurs. Equation (11) determines the steam content at the z section at the instant of time τ_{en} for a liquid particle that is located outside the channel. In accordance with Eq. (4), at the onset of perturbation, a liquid particle is located in the evaporation section for $\tau_0 < 0$, in the economizer section for $0 \le \tau_0 \le \tau_e$, and outside the channel for $\tau_0 > \tau_e$. Equations (4) and (8)-(11) can be used for calculating either the steam content of the flow for an exponential stoppage of coolant supply to the channel for any values of z and τ or the liquid entrainment time τ_{en} for the corresponding values of x and z. For an instantaneous drop in the discharge ($\Omega = \infty$), the solution of Eq. (10) with respect to τ_{en} for $x = 1$ coincides with the expression derived earlier for calculating the dehydration time on the basis of the homogeneous coolant expansion model [2]:

$$\tau_{en} = \tau_e + \frac{1}{\Gamma}\ln\left(\frac{v''}{v'} - \frac{\Gamma z}{W_a}\right). \tag{12}$$

The coolant density and velocity are calculated by means of the expressions

$$\rho(\tau, z) = [v' + x(\tau, z)(v'' - v')]^{-1}, \tag{13}$$

$$W(\tau, z) = W_{in}(\tau) + \Gamma[z - z_0(\tau)]. \tag{14}$$

541

Calculation of the Final Evaporation Stage. The relative discharge of the liquid remaining in the film on the channel wall at the end of liquid removal from the flow core is estimated by means of the expressions given in [4], which generalize the results of investigations of steady-state annular dispersion flow in a tube with d = 13 mm for the following ranges of operating parameters: p = 1.0-10.0 MPa; ρW = 500-4000 kg/(m²·sec); x = 0.1-0.9,

$$x_{fm} = 0.235 \, (v''/v')^{0.12} \, y^n, \tag{15}$$

where $y = 0.01\sigma/W_{fm}\mu''$; for y < 1; n = 2.1; for y > 1, n = 0.67; σ is the surface tension of water; and μ'' is the dynamic viscosity of steam.

In accordance with [4], the film velocity W_{fm} is determined from the relationship

$$\lg \frac{W}{W_{fm}} = 0.6 \left(\frac{\rho W}{1000}\right)^{0.3} (1 - x_{fm})^{0.7} + 0.0272 \left(\frac{v''}{v'}\right)^{0.7} . \tag{16}$$

The obtained values of x_{fm} and W_{fm} are used to determine the percentage of the cross section occupied by the film:

$$\varphi_{fm} = 1 / \left[1 + \frac{v'' (1 - x_{fm}) W_{fm}}{v' x_{fm} W} \right] . \tag{17}$$

The film thickness is given by

$$\delta_{fm} = \varphi_{fm} d/4. \tag{18}$$

The time of final film evaporation after the film is no longer replenished is equal to

$$\tau_f = \delta_{fm} r/qv'. \tag{19}$$

Sequence of Calculations of the Dehydration Time. We shall determine the values of W, x_{fm}, $\overline{W}_{fm}$, δ_{fm}, and τ_f for the final stage of the removal process by using Eqs. (15)-(19). The calculation is performed for the most critical, the outlet, section of the channel (z = L). We assume that z_0 vanishes in Eq. (14). The calculation of the entrainment stage is performed up to x = 1 − x_{fm}. The choice of the equation for calculating τ_{en} is determined on the basis of (4). In using Eqs. (9) and (10), τ_{en} is determined by means of iteration, while Eq. (11) is solvable with respect to time.

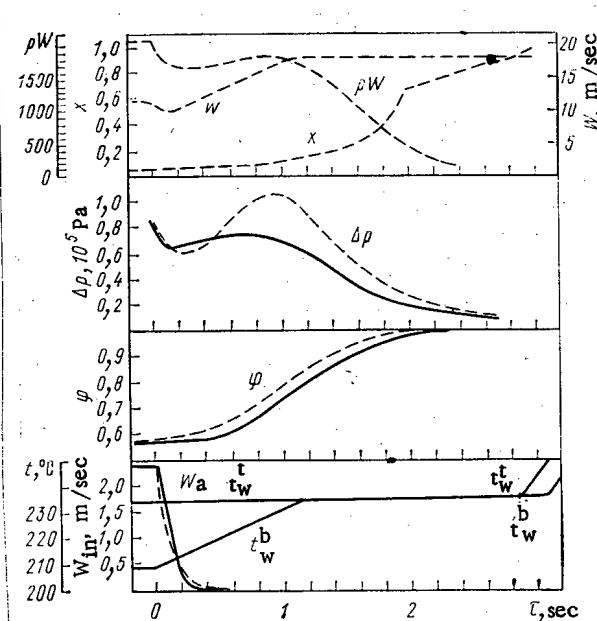Fig. 1. Behavior of the parameters during the dehydration process for a tube with d = 10 mm and L = 5 m for p = 3.0 MPa and q = 0.25 MW/m²; W_a = 2.5 m/sec; Δt_a = 25°C. -----) Calculation based on the described method; ———) experiment [5].
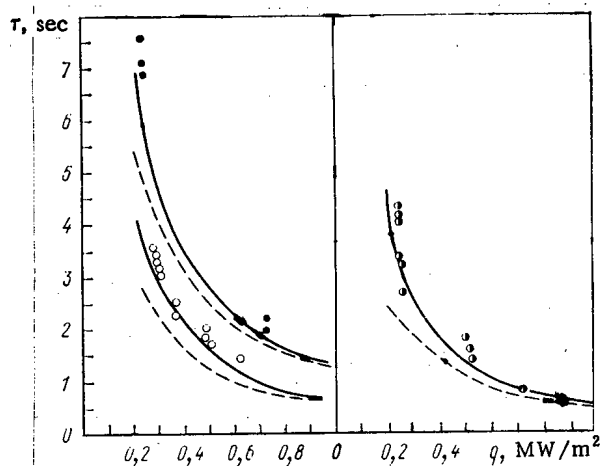
Fig. 2. Dehydration time as a function of the **thermal flux**
density for a tube with d = 10 mm and L = 5 m; ρW_a = 2100 kg/
$(m^2 \cdot sec)$. The theoretical data are represented by ———— for
τ_{cr} and ––––– for τ_{en}. The experimental values of τ_{cr} are
given by the following: (●) p = 7.0 MPa; Δt_a = 100°C; (○) p =
7.0 MPa; Δt_a = 25°C; (◐) p = 3.0 MPa; Δt_a = 25°C.

Figure 1 shows the behavior of the parameters during the process of water removal from a
vaporization tube with d = 10 mm and L = 5 m for p = 3.0 MPa, q = 0.25 MW/m^2, W_a = 2.5 m/sec,
and Δt_a = 25°C. The parameters calculated according to the proposed method are compared with
the experimentally obtained [5] oscillograms of the velocity at the tube inlet W_a, the pres-
sure drop Δp, the actual volumetric steam content in the upper part of the tube φ, and the
wall temperatures at the top and bottom tube sections t_w^t and t_w^b. The value of W_a is calcula-
ted by means of Eq. (1) for Ω = 10. The variation of the overall pressure drop for the tube
Δp is determined as a function of the parameters x, ρW, and W, averaged over the length, with-
out considering the variation of the friction coefficients λ. In correspondence with the
model of homogeneous expansion during the entrainment stage, the theoretical value of $\varphi(x)$ is
set equal to the volumetric discharge steam content. The initial values of Δp and φ (for $\tau \leq$
0) are used as the reference values in calculations.

The assumed exponential velocity decrease at the inlet for Ω = 10 is close to the actual
law, while the behavior of the calculated values of φ and Δp conforms to the experimental data.
Certain discrepancies between the theoretical values of φ and Δp and the experimental data
can be explained by slippage of the vapor stage and by changes in λ during the dehydration
process. The theoretical dehydration time τ_{cr} and the time during which the liquid is heated
to saturation τ_e correspond to the experimentally recorded changes in the wall temperature.

Figure 2 provides a comparison between the theoretical values of τ_{cr} and the experimental
data [5] for p, t_{in}, and q, which indicates a satisfactory agreement between the calculations
based on the proposed method and the experimental data in a wide range of operating parame-
ters.

LITERATURE CITED

1. P. Griffith, J. Pearson, and R. Lepkowski, Nucl. Safety, 18, No. 3, 298 (1977).
2. E. M. Staviskii et al., Heat Exchange, VI [in Russian], Vol. 6, Izd. Inst. Teplomassoob-
   mena, Akad. Nauk BSSR, Minsk, 1980, Part 1, p. 35.
3. B. Shiralkar, L. Schnebly, and R. Lahey, Nucl. Eng. Design, 25, No. 3, 350 (1973).
4. B. I. Nigmatulin, V. I. Milashenko, and V. E. Nikolaev, Teplofiz. Vys. Temp., 16, No. 6,
   1258 (1978).
5. I. S. Dubrovskii et al., in: Safety Problems in Atomic Power Plants and Problems of
   Scientific Research [in Russian], Atomizdat, Moscow (1979), p. 70.

STUDYING THE ELECTROPHYSICAL PARAMETERS OF PIEZOCERAMICS OF VARIOUS

TYPES IN AN IVV-2M REACTOR

Yu. P. Meleshko, S. V. Babaev,
S. G. Karpechko, V. I. Nalivaev,
Yu. A. Safin, and V. M. Smirnov

Various articles [1-4] report investigations into the effects of reactor radiation on the electrophysical characteristics of various types of piezoceramics. However, the conclusions drawn regarding the behavior of this material when subjected to ionizing radiation do not enable us to choose the type of piezoceramic best suited to transducers for measuring the pulsations in pressure of currents of liquid or gas directly in the core of the reactor. For example, [2] reports the results of a study into the electrophysical characteristics of type TsTS ceramic, in which the piezo modulus is measured indirectly. The resultant data are ambiguous, insofar as the changes in the piezo modulus can be masked or accentuated by the effects or combinations of the effects of radiation on the structural members of the test equipment itself.

The present article determines the relationship between the resistance, capacitance, and tan delta of the piezoceramics manufactured in the Soviet Union (types TsTS-19, TsTS-26, TV-1, TSVM-1) and employed in piezoelectric transducers, together with the relationships between the signals generated by these transducers and the power of the γ radiation and neutron fluxes to which they are exposed. The signals were measured while the testpiece was subject to the direct mechanical effects of pressure pulses.

In the case of experimental reactor type IVV-2M [5], the transducers are loaded into irradiation channels (Fig. 1) consisting of a carrier tube 1 in which 16 transducers 3 are connected with the aid of tube 2 (up to four transducers in each level). Hood 5 serves to protect the transducers from mechanical damage; this has holes for the passage of circulating water to cool the transducer during the experiments. Body 10 of the transducer carries the piezoceramic samples to be studied in bush 11 made of Al_2O_3. Each of these takes the form of a disk 12, 6 mm in diameter and 1 mm thick, with contacts 13 which are pressed with a force of 100 N against diaphragm 7 of the transducer by nut 15, via washer 14 made of Al_2O_3. Connection line 7 from the transducers to flange 6 consists of copper conductors, insulated from the protective steel capillary in which it is run by a sleeve of Al_2O_3. Coaxial cable 8 is protected from the reactor water by casing 9. The effect that the radiation has on the connecting line is monitored by two lines 21 acting as controls, identical with the connecting line. Conductors 16 of the line are fixed in holes in tube 17, while capillary 18 is sealed by cover 19. Each level contains transducers with piezoceramics of one particular type. One of the transducers serves a temperature model 4. The precalibrated hot junction of a thermocouple 20 is introduced into the center of piezoceramic testpiece 12 to determine its temperature during the course of the experiment.

Before the test began, the lower part of the radiation equipment carrying the transducers was loaded into a vessel filled with water which was then heated from 10 to 80°C. Measuring the electrophysical parameters of each testpiece during this rise in temperature enables us to separate the temperature effects from the effects due to radiation when the results are subsequently processed.

The investigation was carried out with the reactor operating at power levels of 0, 1, 2, 4, 6, 8, 10, and 12 MW. The activation method, using cobalt and indium foils, was used to determine the density of thermal and fast ($E \geq 1.15$ MeV) neutrons. These proved to be $7.7 \cdot 10^{12}$ and $5.5 \cdot 10^{11}$ cm^{-2}·sec^{-1}, respectively, at the site of the transducers when the reactor was running at 1 MW. The exposure to γ radiation proved to be 7.2 A/kg, when measured on a KTV gamma chamber. The flux of thermal neutrons at the end of the test was $1.8 \cdot 10^{19}$ cm^{-2}, while the flux of fast neutrons was found by the method of calculation and experiment described in [6] to be $1.9 \cdot 10^{18}$ cm^{-2}. The exposure to gamma radiation was $1.7 \cdot 10$ C/kg.
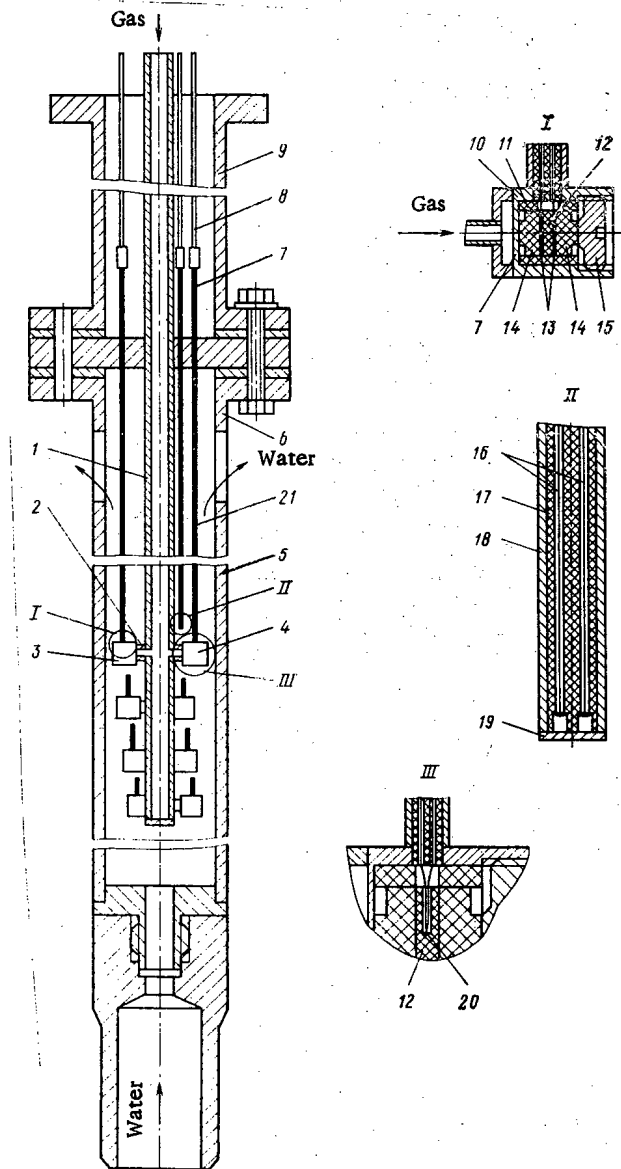
Fig. 1. The radiation equipment.

The temperature of the piezoceramic testpieces was found during the course of the experiment from the evolution of energy in the structural members of the transducers, the temperature of the reactor circulating water, and the cooling of the transducers. This varied from 10 to 35°C. The temperature, resistance, capacitance, and tan delta of the testpieces were measured at all reactor power levels, together with the signals generated by the transducers, while the resistance and capacitance of the cables acting as controls were also measured.

The resistance of the testpieces were measured by a type VK7-9 instrument. The measurement error on the range selected (×100 MΩ) was 4% of full scale deflection. It would appear that the measured resistance is made up of the resistance of the cable, testpiece, and the contacts between. Since the resistance of the cable serving as control (without transducers) was more than 5000 MΩ, we are justified in assuming that the principal components in the measured values are the resistances of the piezoelement and the resistance between the contacts and the body of the transducer.

The resistance of all the testpieces proved to be 5000 MΩ or more prior to loading the radiation equipment into the reactor. When the reactor was brought up to rated power, the resistance of all the testpieces was observed to fall, due to the action of γ radiation. The relationship between the resistance of the three type TsTS-19 testpieces and the exposure to gamma radiation is given in Fig. 2. This relationship, exponential in nature, is characteristic of samples of all the types of piezoceramic, the numerical features being determined by

545

the methods employed to manufacture the particular transducers. The present authors did not observe any influence between the flux levels achieved and the resistances of the types of ceramic tested.

The capacitances of the piezoelements were found by means of a type E7-11 instrument, which enabled us to measure the transfer impedances of the testpieces, so that the capacitance of the piezoelement alone could be measured by the three-electrode connection scheme, excluding the capacitance of the conductors in the process. This proved to be 430 pF for the TsTS-19, 450 pF for the TsTS-26, 70 pF for the TSVM-1, and 30 pF for the TV-1.

Measurements carried out immediately after the radiation equipment was loaded into the reactor at zero power level showed that a clear reduction in the capacitance of all the testpieces took place (after temperature correction has been applied, both here and in subsequent figures). Since the main ionizing factor in the radiation at zero power level is γ radiation ($7.2 \cdot 10^{-2}$ A/kg at the site of the transducers), we can assume that the fall in capacitance is due to an effect of γ radiation on the structure of the piezoceramic. By assuming that the main factor affecting the capacitance when the reactor is operating at low flux levels will be γ radiation, we can plot a relationship between the capacitance of the piezoceramic and the power of the exposure to γ radiation. Such a relationship, characteristic for all samples of piezoceramic types TsTS-19 and TsTS-26, is given in Fig. 3. When the reactor attains its rated power level, further operation up to the end of the tests shows a steady reduction in the capacitance of the testpieces of all types of piezoceramic. Figure 4 shows the averaged relationships of the capacitance of the testpieces and the tan delta due to a flux of fast neutrons. We should note that the capacitances at the end of the test were 40% for TsTS-19, 45% for TsTS-26, and 20% for TV-1 and TSVM-1 of the value measured prior to loading, which is qualitatively confirmed by the data in [1, 3] obtained when measuring the capacitances of samples recovered from a reactor.

When acting on a diaphragm (and, consequently, on the samples of piezoceramic), a pressure pulse causes the transducer to emit a signal proportional to the piezomodulus of the testpiece. This signal was measured both by a commercially available type LKh 7005 piezostation and also by a charge-sensitive amplifier [7] used with an N117/1 light-beam oscillograph. The slope of the rising part of the pressure pulse applied to the diaphragm of the transducer was ~20 MP/sec, while the maximum pressure in the pulse was 1.5 MPa.

When developing the method of testing, we found that the maximum spread in the amplitudes of the pressure pulses did not exceed 2%, while the error did not exceed 3% before or after the measurements, when calibrating the measurement channel. We should bear in mind that the
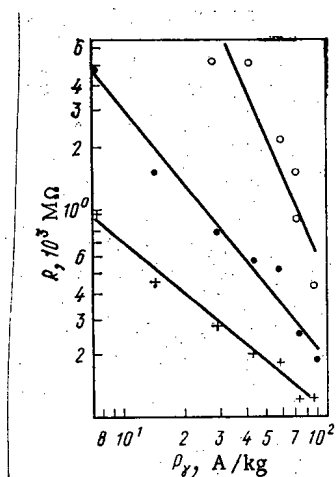

Fig. 2

Fig. 3

Fig. 2. Relationship between the resistance of piezoceramic TsTS-19 and the exposure power of gamma radiation: +) sample No. 1; ●) sample No. 2; ○) sample No. 3.
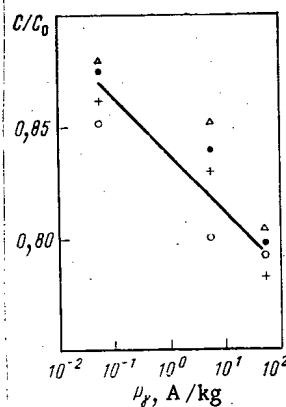
Fig. 3. Relationship of the capacitance of piezoceramics to γ radiation exposure dose: +) sample No. 1 (TsTS-19); ●) sample No. 2 (TsTS-19); ○) sample No. 5 (TsTS-26); Δ) sample No. 6 (TsTS-26).

546
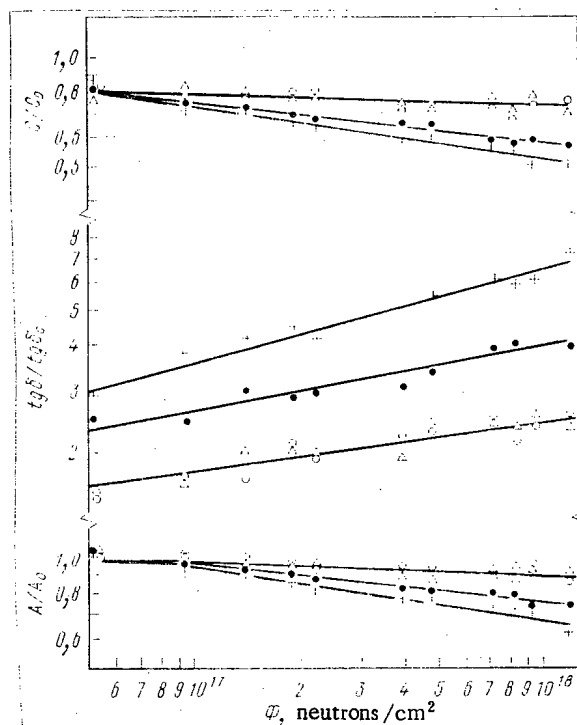
Fig. 4. Relationship of capacitance, tan delta, and signal
amplitude due to flux of fast neutrons: +) TsTS-26; ●) TsTS-
19; ○) TV-11; △) TSVM-1.

relative change in the amplitude of the signals, measured by the piezostation and charge-sensi-
tive amplifier during the experiment, coincided with each other within the limits of experi-
mental error. The relationship of the transducer signals to the flux of neutrons is seen in
Fig. 4.

During the initial stage of the experiment, the neutron-flux density, the power of the
γ-radiation exposure, the neutron flux, and the temperature of the piezoelements all affected
the piezomodulus of the testpieces and therefore the signal. It is probable that the first
three factors can only act to reduce the signal, while laboratory tests have shown that a
temperature increase from 10 to 35° leads to a negligible increase in the signal. Neverthe-
less, we can see from the graph that when instabilities in the system of forming the pressure
pulse applied to the transducers are taken into account, together with the errors in the sys-
tem of measurement at the point where the reactor attains rated load, these factors have no
apparent effect on the signal. Following this point, the errors tend to increase steadily.
This behavior is characteristic of testpieces of all types of piezoceramic. The signal at
the point where a flux of neutrons is attained is reduced by 25% for TsTS-19, by 25-30% for
TsTS-26, and by 10% for TV-1 and TSVM-1.

Consequently, the numerical characteristics describing the influence of reactor radia-
tion on the main electrophysical parameters of four types of piezoceramic produced by Soviet
industry have been obtained with the aid of the proposed radiation equipment. This enables
us to use piezoceramic materials to best effect as a transducer in various measuring devices
operating under conditions of reactor radiation.

LITERATURE CITED

1. V. M. Baranov, Ultrasonic Measurements in Nuclear Engineering [in Russian], Atomizdat,
   Moscow (1975).
2. V. V. Sarkisyan, G. I. Sochilin, and N. V. Markina, "Features of methods for irradiating
   radiation-resistant piezoceramic materials," in: Collection of Papers, All-Union School
   of Investigations Within Reactors [in Russian], Dmitrovgrad, November 21-25, 1977.
3. G. Broomfield, J. Nucl. Mater., No. 1, 91 (1980).
4. V. M. Baranov, S. P. Martynenko, and A. I. Sharapa, At. Energ., 53, No. 5, 337 (1982).
5. B. B. Baturov et al., Vopr. At. Nauki Tekh., Ser. Fiz. Tekh. Yad. Reaktorov, No. 1(21),
   Part 2, 9 (1978).

6.   V. I. Zelenov et al., Theses, Third All-Union Conference on the Metrology of Neutron Rad-
     iation in Reactors and Accelerators [in Russian], Gosstandart, No. 91 (1982).
7.   G. I. Sochilin et al., Vopr. At. Nauki Tekh., Ser. Radiatsion. Mater., No. 1(7), 3 (1976).

USE OF MONOISOOCTYLMETHYLPHOSPHONIC ACID AND ITS TRIVALENT IRON

SALT IN DETERMINING RADIONUCLIDES IN EFFLUENTS

N. E. Tsvetaeva, V. M. Filin,   UDC 628.3:543.53
L. A. Ivanova, V. N. Revnov,
E. P. Rodionov, L. Ya. Kudaya,
I. A. Suslin, and K. Yu. Shapiro

It is possible to determine the biologically most hazardous radionuclides ^{90}Sr, ^{137}Cs,
^{239,238}Pu, ^{241}Am, and so on in effluents at the level of 0.1 MPC if large concentration fac-
tors can be provided during the extraction. Methods exist for determining small amounts of
^{90}Sr (from ^{90}Y), plutonium, and other radionuclides in aqueous solution by the use of liquid
extraction with tri-n-butyl phosphate (TBP) [1–3], di(2-ethylhexyl)phosphoric acid (D2EHPA)
[4–6], trialkylphosphine oxides [7], and other reagents.

During the last decade, it has become common to use solvent–extraction methods in analyz-
ing for radionuclides in aqueous solution by the use of a salt of trivalent iron (a "miom-
phate") — a solid organic phase as formed by extraction of trivalent iron with monoisooctyl-
methylphosphonic acid (MIOMPA) [8–18] — whose properties are similar to those of D2EHPA [5]
(Fig. 1). Aqueous solutions containing nitric and hydrochloric acids when used with MIOMPA
show good extraction of Y, Pu(III), Pu(IV), Pu(VI), U(VI), Fe(III), Ce(IV), Zr, and Nb (dis-
tribution coefficients $D \geq 10^3$ between the organic and aqueous phases); however, MIOMPA hard-
ly extracts group I and II elements ($D \ll 1$).

Over a wide acidity range (from pH 7 up to 4 moles/liter), MIOMPA $(HR)_2$ forms a solid
organic phase, trivalent iron miomphate $FeR_3(HR)_3$. When metals in trace concentrations are
extracted, the principle is that of hybrid concentration of the nuclides Y, Pu(III), Pu(IV),
and Pu(VI), which involves a combination of liquid extraction by MIOMPA and isomorphous co-
precipitation of the nuclides with the trivalent iron miomphate [16]. This is evident for
example from a comparison of the extraction of yttrium from nitric acid solutions with MIOMPA
as a liquid and on extraction into solid trivalent iron miomphate (Fig. 2), as well as from
the rectilinear character of the coprecipitation isotherm for yttrium in trivalent iron mi-
omphate (Fig. 3). The values of D for extraction into the solid organic phase increase by
factors of tens or hundreds by comparison with solvent extraction into MIOMPA for Y and
Pu(III), Pu(IV), and Pu(VI), attaining thus 10^5–10^6.

Iron miomphate as flotated in toluene has a coarse-grained structure and is markedly
hydrophobic, and therefore the phase separation occurs in 20–30 min (during the formation
of the solid extract), which favorably distinguishes solid–phase extraction from precipita-
tion operations, where additional time is required to separate the solid. Another distinc-
tive features is that it is simple to separate the compound from the aqueous phase; a small
amount of the solid extract is rapidly and reliably separated from much larger volumes of
aqueous phase (ratio of the volumes of aqueous phase V_a and the organic phase V_o $n = V_a/$
$V_o \approx 10^3$) by passage through any convenient filter such as marl. The method retains the ad-
vantages of liquid extraction (rapidity and selectivity), while at the same time providing
a high degree of concentration (about by a factor 10^3) of the radionuclides in a single oper-
ation, which is unattainable in liquid extraction. It is readily shown that the concentra-
tion coefficient K for the organic phase can be put in the form

$$K = n/(1 + n/D). \tag{1}$$

This means that the highest radionuclide accumulation occurs for $D \gg n$, and
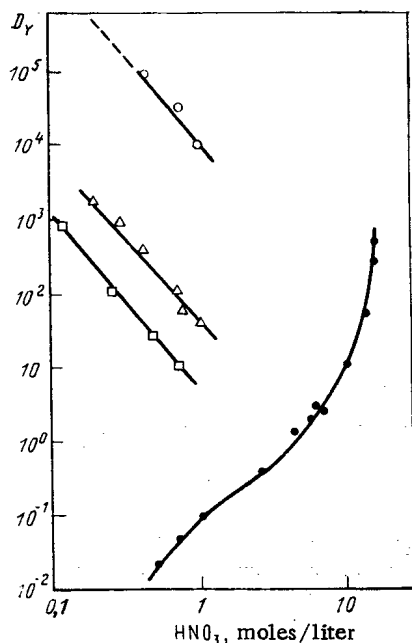
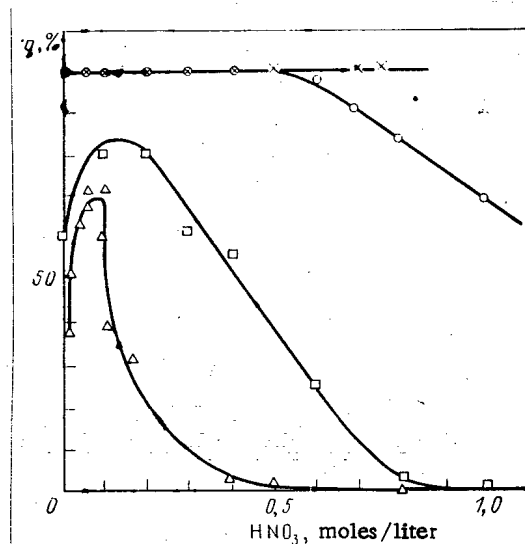Fig. 1   Fig. 2

Fig. 1. Comparison of yttrium distribution coefficients D_Y on extraction into iron miomphate as solid organic phase for $n = 10^3$ ($\bigcirc$); and on liquid extraction into MIOMPA for $n = 10^3$ (∇); into D2EHPA for $n = 1$ ($\square$); and into TBP for $n = 1$ ($\bullet$).

Fig. 2. Extraction q of yttrium into MIOMPA ($\square$) and iron miomphate ($\oslash$), and also of Ce(III) ($\triangle$) and Ce(IV) ($\times$) on extraction into iron miomphate.

$$K_{max} = n. \tag{2}$$

Conversely, if $D \ll n$, the extraction of the radionuclide into the organic phase is slight, no matter what the value of D. Therefore, to separate radionuclides with distribution coefficients D_1 and D_2 one has to have

$$D_1 \gg n \gg D_2. \tag{3}$$

The rapid separation of the solid extract from the aqueous phase with $n = 10^3-10^4$ in combination with large distribution coefficients (10^5-10^6) provides large concentration factors (of 10^3-10^4) for these radionuclides with selective or preferential extraction from mixtures with other radionuclides having distribution coefficients $\leq 10^2$. Figure 4 illustrates the scope for selective extraction for various n. Recent studies have shown that the physicochemical states of radionuclides in effluents and natural waters differ from those in simple ionic forms in various ways [20-24]. For example, the physicochemical states of strontium nuclides in effluents and natural waters are relatively stable [21], whereas the forms taken by plutonium in these waters not only differ from the initial forms but also alter over time in response to temperature fluctuations, major components, and other factors [22]. This has been utilized in methods based on MIOMPA and iron miomphate in detailed methods of determining small amounts of ^{90}Sr, (from ^{90}Y), ^{137}Cs, ^{144}Ce, ^{241}Am, and plutonium nuclides in samples of effluents, natural waters, and drinking water [8-15, 17, 18]. These methods were developed on the basis of effluent reaching the treatment plant at the Moscow treatment station, as well as samples of liquid radioactive wastes reaching the "Radon" Moscow Scientific Production Association for the Storage of Radioactive Wastes. The physicochemical state of the plutonium in the water was first established by means of successive static sorption tests on iron miomphate [17], which showed that the state of plutonium in these effluents differed from the simple ionic forms Pu(III), Pu(IV), and Pu(VI). It was also found that the plutonium was unevenly distributed over the effluent, which is evidence for colloidal or pseudocolloidal states arising from hydrolysis and the multiplicity of coordinated forms taken in these waters. One consequence of the distribution nonuniformity is that there are considerable differences in results on parallel specimens obtained by transferring small aliquots of effluent

TABLE 1. Characteristics of Methods of Nuclide Analysis for Effluent Involving Concentration on Iron Miomphate

Nuclide	Method	Sample volume, liters	Iron miomphate preparation	Detection method	$A\gamma d$, Bq/liter	PC_b^* [26], Bq/liter
^{90}Sr (from ^{90}Y)	Extraction into iron miomphate	2-5	Thick-layer (about 30 mg/cm^2)	Measurement of β activity	0,2-0,4	15
^{144}Ce (IV)	The same	5	The same	γ Spectrometry	4	400
^{137}Cs	Extraction into iron ferrocyanidomiomphate	5	" "	The same	4	500
^{241}Am	Extraction into iron miomphate	0.3	" "	γ Spectrometry of low-energy β radiation	20	70
ΣPu	Static sorption on iron miomphate with stimulating additives	0.3	Organic solution of miomphate combined with phosphor	α-Radiation measurement	0.04	80
^{239}Pu	Static sorption on iron miomphate	0.3	Thick-layer (about 20 mg/cm^2)	Measurement of α and xL radiation and identification from N_L/N_α ratio	40	80
Separate determination of ^{238}Pu and ^{239}Pu	The same	0.3	Thin-layer preparation of iron miomphate $R_e = 150$ keV)	α Spectrometry with a semiconductor detector of area 5 cm^2	4	80

*PC_b permissible radionuclide concentration in water for population use.
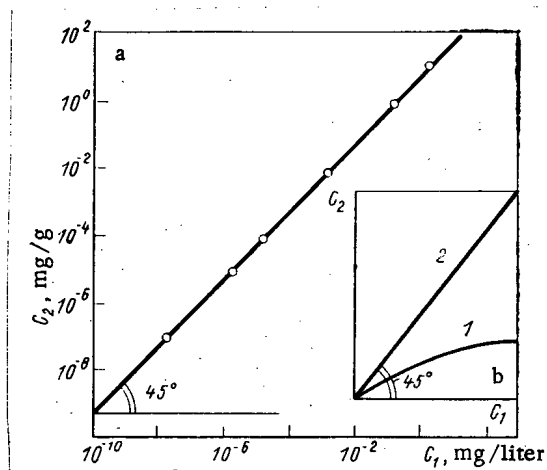
550

Fig. 3. Dependence of yttrium concentration C_2 in iron miomphate on the concentration C_1 in the equilibrium aqueous phase (a) and behavior of the isotherms for absorption (1) and iso-morphous coprecipitation (2) of the trace component with the major one (b) [19].
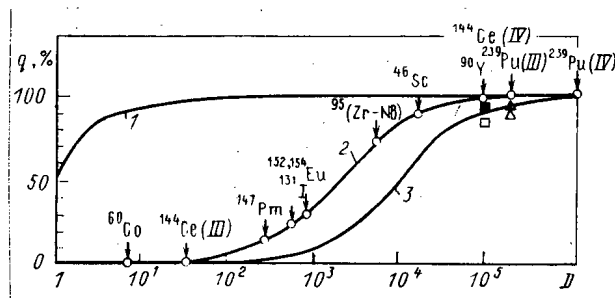
Fig. 4. Calculated values for the extraction q of radionuclides into the organic phase as functions of the distribution coeffi-cient D for a phase-volume ratio n = 1 (1); n = $2 \cdot 10^3$ (2); n = 10^4 (3); and experimental values for n = $2 \cdot 10^3$ for V_a = 5 liters ($\bigcirc$), for n = 10^4 from V_a = 5 liters ($\square$) and ($\triangle$), and with n = 10^4 from V_a = 300 ml ($\blacksquare$ and $\blacktriangle$).

onto metallic substrates. The convergence in analyses of such specimens is worse than that for specimens made from nitric acid and acetone solutions of Pu(IV) by factors of about 10 and 20, respectively.

Static sorption on iron miomphate provides high selectivity in extracting plutonium from mixtures with uranium, americium, and curium, together with a higher degree of concentration (10^4) by comparison with extraction into iron miomphate (10^3). Therefore, to determine small amounts of plutonium in water samples of volume 300 ml, one can use static sorption on iron miomphate containing stimulating additives [40 mg each of MIOMPA and Fe(III)].

A method has also been developed for determining small amounts of ^{241}Am in effluents after concentration from a water sample of volume 300 ml into iron miomphate by extraction with MIOMPA in combination with precipitation of the ^{241}Am on iron hydroxide [11]. The ^{241}Am is assayed from the 60-keV γ line from the iron miomphate by the use of a scintillation or semiconductor γ spectrometer for low-energy γ radiation, limit of detection for ^{241}Am A_{ld} = 20 Bq/liter. Various iron miomphate specimens are used in accordance with the detection meth-od: thick specimens at 20-30 mg/cm^2 for nuclides emitting γ and β radiations, or thin ones of less than 100 μg/cm^2 for α spectrometry, which are obtained by depositing small aliquots of the organic solution of the miomphate on metal substrates. Table 1 gives some character-istics of these analysis methods.

Therefore, hybrid methods of concentrating radionuclides in trivalent iron miomphate have advantages over the existing methods of precipitation, solvent extraction, and sorption in that it is possible to attain high degrees of concentration (10^3-10^4) together with selec-

tive or preferential extraction from water samples in comparatively short times (20-40 min), while the chemical operations are very simple, including the separation of the solid extract from the aqueous phase. One can prepare firm specimens of any configuration from iron miomphate, which enables one to use these methods in routine analysis.

In recent years it has been found possible to concentrate radionuclides into iron miomphate from volumes of up to 50 liters by the use of vibration [18], which reduces the limit of detection by more than a factor 10. There are prospects for improving the sensitivity in determining α-emitting nuclides in effluents by the use of α spectrometers with large-area semiconductor detectors or large α-spectrometric ionization chambers [25], which enable one to increase the areas of the thin-layer specimens correspondingly.

We are indebted to M. N. Erofeeva and É. N. Matsyna for valuable advice and assistance.

LITERATURE CITED

1. V. V. Fomin et al., Zh. Neorg. Khim., 3, No. 9, 2113 (1958).
2. I. M. Golutvina, T. A. Kazakova, and Yu. M. Nikolaeva, Meditsinskaya Radiol., 1, 62 (1962).
3. F. Ya. Rovinskii and V. V. Ispravnikova, At. Energ., 14, No. 3, 285 (1963).
4. T. Goto, J. Inorg. Nucl. Chem., 30, No. 12, 3305 (1968).
5. D. Peppard et al., ibid., 4, No. 5/6, 334 (1957).
6. Yu. I. Gryzin et al., Radiochemical Determination Methods for Plutonium, Americium, Curium, Californium, Berkelium, and Fission Products in Irradiated Materials [in Russian], NIIAR Preprint, Melekess (1970).
7. Analytical Chemistry of the Transplutonium Elements: Americium and Curium [in Russian], Nauka, Moscow (1970).
8. É. V. Ershova et al., USSR Paper No. 49/R/45 at the Fourth Geneva Conference (1971).
9. Z. V. Ershova et al., Inventor's Certificate No. 403330, Byull. Izobret., No. 28, 229 (1978).
10. N. E. Tsvetaeva et al., Inventor's Certificate No. 458603, Byull. Izobret., No. 28, 229 (1978).
11. N. E. Tsvetaeva, D. A. Fedoseev, and L. A. Ivanova, Inventor's Certificate No. 558549, Byull. Izobret., No. 9, 298 (1982).
12. N. E. Tsvetaeva et al., Radiokhimiya, 20, No. 1, 71 (1978).
13. N. E. Tsvetaeva et al., ibid., 21, No. 2, 252 (1979).
14. V. P. Kermanov and D. A. Fedoseev, Dosimetric and Radiometric Monitoring [in Russian], Vol. 1, Atomizdat, Moscow (1980), p. 245.
15. Recommendations on Methods for Health-Physics Monitoring for the Contents of Radioactive Substances in Environmental Objects [in Russian], Minzdrav SSSR, Moscow (1980).
16. N. E. Tsvetaeva, D. A. Fedoseev, and A. V. Rodionov, Abstracts for the Eleventh Mendeleev Congress on General and Applied Chemistry, Coll. No. 1 [in Russian], Nauka, Moscow (1975), p. 275.
17. N. E. Tsvetaeva et al., in: Abstracts for the Conference on the Analytical Chemistry of Radioactive Elements [in Russian], Nauka, Moscow (1977), p. 27.
18. N. E. Tsvetaeva et al., Inventor's Certificate No. 650360, Byull. Izobret., No. 47, 308 (1978).
19. I. M. Korenman, Zh. Organ. Khim., 25, 2399 (1955).
20. V. I. Shchebetkovskii and A. A. Bychkov, in: Abstracts for the First All-Union Conference on the Chemistry of Neptunium and Plutonium [in Russian], Nauka, Leningrad (1975), p. 47.
21. V. V. Gromov and V. N. Spitsyn, Artificial Radionuclides in the Sea [in Russian], Atomizdat, Moscow (1976).
22. Transuranium Nuclides in the Environment, International Atomic Energy Agency (1976).
23. E. Mathew, W. Matkar, and K. Pillai, J. Radioanal. Chem., 62, No. 1-2, 267 (1981).
24. M. A. Belokurova et al., At. Energ., 18, No. 3, 296 (1965).
25. M. I. Yakunin, ibid., 50, No. 5, 334 (1981).
26. Radiation-Safety Standards NRB-76 [in Russian], Atomizdat, Moscow (1978).

A METHOD OF CALCULATING MEMBRANE-ELEMENT CASCADES

FOR SEPARATING MULTICOMPONENT MIXTURES

E. B. Gruzdev, N. I. Laguntsov,   UDC 621.039.3
B. I. Nikolaev, A. P. Todosiev,
and G. A. Sulaberidze

There are problems in calculating a separating plant consisting of several series-connected countercurrent stages when the enrichment factor is large because it is necessary to incorporate very precisely the physical features of the separation method as far as possible, while it is also necessary to derive the optimum algorithm for calculating the component distributions along the cascade. Methods have been published based on the use of elements in which the separation is described by simple laws [1-3]. However, it is often impossible to establish such laws for the elements, particularly in separating gas mixtures. This makes it necessary to derive methods that can be used for an arbitrary form for the enrichment functions in the stages.

Here we propose a method enabling one to resolve the system of balance equations for the flows of the components at the inlet to each stage by direct techniques. This method provides better convergence than the stepwise method of [1, 2, 4] and often reduces the run time, although it requires a certain increase in the computer memory.

Consider a countercurrent stage consisting of M membrane stages. The flux $\theta_i G_i$ passing through the membrane in stage i is supplied to the input of the next stage i + 1, while the part not passing through $(1 - \theta_i)G_i$ is returned to the input of stage i − 1. We assume that the flows to the inputs of the stages G_i (i = 1, 2,..., M) are given, while the feed flow F with component concentrations c_j^F (j = 1, 2, ..., N) is supplied to the input of stage k. Also, one of the outgoing flows is specified (the flow W taken from the first stage is called the stripped fraction, while the flow P taken from stage M is the product).

The task of calculating a stage amounts to determining the separation factors θ_i, the distributions of the component concentrations in the flows at the input and output to each stage c_{ij}, c_{ij}^+, c_{ij}^- (i = 1, 2, ..., M; j = 1, 2, ..., N), and the membrane areas in the stages S_i (i = 1, 2, ..., M)

In the stationary state, the distribution of the component concentrations over the stages should satisfy the following system of equations [5]:

$$G_1 c_{1j} - (1 - \theta_2) G_2 c_{2j}^- - [W - (1 - \theta_1) G_1] c_j^W = 0;$$
$$j = 1, 2, \ldots, N;$$

$$G_i c_{ij} - \theta_{i-1} G_{i-1} c_{i-1,j}^+ - (1 - \theta_{i+1}) G_{i+1} c_{i+1,j}^- - \delta_{ik} F c_j^F = 0, \qquad (1)$$
$$i = 2, 3, \ldots, M-1,$$
$$j = 1, 2, \ldots, N;$$

$$G_M c_{Mj} - \theta_{M-1} G_{M-1} c_{M-1,j}^+ - [P - \theta_M G_M] c_j^P = 0, \quad j = 1, 2, \ldots, N,$$

where

$$\delta_{ik} = \begin{cases} 0, & i \neq k; \\ 1, & i = k; \end{cases} \qquad (2)$$
$$\begin{cases} c_{ij}^+ = f_i(c_{ij}, \theta_i, G_i); \\ c_{ij}^- = (c_{ij} - \theta_i c_{ij}^+)/(1 - \theta_i). \end{cases}$$

The detailed form of the function in (2) is determined by the separation method and the mode of operation. To close system (1) of N M equations, it is necessary to eliminate the θ_i (i = 1, 2, ..., M) from the unknowns. One specifies the value of one of these coefficients (for example, θ_1) and determines the other θ_i from standard relations [3]:

$$\theta_{i+1} = \begin{cases} 1 - \dfrac{W}{G_{i+1}} - \dfrac{\theta_i G_i}{G_{i+1}}, & i = 1, 2, \ldots, k-1; \\ 1 + \dfrac{P}{G_{i+1}} - \dfrac{\theta_i G_i}{G_{i+1}}, & i = k, k+1, \ldots, M-1. \end{cases} \tag{3}$$

A damped form of Newton's method [6] was used to solve (1), in which the iterative process was applied in the form

$$F'(\mathbf{x}^h) \Delta \mathbf{x}^h = -\omega F(\mathbf{x}^h), \tag{4}$$

where $F(\mathbf{x}^k)$ are the values of the left sides in (1) at a point with known coordinates $\mathbf{x}^k$; $F^1(\mathbf{x}^k)$ is the Jacobi matrix for the system at that point, $\Delta\mathbf{x}^k = \mathbf{x}^{k+1} - \mathbf{x}^k$, and ω is the damping coefficient. In this style, the determination of a new approximation $\mathbf{x}^{k+1}$ amounts to solving a system of equations linear in $\Delta\mathbf{x}^k$ of the form $A\Delta\mathbf{x} = \mathbf{b}$. To determine $\Delta\mathbf{x}$, we formulated a Gauss elimination algorithm involving compact storage of matrix A in the executive store. Compact storage of A is possible because the Jacobi matrix $F'(\mathbf{x})$ belongs to the type of strip matrices with strip width 2 (2M − 1) + 1, as is evident from (1), and during the iterations of (4) the strip structure of the matrix persists [7].

The algorithm was formulated in such a way that the elements of the Jacobian $F'(\mathbf{x})$ not appearing in the strip of this width did not participate in the calculations, which reduced the run time by a substantial factor. It is preferable to calculate the elements of the Jacobian analytically, since then the convergence rate in the iteration of (4) is quadratic. However, the form of the function for c_{ij}^+ in (2) does not always allow one to derive analytic expressions for the derivatives, so in this algorithm the elements of the Jacobian were determined numerically from a two-point scheme.

This method can be used to calculate stages when one specifies not the stage throughputs but an equivalent number of other parameters. In particular, interest attaches to calculating stages with given membrane areas. Then to system (1) we add M equations of the form

$$f_2(c_{ij}, \theta_i, G_i) - S_i = 0, \quad i = 1, 2, \ldots, M, \tag{5}$$

where S_i are the given membrane areas, while $f_2(c_{ij}, \theta_i, G_i)$ are the calculated ones.

In what follows we examine some results for a cascade with a given stage throughput distribution. The separation performance was examined by reference to the three-component mixture $CO_2 - O_2 - CO$ (0.85 $c_{CO_2}^F$, 0.05$c_{O_2}^F$, 0.1% c_{CO}^F. In each stage, the separating membrane consisted of poly-4-methylpent-1-ene. The specific permeabilities of this material are $Q_{CO_2} = 3.16 \cdot 10^{-14}$, $Q_{O_2} = 9.74 \cdot 10^{-15}$, $Q_{CO} = 2.75 \cdot 10^{-15}$ m•mole/(m^2•sec•Pa) [8], while the thickness was taken as $\lambda = 10$ μm and the pressures in the high-pressure and low-pressure cavities were taken as $p_1 = 7.65 \cdot 10^5$ Pa and $p_2 = 9.81 \cdot 10^4$ Pa, respectively.

One of the basic parameters characterizing the separation is the ratio of the product flow P to the waste or stripped flow W. We examined the effects of P/W on the mixture composition in the flows emerging from the stages, for example, in the waste flow (Fig. 1). We used the conservation equations for the cascade as a whole:

$$\begin{cases} Fc_j^F = Pc_j^P + Wc_j^W, & j = 1, 2, \ldots, N-1; \\ F = P + W, \end{cases} \tag{6}$$

to show that for P/W → 0 the concentrations of the components in the waste c_j^W (j = 1, 2, ...,N) will approximate to the values c_j^F (j = 1, 2, ..., N). As P increases, the concentration of the readily penetrating component RPC decreases, while that of the slowly penetrating component SPC increases, and that of the intermediate one passes through a maximum. It is clear that one may obtain either one or several components in the waste for different values of P/W. A similar behavior occurs in c_j^P(P/W), but with the difference that the product flow is enriched in the RPC as P/W decreases.
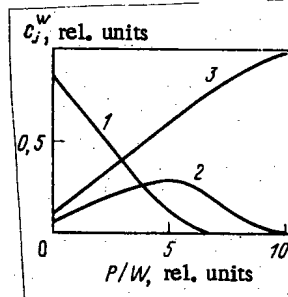
Fig. 1. Dependence of the component concentrations in the stripped flow on P/W for $M = 7$, $k = 4$, $G_i/F = 10$ ($i = 2, 3, \ldots, M-1$), $\theta_2 = 0.5$; 1) CO_2; 2) O_2; 3) CO.
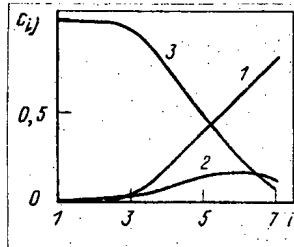
Fig. 2
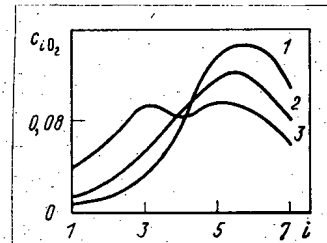
Fig. 3

Fig. 2. Distributions of component concentrations at the inputs to the stages along the cascade for $k = 4$, $G_i/F = 10$ ($i = 2, 3, \ldots, M-1$), $P/W = 10$, $\theta_2 = 0.5$; 1) CO_2; 2) O_2; 3) CO.

Fig. 3. Distribution of the intermediate-component concentrations along the cascade for $k = 4$, $P/W = 10$: 1) $G_i/F = 10$ ($i = 2, 3, \ldots, M-1$); 2) $G_i/F = 3$; 3) $G_i/F = 2$.
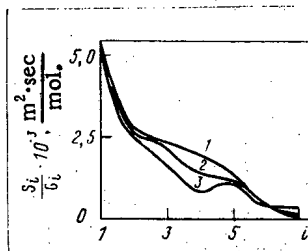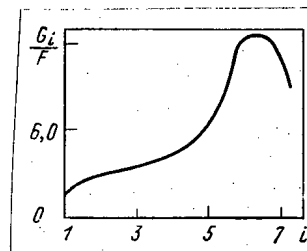
Fig. 4

Fig. 5

Fig. 4. Distribution of the membrane areas in the stages along the cascade for $k = 4$, $P/W = 10$: 1) $G_i/F = 10$ ($i = 2, 3, \ldots, M-1$); 2) $G_i/F = 5$; 3) $G_i/F = 3$.

Fig. 5. Distribution of the gas-mixture flows at the inputs to the stages for a given membrane area for $k = 4$, $P/W = 10$, $S_i/F = 8 \cdot 10^3$ $m^2 \cdot sec/mole$ ($i = 2, 3, \ldots, M-1$).

We now consider relations enabling one to estimate the value of P/W at which the limiting concentration of component s may be obtained in P or W. We have from (6) that

$$\frac{P}{W} = \frac{c_s^F - c_s^W}{c_s^P - c_s^F} . \tag{7}$$

We assume that the mixture is divided into two fractions in the cascade: The product flow accumulates only the components 1, 2, ..., s, ..., j, while the waste flow accumulates only j + 1, j + 2, ..., N. Then (7) can be written as

$$\frac{P}{W} = \frac{c_s^F}{c_{s\,lim}^P - c_s^F} . \tag{8}$$

We sum the first j equations in (6) to get

555

$$P = F \sum_{l=1}^{j} c_l^F, \tag{9}$$

after which we use the conservation equation for component s to write an equation for the limiting concentration in the product:

$$c_s^P \lim = \frac{c_s^F}{\sum_{l=1}^{j} c_l^F}. \tag{10}$$

If component s accumulates in the waste, then (8) and (10) become

$$\frac{P}{W} = \frac{c_s^F - c_s^W \lim}{c_s^F}; \tag{11}$$

$$c_s^W \lim = \frac{c_s^F}{\sum_{l=j+1}^{N} c_l^F}. \tag{12}$$

Formulas analogous to (8) and (10) have been derived in [9] for an infinitely long cascade separating isotope mixtures. The calculations indicate that (8) and (10) enable one to estimate the limiting concentrations in the two flows and the corresponding P/W in the cascade for any degree of enrichment in a stage of short length. In particular, in calculating a cascade consisting of five stages for separating a seven-component hydrocarbon mixture, there was not more than 7% relative difference between the calculated concentration for an arbitrary intermediate component and the value given by (10).

Figure 2 shows the concentration distribution at the inputs along the cascade. In the direction from the waste point to the product point, the mixture becomes richer in the RPC, while in the opposite direction it becomes richer in the SPC, while the concentration of an intermediate component passes through a maximum. This maximum is due to the component being displaced from the first and latter stages by the SPC and RPC correspondingly on account of their higher activity. The position of the maximum is determined in the main by P/W. The position is also affected by the feed flow (Fig. 3); as the latter increases, the concentration gradients in the cascade decrease, which reduces the maximum concentration in the intermediate component and displaces the maximum towards the point of feed input. An interesting point is that there is a second maximum in the concentration of the intermediate component for a certain relation between the parameters of the cascade and those of the input mixture.

We now consider the distribution of the membrane areas along the length of the cascade with given flows between stages (Fig. 4). The mixture becomes enriched in the SPC in the direction from the product flow to the waste one, while the mixture flow rates are the same at the inputs to each of the stages, so the membrane areas increase in that direction. As the feed flow increases, the distribution of the areas alters, and above a certain F one finds a local maximum, because the proportion of nonpenetrating flow decreases as F increases, while the area of the membrane in stage k + 1 increases.

If the membrane areas are included in the given quantities and these are identical in all stages, the flow of mixture to the inlet to a stage increases in the direction from the waste to the product (Fig. 5). The form of the relationship is due to the increase in the RPC concentration as the product point is approached, while the reduction in flow at the inlet to the last stage occurs because the input to stage M is only the flux passing through the membrane in stage M − 1.

The results in Figs. 4 and 5 indicate that it is impossible to design a countercurrent cascade with identical membrane areas and identical input flows to all stages simultaneously.

In conclusion we note that these results apply to the case where the separating characteristics of a membrane stage may be calculated from a model for a complete-mixing element [10]. The method also enables one to calculate a stage from any of the standard element models. In particular, we have performed calculations on a cascade with given flows between stages subject to the condition that a stage works as an element with transverse efflux [10].

Although there are only comparatively small differences in separation characteristics of elements with transverse efflux and those with complete mixing, a cascade of stages of the first type gives an advantage as regards the overall membrane area of about 20%.

LITERATURE CITED

1. N. I. Nikolaev et al., Theoretical Principles of Chemical Engineering [in Russian], Vol. 13, No. 4 (1979), p. 486.
2. I. S. Knyazev, N. I. Laguntsov, and G. A. Sulaberidze, ibid., Vol. 15, No. 1 (1981), p. 36.
3. N. A. Kolokol'tsov and N. I. Laguntsov, At. Energ., 27, No. 6, 560 (1969).
4. V. D. Borisevich et al., Theoretical Principles of Chemical Engineering [in Russian], Vol. 17, No. 2 (1983), p. 172.
5. N. A. Kolokol'tsov and N. I. Laguntsov, At. Energ., 29, No. 4, 300 (1970).
6. J. M. Ortega and W. C. Reinboldt, Iterative Solution of Nonlinear Equations in Several Variables, Academic Press (1970).
7. G. E. Forsythe and C. Moler, Computer Solution of Linear Algebraic Systems, Prentice-Hall (1967).
8. N. I. Nikolaev, Diffusion in Membranes [in Russian], Khimiya, Moscow (1980).
9. V. P. Minenko, At. Energ., 33, No. 2, 703 (1972).
10. V. D. Borisevich et al., Theoretical Principles of Chemical Engineering [in Russian], Vol. 17, No. 1 (1983), p. 60.

LETTERS

DENSITY OF MELTS OF THE TERNARY MUTUAL SYSTEM K, KR//F, Cl

S. E. Darienko, N. N. Kurbatov,
S. P. Raspopin, and Yu. F. Chervinskii

Fluoride—chloride zirconium-containing melts can be used in an electrolytic process to obtain zirconium metal [1]; in view of this it is necessary to have data about the physicochemical properties of the possible melts [2-4]. In this paper we present the results of studies on the temperature dependences of the density of melts of the system K, Zr//F, Cl over a wide range of concentration. The measurements were carried out by the method of maximum pressure in a gas bubble in fiber-glass-reinforced carbon crucibles. Purified argon served as the working gas. In calculating the density we took into account a correction for the displacement of melt by the platinum capillary. The error in the determination of the density did not exceed 1%.

The reliability of the experimental results in many ways depends on the purity of the salts used and, therefore, particular attention was paid to obtaining and storing pure anhydrous salts. In order to obtain potassium fluoride we used chemically pure $KF \cdot 2H_2O$, which was dried using the familiar method [5], and then melted under continuous evacuation. The resulting product was subjected to zone recrystallization. Special-purity potassium chloride was remelted in advance. To obtain zirconium tetrafluoride we took pure-grade salt, which was then dried at a residual pressure of 1.33 Pa, after which it was vacuum-distilled. The physicochemical properties of the substances obtained are in satisfactory agreement with the reference-book data [6].

The density of molten mixtures of the ternary mutual system K, Zr//F, Cl was studied by the method of polythermal sections, the sections being drawn through the apex of the concentration triangle corresponding to zirconium tetrafluoride. The experimental data were processed by the method of least squares. For all the melts in the temperature range investigated we obtained empirical temperature dependences of the density in the form of equations $\rho = a - b \cdot T$, whose coefficients are presented in Table 1. The rms deviations (S) of the experimental values of the density from the values calculated from the equation are also given in Table 1.

Figure 1 shows the lines of equal density in the system K, Zr//F, Cl, calculated for 1150°K. With increasing zirconium tetrafluoride content in the mixtures, the density of the
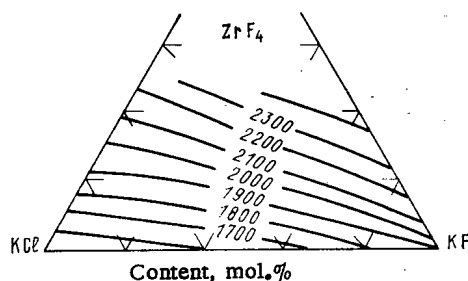

Fig. 1. Lines of equal density (kg/m^3) of melts of K, Zr//F, Cl at 1150°K.

TABLE 1. Density of Melts of the System K, Zr//F, Cl

Content of components, mole %			$\rho = a - b \cdot T$, kg/m^3		s	Temperature interval, °K
ZrF$_4$	KCl	KF	a	b		
0	0	100	2661,5	0,6625	1,6	1135—1222
0	20	80	2535,4	0,6774	2,1	1061—1153
0	40	60	2380,4	0,6188	1,3	962—1158
0	60	40	2317,3	0,6352	2,8	975—1141
0	80	20	2246,9	0,6340	1,8	1009—1139
0	100	0	2181,8	0,6242	1,4	1058—1144
10	90	0	2515,4	0,7272	2,7	1018—1158
20	80	0	2612,2	0,6561	6,0	964—1191
30	70	0	2838,2	0,7442	4,7	926—1148
40	60	0	2968,2	0,7356	2,8	861—1145
50	50	0	3098,9	0,7535	2,0	972—1143
10	72	18	2439,7	0,6267	2,7	983—1151
20	64	16	2614,8	0,6503	2,1	954—1158
30	56	14	2879,2	0,7462	2,4	943—1151
40	48	12	2970,2	0,6927	2,5	974—1157
50	40	10	2907,4	0,5187	1,6	973—1153
10	54	36	2659,5	0,7909	2,9	1008—1158
20	48	32	2532,6	0,5328	4,0	981—1180
30	42	28	2928,1	0,7371	3,3	975—1152
40	36	24	3110,6	0,7738	1,8	974—1161
50	30	20	3214,0	0,7496	1,0	977—1151
10	36	54	2649,6	0,6739	2,7	1021—1170
20	32	48	2832,0	0,7153	2,5	1066—1181
30	28	42	3009,2	0,7072	1,4	1046—1167
40	24	36	3104,0	0,6771	6,2	1032—1150
50	20	30	3251,6	0,6846	2,6	998—1181
10	18	72	2779,5	0,6908	1,7	1038—1183
20	16	64	3208,2	0,9542	1,4	1093—1174
30	14	56	3477,8	1,0587	6,5	1081—1159
40	12	48	3114,9	0,6525	4,5	873—1156
50	10	40	3309,4	0,7313	2,2	1048—1171
5	0	95	2687,0	0,5662	1,4	1118—1189
13	0	87	3093,7	0,7941	2,7	1060—1181
20	0	80	3444,8	1,0162	1,1	1158—1230
33	0	67	3064,4	0,6082	4,2	1066—1171
40	0	60	3140,6	0,6021	5,7	872—1151
45	0	55	3332,7	0,7102	3,2	953—1150
50	0	50	3528,2	0,8292	2,7	949—1173

melts increases. The use of zirconium tetrafluoride substantially widens the range of compositions of the electrolyte, which in principle cannot be attained in the system KF—KCl—K$_2$ZrF$_6$ [3].

LITERATURE CITED

1. I. N. Sheiko, Ukr. Khim. Zh., 29, No. 1, 57 (1963).
2. I. N. Sheiko, R. V. Chernov, and V. I. Suprunchuk, Ukr. Khim. Zh., 31, No. 11, 1143 (1965).
3. I. N. Sheiko, T. A. Bandur, and T. N. Grechina, Ukr. Khim. Zh., 40, No. 11, 1210 (1974).
4. I. N. Sheiko, T. N. Grechina, and I. A. Sidorenko, Ukr. Khim. Zh., 41, No. 2, 206 (1975).
5. Yu. V. Karyakin and I. I. Angelov, Pure Chemical Substances [in Russian], Khimiya, Moscow (1974), p. 142.
6. Handbook of Fused Salts [in Russian], Vol. 1, Khimiya, Leningrad (1971).

HEAT EXCHANGE DURING THE FLOW OF A MELT OF LiF—NaF—KF
FLUORIDE SALTS IN A CIRCULAR TUBE

V. V. Ignat'ev, S. V. Keronovskii,   UDC 621.039
A. I. Surenkov, O. P. Shcherbanyuk,
S. P. Manchkha, and Yu. B. Smirnov

The solution of a number of nuclear power problems, such as the generation and transfer of high-potential heat (temperature $\geq 600°C$), production of fissile materials in the blankets of fusion reactors and power breeder reactors, as well as some others, can be attained by using melts of fluoride salts (MFS) [1-3].

The problems of heat exchange in MFS have not been investigated to any extent. Very limited experimental data have been published [4] about heat transfer from MFS in tubes and they are not sufficient to give an idea of the general laws governing the heat transfer and the influence of diverse factors on it (change in the physicochemical properties of the coolant under the action of impurities, temperature, and radiation; corrosion of the heat-exchange surface; contact thermal resistance of the layer of impurities and the formation of deposits on the heat-exchange surface). In particular, in studies of the heat transfer of MFS (LiF—BeF_2—ThF_4—UF_4) in a heated circular tube it was found [4] that the experimental points are, on the average, 25-30% below the curve plotted according to the Sieder—Tate formula [5], both in the transient flow region and in the region of developed turbulent flow. In the opinion of Hoffman et al. [4] this discrepancy cannot be explained by the influence of thermogravitational forces and is most likely due to the error of the measurements of the MFS temperature at the inlet and outlet of the experimental section (ES). Unfortunately, the data presented do not permit a very detailed analysis to be made of them.

In the work reported here we studied the heat transfer of MFS and how it is affected by the physicochemical processes of the interaction of the MFS with the structural materials under conditions characteristic of heat exchangers of atomic power plants.

The investigations were carried out on a stand constituting a closed loop with forced coolant circulation [6]. As the coolant we used a MFS with the composition (in mole%) 46.5 LiF, 11.5 NaF, 42 KF (melting point 454°C), containing the main components of the compositions of the fuel and intermediate loops of an atomic power plant with the MFS. All the parts of the loop were made of Kh18N10T stainless steel, which is compatible with MFS not containing the fuel impurities U, Th, and Pu [7]. The experimental section consisted of a circular vertical tube (inner diameter d = 30 mm, unheated part 20d, and heated part 40d), through which coolant was pumped from the bottom up. Heating was by means of a 10 × 0.5-mm strip resistance heater, evenly wound onto the surface of the tube.

In the experiments we measured the power delivered to the experimental section, the temperature of its wall (at 12 cross sections of the heating zone), and the mean-mass temperature at the inlet and outlet of the experimental section. The coolant flow rate in the loop was determined with the aid of a calorimetric flow meter which at the same time acts as a "salt—air" heat exchanger. Chromel—Alumel thermocouples were used to measure the temperature. The density of the heat flux through the wall of the experimental section was calculated from the delivered electrical power with allowance for the thermal losses into the surroundings. The temperature drop in the experimental section and the calorimeter flow meter was determined with the aid of multi-junction differential thermocouples. Before beginning the experiments with MFS we measured the heat transfer during the flow of distilled water. These results are in satisfactory agreement with the tried and tested generalizing relations of [5, 8]. Before the experiments the MFS were subjected to purification [6]. The experiments with the MFS were carried out with excess argon pressure above the surface of the coolant.
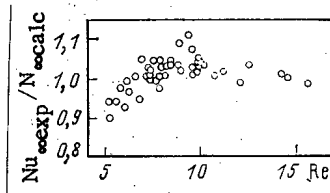
Fig. 1. Comparison of experimental data on heat transfer to LiF—NaF—KF ($Nu_{\infty exp}$) with data calculated from formula of [11] ($Nu_{\infty calc}$).

The heat transfer during forced flow of MFS was studied in the range of Re numbers $5 \cdot 10^3$ – $15 \cdot 10^3$ and Pr numbers 1.7–2.3. The mean—mass coolant temperature at the inlet to the experimental section was 550–650°C. The density of the heat flux at the wall varied from $3 \cdot 10^4$ to $6 \cdot 10^4$ W/m². The discrepancy in the heat balance in the experiments did not exceed 10%. In processing the experimental results and in carrying out the calculations, as in [4] we used data about the properties of MFS, obtained in [8]. More recent data about the properties of MFS are in agreement with those given in [8]. Analysis of the results of the measurements of local heat-transfer coefficients showed that thermal stabilization occurs at $x/d \geq 10$–15. Unlike the experimental data of [4], our data are in agreement with those calculated from the formula of [5], which generalized the results of measurements of heat transfer to liquids with different Pr numbers over a wide range of Re numbers, including the entire transitional region from laminar to turbulent flow. Estimates made by the method of [9] showed that the effect of thermogravitational forces on heat exchange under the conditions of our experiments can be neglected. The data obtained are in fairly good agreement, in the range $Re \geq 9 \cdot 10^3$, with the data calculated from the empirical equation of [10], while in the range of Re values up to $5 \cdot 10^3$ they are in agreement with the data of [11] (see Fig. 1) in which the formula of [9] was modified as it applies to the transitional region for $Re \leq 10^4$ and $Pr \geq 2$:

$$Nu_\infty = Nu_\infty^* (1 - 1000/Re),$$

where Nu_∞^* is found from the Petukhov—Kirillov formula [10] for $k_1 = 1.0$ and $k_2 = 12.7$.

In one experiment we studied the accumulation of impurities in MFS and the effectiveness of purification to remove them with the aid of a dead—end cold trap [12]. It is known that the corrosive interaction of chromium—nickel steels with MFS, which do not contain fuel impurities, is determined mainly by the passage of chromium, and to a lesser degree iron and nickel, into the melt in the form of oxides and fluorides through oxidation—reduction reactions with the impurities present in the metal [7]. At the same time, in order to study how the heat exchange is affected by the interaction of the MFS with the structural materials, we measured the heat transfer when the coolant at the inlet into the experimental section was at a constant temperature of 600°C.

The length of the experiments was chosen on the basis of the fact that under static isothermal conditions saturation in the corrosion processes occurs in less than 200 h [7]. This takes place much more quickly, obviously, under dynamic conditions. The results of analysis of MFS samples taken during the experiment indicate that after 100 h of operation the equilibrium concentration of the principal metallic impurities did not exceed 10^{-2} mass %. This concentration of corrosion products does not affect the properties of the MFS. Purification of the MFS by means of a cold trap made it possible for several hours to reduce the chromium, nickel, and iron content by a factor of 2–5, which attests to the effectiveness of this method. When the purification was halted, we observed a rapid increase in the chromium content in the coolant to the initial temperature while the iron and nickel content practically did not change. During visual analysis of the contents of the cold trap it was discovered that the impurities concentrate in the cooled zone as a crystalline deposit, containing practically no coolant. According to the data of chemical analysis this deposit consists of a considerable amount of corrosion products of the structural material of the stand. As shown by estimates, there is a balance between the impurities removed from the circulation loop during purification and the impurities found in the cold trap. After the experiments no deposits were detected on the inner surface of the tube of the experimental section. The melting point of the MFS investigated did not change, i.e., it was indirectly confirmed that the physical properties did not change during the operation.

Analysis of the results of the experiments indicated that the heat-transfer coefficients of LiF—NaF—KF remain constant during operation (>1000 h), indicating that no factors have any appreciable effect on the heat exchange under the conditions of heating.

In conclusion, we should point out that the detected mass transfer of corrosion products onto the cold surfaces can apparently have an effect on the state of the heat-exchange surface under the conditions of cooling, but the quantitative side of the effect and its influence on heat transfer require further investigations.

The authors express their thanks to L. A. Sukomel, S. A. Konakov, É. N. Neretin, and A. Kh. Fazlullin for participating in the preparation and conduct of the experiments as well as assistance in the formulation of the problem and discussion of the results.

LITERATURE CITED

1. V. M. Novikov, At. Tekh. Rubezhom, No. 1, 3 (1983).
2. V. M. Novikov and V. V. Ignat'ev, Magn. Gidrodin., No. 4, 119 (1980).
3. K. Furukawa et al., J. Nucl. Sci. Technol., 18, 79 (1981).
4. H. Hoffman, J. Keyes, and J. Cooke, MSR-Program. Sem. Rept., ORNL-4543, 87 (1970).
5. E. Sieder and C. Tate, Indust. Eng. Chem., 28, 1429 (1936).
6. S. S. Abalin et al., Vopr. At. Nauki Tekh. Ser. Atomno-Vodorodnaya Energ. Tekhnol., No. 3(10), 112 (1981).
7. V. B. Kirillov and V. N. Fedulov, Fiz.-Khim. Mekh. Mater., No. 6, 22 (1980).
8. W. Powers, S. Cohen, and N. Greene, Nucl. Sci. Eng., 71, 200 (1963).
9. A. F. Polyakov, Teplofiz. Vys. Temp., No. 1, 106 (1973).
10. B. S. Petukhov and V. V. Kirillov, Teploenergetika, No. 4, 63 (1958).
11. V. Gnielinski, Forschung Ingenieurwesen, 41, 1 (1975).
12. V. I. Subbotin, M. N. Ivanovskii, and M. N. Arnol'dov, Physicochemical Fundamentals of the Use of Liquid-Metal Coolants [in Russian], Atomizdat, Moscow (1970).

EFFECT OF REACTOR IRRADIATION ON THE MICROSTRUCTURE OF

PYROCARBON COATINGS

I. S. Alekseeva, A. A. Babad—Zakhryapin,
Yu. G. Degal'tsev, L. A. Elesin,
Yu. M. Utkin, and Yu. N. Yurovskikh

UDC 621.039.544.53

The great attention to investigations of the microstructure of pyrocarbon coatings in microfuel elements is due to the necessity of retaining fission products for a high fuel burnup and a high neutron irradiation fluence. Meanwhile, changes of structure by the action of radiation and the buildup of fission products can significantly affect the properties of the pyrocarbon coating, and lead to the onset of noncontinuity or through channels. Prereactor investigations of the state of the applied pyrocarbon coatings, carried out by etching thin sections in the positive column of an interelectrode glow discharge, which was excited in an air medium at a pressure of 130 Pa, arcing potential 6000 V, and a discharge current of 20 mA, showed the quite high quality of these coatings [1]. It will be interesting to investigate the change of structure of pyrocarbon coatings after irradiation of micro-fuel elements in the MR reactor (channel type "Karat").

The exposure of the microstructure of irradiated pyrocarbon coatings (Table 1) was carried out by the procedure developed in [1]. Irradiated and nonirradiated micro-fuel elements were placed in the yoke for preparing the thin sections, for the purpose of ensuring identical etching conditions. After preparation of the thin sections of irradiated micro-fuel elements, the fuel cores were removed and in batches 65D and 21-Kh the pyrocarbon coverings, located below the SiC cladding, were broken down.

During etching of the pyrocarbon coatings in the positive column of the glow discharge, the component with the least perfect lattice is the most intensely oxidized. As a result, a

contour develops on the surface, the troughs of which correspond to the position of this component. The relative content of the easily oxidized component can be established by means of a "Kvantimet-720" analyzer from the contrast of the photographic image of the surface of the thin section. The optical anisotropy coefficient of the pyrocarbon coating was measured by the well-known procedure of [2]. The structure of the pyrocarbon coatings was studied on a "Temskan-100" scanning microscope after preliminary sputtering of a film of gold with a thickness of 10 nm.

A reticular microstructure of the outer pyrocarbon coating with a striated arrangement along the front of development of the coating, of the readily oxidized component (dark lines in Fig. 1) is characteristic for the unirradiated batches 16D, 65D, and 5-76, but the coatings of batch 21-Kh had an onion-like structure with alternation of concentric layers of ordered and disordered components (Fig. 2); at the same time, the outer layer with a thickness of 15 μm of the damaged pyrocarbon coating with a uniform arrangement of both components (zone a) differed in structure from the underlying layer (zone b). The optical anisotropy coefficient of the pyrocarbon coating for batch 21-Kh was found to be higher than for batches 16D, 65D, and 5-76.

The irradiation conditions of the batches of micro-fuel elements investigated are given in Table 2 and the measurement procedure in the "Karat" channel and the burnup calculations were described earlier in [3].

TABLE 1. Some Properties of Unirradiated Pyrocarbon Coatings*

Batch	Coating No.[†]	Density, g/cm^3	Thickness, μm	Optical antisotropy coefficient	Fraction of readily oxidized component in the outer coating, %
16D	1	1,1	35	—	—
	2	1,86	60	1,18	15
	3	1,8	65	1,16	15
65D	1	1,1	30	—	—
	2	1,5	15	—	—
	3	1,9	30	1,10	—
	4	1,9	50	1,13	20
5-76	1	1,2	55	—	—
	2	1,8	50	1,10	10
	3	1,8	45	1,10	8
21-Kh	1	1,1	30	1,20	—
	2	—	15	1,34	4
	3	1,62	28	1,38	6
	4	1,75	85	1,50	10

*All batches of the micro-fuel elements had a SiC cladding, the radiation resistance of which was not studied in the present work.
[†]The multilayer pyrocarbon coating consists of a buffer (1), inner dense (2, 3), and outer layers (4). In batches 16D and 5-76 coating 3 is outside.

TABLE 2. Irradiation Conditions of Batches of Micro-Fuel Elements

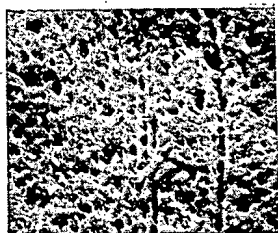| Batch	Burnup, %	Neutron fluence, $10^{21} cm^{-2}$ (0.18 MeV)	Maximum radiation temperature °K	Fraction of readily oxidized component in outer coating after irradiation, %
16D	6,1	1,4	1370	6
65D	6,7	1,7	1540	8
5-76	10,5	1,4	1370	3
21-Kh	5,9	1,5	1520	4

Fig. 1   Fig. 2
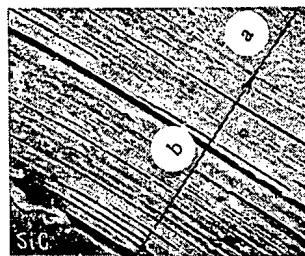
Fig. 1. Microstructure of unirradiated outer pyrocarbon coat-
ing for batch 16D (×2000).

Fig. 2. Microstructure of outer (a) and inner (b) layers of un-
irradiated peripheral pyrocarbon coating for batch 21-Kh (×2000).

Fig. 3   Fig. 4
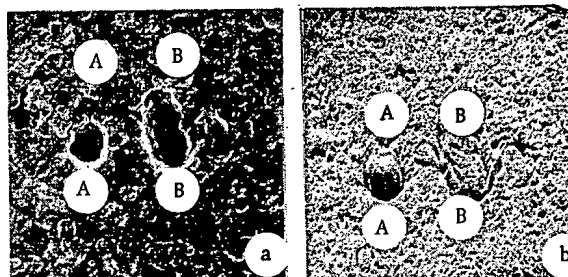
Fig. 3. Microstructure of irradiated outer pyrocarbon coating for batch 16D (×4000).

Fig. 4. Microstructure (a) and contouring (b), obtained by the Y-modulation method,
of irradiated pyrocarbon coating for batch 65D: A) pore; B)inclusion of readily ox-
idized component (×5000).
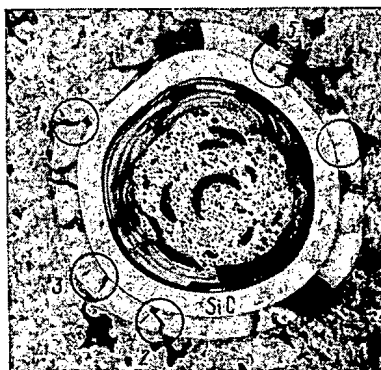
Fig. 5. Structure of irradiated
micro-fuel element of batch 21-Kh
(×100).

Reactor irradiation leads to marked changes in the structure of the pyrocarbon coating.
The coatings in batches 16D, 65D, and 5-76 were more uniform; at the same time, the fraction
of readily oxidized component was reduced approximately twofold (see Table 2). Crushing of
the structure of the coatings is observed (Fig. 3) and, what is very important, the formation
of circular pores with a diameter of 1-2.5 μm (Figs. 3 and 4). The use of the Y-modulation
method allowed the fraction of pores and readily oxidized component to be determined distinct-
ly (Fig. 4b) during analysis of the image.

The pyrocarbon coating for the irradiated batch 21-Kh was attacked; at the same time,
the coating below the SiC layer was destroyed completely and the outer coating was split.
Cracks are also observed spreading from the SiC coating, while in the central regions of the
coating (Fig. 5), the cracks change their direction of spread (Nos. 1 and 2) or are terminated

564

(Nos. 3 and 4), and some cracks are transformed into circular cracks (No. 5), which confirms the greater radiation resistance of zone "a" by comparison with zone "b" (see Fig. 2).

According to the data obtained, the pyrocarbon coatings on batches 16D, 65D and 5-76 after irradiation at 1540°K, up to a neutron fluence of $1.5 \cdot 10^{21}$ cm^{-2} neutrons retain their completeness, despite marked changes of structure, while the pyrocarbon coatings for batch 21-Kh are found to be completely destroyed. In the original state (before irradiation), these batches differed in the nature of the distribution of the readily oxidized component and in the value of the optical coefficient. Hence, it follows that the uniform distribution of the readily oxidized component and the low optical anisotropy coefficient (~1.1) are criteria of the radiation resistance of pyrocarbon coatings.

The development of pores in the coatings with a quite uniform distribution of the readily oxidized component can be related with the radiation deposition of material as a result of ordering of the crystal structure of this component, with the simultaneous increase of the sizes of the ordered component crystallites [4].

With higher values of the neutron fluence, radiation growth of the coatings can be expected, in consequence of the increase of anisotropy of the material [5]. This, inevitably, is accompanied by an increase of internal stresses, which leads to the formation of cracks, as is observed in pyrocarbon coatings of batch 21-Kh, and characterized by a high initial anisotropy.

LITERATURE CITED

1. I. S. Alekseeva et al., At. Energ., 52, No. 4, 266 (1982).
2. K. Koizlik, Ber. Kernforschungsanlage, Jül-868, 71 (1972).
3. Yu. G. Degal'tsev et al., Problems of Nuclear Science and Technology. Series Atomic-hydrogen Power Generation [in Russian], No. 2(12) (1982), p. 14.
4. J. Bokros, J. Guthrie, and A. Schwartz, Carbon, 6, 55 (1968).
5. P. A. Platonov et al., At. Energ., 46, No. 4, 248 (1979).

HIGH-SPEED BULK ANALYSIS OF URANIUM IN GEOLOGICAL SAMPLES
BY THE DELAYED NEUTRON METHOD

V. R. Burmistrov

UDC 543.52

In the VVR-K reactor of the Institute of Nuclear Physics, Academy of Sciences of the Kazakh SSR, an automatic facility is being operated for the high-speed bulk determination of uranium in rocks [1, 2], which functions by the delayed neutron method [3] and is intended for bulk analyses when conducting extensive geochemical investigations for the purpose of revealing the regularity of a regional layout. Samples of rock, with a mass of up to 10 g, are irradiated in a special vertical channel at a distance of 30 mm from the surface of the reactor core and at a height of 110 mm from the central plane of the zone. The thermal neutron flux amounts to $1.4 \cdot 10^{13}$ cm$^{-2} \cdot$sec^{-1}, and the fast neutron flux with energy in excess of 2.4 MeV is $1.5 \cdot 10^{12}$ cm$^{-2} \cdot$sec^{-1}. The cadmium ratio with respect to the activity of gold is 2.54. The nonuniformity of the thermal neutron flux over the height of the hollow irradiation capsule does not exceed ±3% deviation from the mean. The instability of the flux with time is also found within the limits of 3%.

The delayed neutrons from the sample are recorded with 20 counters of an SNM-11, arranged in a polyethylene block (40 × 40 cm): 16 around a circle with radius 7 cm and 4 at a distance of 9 cm. The background of the facility with the nonoperating reactor is 10 pulses/min, and when operating at full power (10 MW) it is 27 pulses/min; for this, the background of a "blank experiment" is from 80-120 pulses/min, depending on the degree of contamination of the rabbit system and the discrimination level of the counters.

TABLE 1. Results of Two Parallel Uranium Determinations

Uranium content, 10^{-4} %		Number of samples	Relative rms deviation, %	
interval	average		present paper	data of [4]
0,1—0,49	0,33	21	5,5	—
0,5—1,99	1,3	36	4,0	30
2—4,9	3,5	140	2,5	20
5—9,9	7,1	79	1,8	16
10—19,9	12,5	19	1,4	12
20—49,9	28,8	8	1,3	9

The time of irradiation (and measurement) is 60 sec and the cooling time is 20 sec. The next sample is measured simultaneously with irradiation of the following sample. The sample is conveyed to the irradiation zone, withdrawn from it, and transferred to the recording block with compressed air. Irradiation, cooling, measurement, and printout of the results of the count are performed automatically with a maximum output of 45 samples per hour.

During the experimental operation of the facility, the output amounted on average to 50 tests per shift. The analytical parameters achieved are described in the Instructions [4], developed by E. G. Vertman et al. After further constructional developments, the output was increased to 200 tests per shift. After further development of the analyses procedure, the improved analytical parameters presented in this present report were obtained. More than 20,000 sample analyses were performed in all over three years of operation of the facility. The rock samples (crushed to 150 mesh), with a standard mass of 5 g, are hermetically packed in rubber fingers which are placed in polyethylene capsules serving for transportation.

As a comparison sample, a sample of a silicate composition is used, prepared on the basis of a standard UR-47 sample by dilution with quartz powder to a concentration of $1 \cdot 10^{-2}$ %. The comparison sample was calibrated against reference samples SG-1A, UR-47, UR-240, USFRS-73.5, S-8, and S-13. The mass of the weighed comparison sample was 5 g.

When carrying out the analyses, certain corrections are taken into account. The correction for lost counts of the recording system, for nominal reactor power, and with a uranium concentration of 10^{-2} % does not exceed 1%. A correction for the fission of thorium present in the samples, together with the uranium, is not required, as in our irradiation conditions the degree of activation of the uranium (with respect to delayed neutrons) exceeds the degree of activation of the thorium by a factor of 100, and in normal rocks the concentration of thorium and uranium is of one order.

A correction for self-screening of the activating neutron flux by the uranium is introduced from the experimentally determined value: 1 mg of uranium in the rock screens the flux by 0.23%. Corrections for screening of the activating neutron flux by strong absorbers present in the rock were found experimentally using as an example gadolinium, the most dangerous from this point of view: 1 mg of gadolinium in the rock screens the neutron flux by 8%. Thus, corrections for the presence of gadolinium become appreciable when its concentration in rocks is in excess of $3 \cdot 10^{-3}$%. Monitoring of the gadolinium content is based on the mineralogical composition of the samples. The gadolinium is determined on selective individual samples of each batch of tests by the method of neutron activation analysis. The last two corrections cannot be based on published data, as they are strongly dependent on the spectral composition of the reactor neutron flux.

We investigated the question of the effect of the composition of the matrix of geological samples on the results of the uranium determination for moderated and scattered neutrons. It was found experimentally that for silicate, limestone, and carboniferous rocks, the variation of the activating neutron flux in samples with mass 5 g did not exceed 1%.

The following analytical parameters were obtained for the facility: sensitivity 320 pulses/min per 1 µg uranium, limit of detection of uranium 0.1 µg ($2 \cdot 10^{-6}$% for 5-g samples), interval of concentration determined from $7 \cdot 10^{-6}$ to 3%. The reproducibility of the analysis results is given in Table 1. The reproducibility obtained by the authors of procedure [4] on our facility are given in the same table.

The results were verified by an analysis of standard samples as well as by a comparison with an analysis of the same samples by other analytical methods. On an average, the deviation with respect to the standard samples amounts to 3%. Statistical treatment [5] of the results of analysis of the samples by different methods shows an insignificant deviation for uranium concentrations greater than $3 \cdot 10^{-4}$%. The method of the present paper, as well as other published procedures, for example [4], gives a deviation from the results of a determination by the luminescence method, the latter giving lower results. The x-ray spectral method overestimates the results, if no correction is introduced for interfering elements (strontium, molybdenum, and rubidium). A verification of validity by an interlaboratory standardization of the Ministry of Geology of the USSR on 10 samples of different composition gives a deviation of results within limits of 4%. The procedure of the present paper has been introduced into practice. With a throughput of 10,000 analyses per year, the economic effect amounts to about 300,000 rubles.

LITERATURE CITED

1. V. V. Bolotov et al., Izv. Akad. Nauk KazakSSR, Ser. Fiz. Mat., No. 4, 95 (1980).
2. E. G. Vertman et al., in: Modern Nuclear Physics Methods for the Determination of the Elementary Composition of Rocks [in Russian], All-Union Scientific-Research Institute of Nuclear Geophysics and Geochemistry (1981), p. 136.
3. S. Amiel' and M. Peisakh, At. Energ., 14, No. 6, 535 (1963).
4. Instructions. Determiantion of Uranium by the Delayed Neutron Method [in Russian], All-Union Scientific-Research Institute of Metrology and Standardization, Moscow (1982).
5. Primary Processing of Analytical Data. Procedural Instruction No. 13 [in Russian], All-Union Scientific-Research Institute of Metrology and Standardization, Moscow (1977), p. 16.

ISOTOPIC COMPOSITION OF CESIUM BUILT UP IN VVÉR NUCLEAR FUEL

V. Ya. Gabeskiriya, V. I. Borisenkov,
V. V. Kalygin, V. M. Prokop'ev,
V. S. Prokopenko, M. N. Maslennikova,
and A. P. Chetverikov

UDC 621.039.516.22:621.039.524.4-98

Data about the content of fission products in spent nuclear fuels allows the parameters of the neutron spectrum to be established, and the fuel burnup and the buildup in it of nuclides of the actinide elements to be calculated [1–4]. At the same time, there are almost no data about the determination of the isotopic composition of the individual fission products built up in the fuel of Soviet power reactors. In the present paper, the results are given of measurement of the isotopic composition of cesium in the fuel of water-cooled/water-moderated reactors with pressurized water and boiling reactors (VVÉR 365, VVÉR-440, and VK-50).

The isotopic composition of cesium was determined in samples of spent nuclear fuel, cut out of fuel elements with a different burnup. The initial enrichment of the fuel in ^{235}U for the VVÉR-365 and the VK-50 amounted to 3%, and for the VVÉR-440 it was 3.6%.

The samples of spent fuel investigated were dissolved in a mixture of chloric and nitric acids with heating. After complete dissolution, separation of the cesium for mass-spectrographic analysis was carried out by the method of [5]. The isotopic composition was measured on MI-1311 and (redesigned) MI-1305 mass spectrometers; in the latter, a triple-ribbon ion source was used for generating the ion beam. The characteristics of the samples and the results of mass-spectrometric analysis obtained, recalculated to the time of burnup of the fuel-element assembly, are given in Table 1.

The ratio of the molar fractions $^{134}Cs/^{137}Cs$ depends on the depth of burnup, the irradiation time, and the hardness of the neutron spectrum. Measurement of this ratio by the γ-spectrometric method gives information about the fuel burnup for the investigation of spent

TABLE 1. Isotopic Composition of Cesium in Samples of VVÉR Spent Nuclear Fuel, %

Reactor	Sample	^{133}Cs	^{134}Cs	^{135}Cs	^{137}Cs	Burnup of uranium, kg/ton	No. of fuel-element assembly	Distance from base of fuel element, mm	Irradiation time, days
VVÉR-365	1	43,56±0,04	0,92±0,01	15,21±0,03	40,31±0,03	5,33±0,06	РП-3-198	2150	343
	2	45,41±0,21	1,47±0,22	10,74±0,06	42,38±0,21	9,50±0,30	РП-3-198	750	343
	3	45,38±1,12	1,17±0,13	12,38±0,94	41,07±0,75	7,34±0,13	РП-3-198	350	343
	4	42,94±0,19	3,18±0,13	11,75±0,05	42,13±0,22	21,07±0,20	РП-3-247	1250	852
	5	43,35±0,19	3,22±0,19	11,46±0,05	41,97±0,21	22,39±0,28	РП-3-247	1250	852
	6	42,31±0,28	1,51±0,09	17,56±0,24	38,61±0,28	12,93±0,41	РП-3-223	2310	1230
	7	41,82±0,24	4,41±0,04	11,23±0,07	42,54±0,13	31,9±0,5	РП-3-223	1250	1230
VVÉR-440	8	40,25±0,18	4,28±0,05	14,42±0,04	41,05±0,16	33,8±0,5	Р-3,6 №216	1625	1222
	9	41,74±0,30	4,48±0,10	12,48±0,21	41,30±0,03	37,7±0,6	Р-3,6 №216	1375	1222
VK-50	10	38,59±0,15	0,89±0,02	25,22±0,11	35,30±0,13	8,14±0,1'.	ЭК-5М №4	1800	1825
	11	39,93±0,27	2,01±0,03	20,21±0,26	37,85±0,48	17,6±0,4	ЭК-5М №4	1400	1825
	12	41,16±0,10	2,86±0,02	15,24±0,08	40,74±0,10	23,6±0,4	ЭК-5М №4	1000	1825
	13	41,36±0,21	2,46±0,02	15,48±0,10	40,70±0,21	25,6±0,6	ЭК-5М №4	600	1825
	14	41,68±0,05	2,02±0,02	16,37±0,03	39,93±0,11	22,7±0,5	ЭК-5М №4	200	1825

fuel-element assemblies by nondestructive methods. An analysis of the data given in Table 1 shows that for samples 7 and 8 of VVÉR-365 and VVÉR-440 fuel, with approximately equal burnup and irradiation time, the ratio of the molar fractions $^{134}Cs/^{137}Cs$ are almost equal, i.e., the neutron spectra of these reactors differ only insignificantly.

The characteristic special feature of the boiling reactor VK-50 is the reduction of the density of the neutron moderator over the height of the core and, as a consequence, the increased hardness of the spectrum. Therefore, the ratio $^{134}Cs/^{137}Cs$ to the value of the burnup for samples cut out of the VK-50 reactor fuel-element assemblies increases with increase of distance from the base of the fuel element to the point of sectioning of the fuel being investigated.

LITERATURE CITED

1. T. S. Zaritskaya, A. K. Kruglov, and A. P. Rudik, At. Energ., 50, No. 1, 36 (1981).
2. T. S. Zaritskaya, A. K. Kruglov, and A. P. Rudik, At. Energ., 52, No. 1, 60 (1982).
3. T. S. Zaritskaya and A. P. Rudik, At. Energ., 52, No. 5, 348 (1982).
4. B. A. Bibichev et al., At. Energ., 48, No. 5, 294 (1980).
5. G. Timofeev et al., J. Radioanal. Chem., 51, 2, 377 (1979).

SATURATION OF THE SURFACE LAYER OF CARBON DEVITRIFIED GLASS, BORON NITRIDE, AND QUARTZ GLASS WITH ION-IMPLANTED DEUTERIUM

V. V. Bandurko, V. V. Kulik,
A. A. Pisarev, and V. N. Tsyplakov

UDC 533.924

In order to solve a number of problems pertaining to the interaction of plasma with materials it is necessary to investigate processes of the trapping of hydrogen isotope ions bombarding the surface of a solid. It is of particular interest to study the interaction of plasma with material having a low atomic number since the energy losses of the plasma on the impurities of these materials are minimal.

In this paper we investigate the accumulation of deuterium implanted during ion bombardment into USB-15 carbon devitrified glass, boron nitride, and KI quartz glass. The trapping was studied on the basis of the detection of reverse deuterium gas liberation from the specimens during irradiation (re-emission curves) and during subsequent heating with the temperature rising with time (thermal desorption spectra). The specimens were bombarded at room temperature with monoenergetic deuterium ions possessing an energy of 5 and 7.5 keV per deuteron. The experimental procedure was described in detail in [1].

The radiation dose was measured by the ion current with suppression of the secondary electrons. In the experiments with dielectrics (boron nitride, quartz glass) in order to prevent the buildup of positive charge on the surface of the specimen during ion bombardment provision was made for autocompensation of the charge by thermoelectrons. The rate of gas liberation during and after irradiation was measured quantitatively. The measuring system was calibrated during irradiation of reference specimens under conditions when the trapping coefficient is zero and the measured gas liberation flux is identical with the known flux of bombarding ions.

The thermal desorption spectra of gas liberation during heating after irradiation (Fig. 1) are characterized by an indistinct fine structure which indicates that gas liberation occurs as a result of several processes. The temperature of the maximum gas liberation rate j upon heating much above room temperature is ~805°K for boron nitride, 810°K for quartz glass, and 850-1200°K for carbon devitrified glass. The values of the activation energy for freeing implanted deuterons, estimated by the technique of [2, 3], are ~155 kJ/mole for boron nitride, 165 kJ/mole for quartz glass, and 165-250 kJ/mole for carbon devitrified glass. Thus, the results of thermal desorption experiments indicate that the mobility of the implanted deuterium is low in all the materials. Measurement of the reverse gas liberation during irradiation makes it possible to calculate the number of trapped particles as a function of the radiation dose (Fig. 2). It is seen that the number N_0 of trapped particles increases with the dose N_d and approaches a value which characterizes the state of saturation of the material with implanted deuterium. The initial segments of all the curves correspond to total trapping of all incident ions (trapping coefficient equal to 1). Gas liberation is absent during irradiation at low doses and when the dose exceeds a certain critical value it begins to grow, approaching a value that corresponds to the escape of all implanted ions from the specimen back into the vacuum. When the irradiation stops, the rate of gas liberation rapidly falls off to zero. This indicates that the rate of thermal gas liberation is insignificant and the emergence of gas from the specimen during irradiation is determined by radiation-stimulated processes, whose rate increases with the accumulation of deuterium implanted into the material.

When the thermal desorption of implanted particles is small, the model of local mixing which has been verified on a number of materials [4, 5] can be used to describe the re-emission. The model assumes that at a low radiation dose the concentration of implanted deuterium increases in proportion to the radiation dose over the entire zone of ion deceleration.
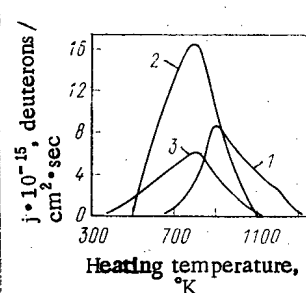
569

Fig. 1. Typical thermal desorption spectra of deuterium from materials bombarded with D_2^+ ions at 300°K (average heating rate ~7°K/sec: 1-3) carbon devitrified glass, boron nitride, quartz glass; deuterium dose $4 \cdot 10^{17}$, $7 \cdot 10^{17}$, and $3 \cdot 10^{17}$ cm^{-2}, respectively.
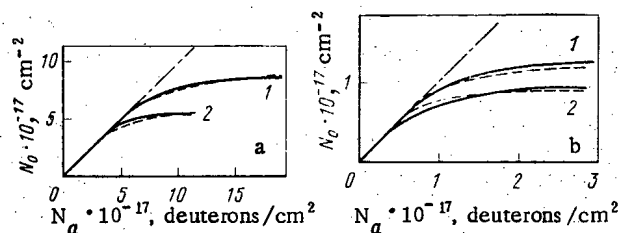

Fig. 2. Dose dependences of the number of particles trapped at 300°K and 15 keV during bombardment with deuterium ions: a) carbon devitrified glass (1) and boron nitride (2), 1 and 2 — D_2^+; b) quartz glass, 1 and 2 — D_2^+ and D_3^+; ———) experiment (error of determination of N_s is ±10%); -----) calculation; —•—•—) trapping efficiency 100%.

An increase in the concentration occurs only until a certain limiting value C_{max} is reached. It is assumed that if at some depth the concentration reached the maximum possible value, all the implanted particles which had stopped at that depth will not remain in the specimen and are released into the vacuum as a result of radiation-stimulated processes.

To calculate the number of implanted particles we used the deceleration profile $\varphi(x)$ in the form [6]

$$\varphi(x) = A \exp{[(x - \langle x \rangle)^2 / 2 \langle \Delta x^2 \rangle]},$$

where x is the depth, $\langle x \rangle$ is the mean projective range, $\langle \Delta x^2 \rangle = \left| \langle x^2 \rangle - \langle x \rangle^2 \right|$, $\langle x^2 \rangle$ is the mean square depth of penetration, and A is a normalization coefficient.

In the calculations for boron nitride and carbon devitrified glass we used experimentally determined values of the distribution parameters obtained during bombardment of graphite with deuterium ions: $\langle x \rangle = 110$ nm and $\sqrt{\langle \Delta x^2 \rangle} = 30$ nm for a deuteron energy of 7.5 keV [7-9]. The use of these parameters as applied to carbon devitrified glass and boron nitride is possible since the main component of carbon devitrified glass is carbon (85%) and boron nitride is characterized by approximately the same kind of parameters, determining the deceleration profile [10], as graphite does: average atomic number A = 6, atomic mass M = 12.4 amu, and atomic density $11.3 \cdot 10^{22}$ cm^{-3}. For quartz glass we used the theoretical values of the distribution parameters from [10]: $\langle x \rangle = 33$ nm and $\sqrt{\langle \Delta x^2 \rangle} = 21$ nm at a deuteron energy of 5 keV and $\langle x \rangle = 49$ nm, $\sqrt{\langle \Delta x^2 \rangle} = 27$ nm at a deuteron energy of 7.5 keV.

Using the expression above for the deceleration profile with the indicated parameters $\langle x \rangle$ and $\sqrt{\langle \Delta x^2 \rangle}$ we obtained the dependence $N_0(N_d)$ in the proposed local mixing model for a fixed value of C_{max}. Then, using C_{max} as a fitting parameter, we can attain satisfactory agreement between the calculated and experimental curves. It is seen from Fig. 2 that the experimental results are in good agreement with the calculated results for a maximum deuteron concentration $C_{max} = 7.3 \cdot 10^{22}$ cm^{-3} for carbon devitrified glass, $5.15 \cdot 10^{22}$ cm^{-3} for boron nitride, and $1.15 \cdot 10^{22}$ cm^{-3} for quartz glass. For quartz glass one value of C_{max} satisfies experiments carried out for two different ion energies.

In conclusion, we note that when carbon devitrified glass, boron nitride, and quartz glass are bombarded at room temperature with deuterium ions with an energy of 7.5 keV per deuteron practically all the incident ions are trapped in the specimen to doses of $4 \cdot 10^{17}$, $3.5 \cdot 10^{17}$, and $0.5 \cdot 10^{17}$ cm^{-2}, respectively. After these doses a reverse gas liberation appears and the state of saturation is gradually approached. As indicated by the results of experiments on gas liberation during irradiation and during heating after the irradiation, the mobility of the implanted **deuterons is insignificant** at room temperature. The accumulation of gas during implantation is described well by the model of local mixing with the values of the maximum attainable concentration of ion-implanted deuterium $7.3 \cdot 10^{22}$, $5.15 \cdot 10^{22}$, and $1.15 \cdot 10^{22}$ cm^{-3}, respectively, for carbon devitrified glass, boron nitride, and quartz glass.

LITERATURE CITED

1. A. A. Pisarev and V. N. Tsyplakov, At. Energ., 57, No. 2, 104 (1984).
2. A. A. Pisarev and V. A. Pisarev, At. Energ., 37, No. 4, 340 (1974).
3. L. B. Begrambekov et al., At. Energ., 31, No. 6, 625 (1971).
4. B. Doyle et al., J. Nucl. Mater., 93/94, 551 (1980).
5. S. Cohen and G. McCracken, J. Nucl. Mater., 84, 157 (1979).
6. Yu. V. Martynenko, Itogi Nauki i Tekhniki, Fiz. Plazmy, 3, 119 (1982).
7. R. Langley and R. Blewer, J. Nucl. Mater., 76/77, 313 (1978).
8. J. Roth et al., J. Nucl. Mater., 93/94, 601 (1980).
9. B. Scherzer et al., J. Nucl. Mater., 63, 100 (1976).
10. A. F. Burenkov et al., in: Tables of Parameters of Spatial Distribution of Ion-Implanted Impurities [in Russian], Belorussian State Univ., Minsk (1980), p. 352.

YIELDS OF ^{42}K AND ^{43}K UPON IRRADIATION OF CALCIUM BY

PROTONS AND DEUTERONS

P. P. Dmitriev and M. V. Panarin

Of the two long-lived radioisotopes of potassium ^{42}K ($T_{1/2}$ = 12.36 h) and ^{43}K ($T_{1/2}$ = 22.6 h), the most widely used in nuclear medicine is ^{43}K. It is necessary when choosing the method of producing ^{43}K to know the yields of ^{42,43}K. The method of producing ^{43}K by the reaction ^{40}Ar(αp)^{43}K is well known. An argon gas target for producing ^{43}K has been described in [1], and the dependence of the ^{43}K and ^{42}K yields on the α-particle energy has been measured for a thick argon target. For E_α = 17 MeV the ^{43}K yield is equal to 2330 kBq/μA·h, and the admixture of ^{42}K formed by the reaction ^{40}Ar(αpn)^{42}K amounts to 8-10%. A ^{43}K yield of 2220 kBq/μA·h has been obtained at E_α = 21 MeV in [2] for a similar gaseous target.

The ^{42}K and ^{43}K yields are measured in this paper as a function of the proton and deuteron energy for a thick calcium target. Samples of metallic calcium were irradiated in the deflected beam of the Physicopower Institute cyclotron (Obninsk). The ^{42,43}K yields were measured for six values of the particle energy. When calcium is irradiated by protons and deuterons, the radioisotopes ^{43,44m,46,47,48}Sc with half-lives from 3.89 h to 83.8 days are formed with an appreciable yield, which complicates the measurement of the activity of ^{42,43}K in the irradiated samples. Therefore, we radiochemically isolated ^{42,43}K from the irradiated samples, identified these isotopes from their γ-radiation and half-life, and measured their activity by the number of pulses in the photopeak of the selected γ-line. The following values of the γ-photon yield from [3] were used: ^{42}K (1525 keV; 17.9%) and ^{43}K (617.2 keV; 71.8%). The procedure for measurement of the activity of the isotopes and the integrated irradiation current of the samples is similar to that described in [1].

The measurement results for the yields are given in Fig. 1 and in Table 1. The errors in the values of the yields (15-16%) are caused mainly by systematic errors in measurements of the activity of ^{42,43}K and the integrated irradiation current of the samples as well as by the error in determination of the percentage of radiochemical isolation of ^{42,43}K from the irradiated samples.
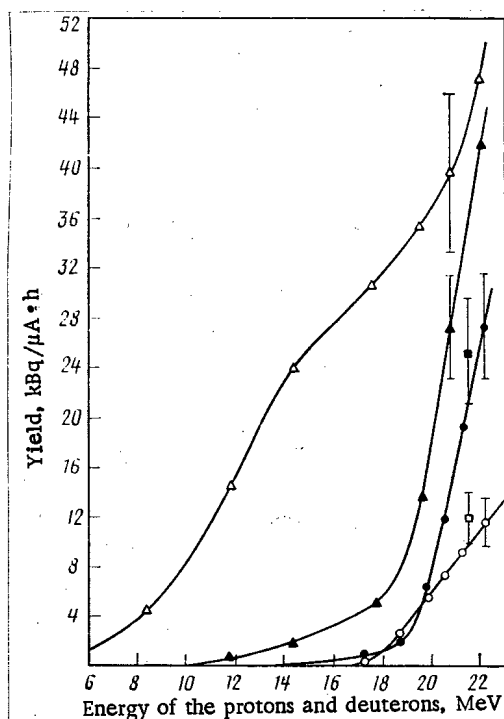
Fig. 1. Yields of ^{42}K and ^{43}K upon irradiation of thick calcium targets by protons and deuterons. This paper: ●) Ca + p → ^{43}K; ○) Ca + p → ^{42}K; ▲) Ca + d → ^{43}K; △) Ca + d → ^{42}K (:10 times); Ref. 5: ■) ^{44}Ca (p 2p) ^{43}K; ⊡) ^{43}Ca (p 2p) ^{42}K.

TABLE 1. Yields of ^{43}K and ^{42}K

Radioisotope	Production reaction*	Energy threshold of the reaction, MeV	Content of original isotope, %	Particle energy, MeV	Yield, kBq/μA·h	Remark
^{43}K	^{44}Ca (p 2p)	12,45	2,13	22,2±0,3	27±4	a†
	^{46}Ca (pα)	1,72	0,003	21,5	25±4	b‡
	^{48}Ca (pα 2n)	18,91	0,177			
^{42}K	^{43}Ca (p 2p)	10,92	0,13	22,2±0,3	11,5±1,7	a
	^{44}Ca (p 2p n)	22,3	2,13	21,5	11,8±1,9	b
	^{46}Ca (pα)	11,57	0,003			
^{43}K	^{43}Ca (d 2p)	3,41	0,13	22,1±0,3	42±7	a
	^{44}Ca (d 2p n)	15,05	2,13			
	^{46}Ca (dαn)	4,08	0,003			
^{42}K	^{42}Ca (d 2p)	5,2	0,64	22,1±0,3	470±70	a
	^{43}Ca (d 2p n)	13,2	0,13			
	^{44}Ca (dα)	0	2,13			
	^{46}Ca (dα 2n)	14,14	0,003			

*Reactions of the type (p ^{3}He) and (d ^{3}He) are not given in view of their relatively low cross sections (for example, see [7]).
†Data of this paper (a).
‡Estimate of the yield from the cross section of the (p 2p) reaction with E_p = 21.5 MeV (b).

One paper [5] has been published in all in which the cross sections of ^{43}Ca(p 2p)^{42}K and ^{44}Ca(p 2p)^{43}K reactions, in which ^{42,43}K is formed from calcium with E_p = 21.5 MeV, are measured: 7 ± 1 and 2 ± 0.3 mb, respectively (1 b = 10^{-28} m^2). The effective thresholds of these reactions estimated from the formula given in [6] are approximately 16.5 and 18 MeV,

respectively. In order to **estimate** the yields of ^{42}K and ^{43}K for a thick target from the cross sections indicated above, it was assumed that the cross section of these reactions increases linearly from the effective threshold of the reaction to E_p = 21.5 MeV. Upon integration over the range of the excitation functions obtained for these reactions the values of the yield of ^{42}K and ^{43}K for E_p = 21.5 MeV are as shown in Table 1 and on **Fig. 1**.

Upon the irradiation of natural calcium the ^{43}K yield is small in comparison with the irradiation of argon, and the admixture of ^{42}K is very appreciable. The situation is radically altered when enriched ^{44}Ca is used. For example, the irradiation by protons of calcium enriched in ^{44}Ca to 95% increases the yield of ^{43}K by a factor of 45, and the content of the ^{43}K impurity decreases by a factor of 100–200 (depending on the ^{43}Ca content in the enriched ^{44}Ca). Upon irradiation of natural calcium by deuterons the contribution, according to our estimates, of the reaction ^{44}Ca(d2pn)^{43}K to the ^{43}K yield amounts to ~70% (with E_d = 22 MeV). Therefore, when enriched ^{44}Ca is irradiated, one can expect an increase of the ^{43}K yield by approximately a factor of 30.

The admixture of ^{42}K due to the reaction ^{44}Ca(dα)^{42}K can be reduced by using a thin target. Thus when a target of enriched ^{44}Ca is used, the ^{43}K yield and the content of the ^{42}K impurity are comparable to the analogous characteristics of the target (Ar + α) → ^{42,43}K. The well-known difficulties associated with the creation and operation of a gaseous target are eliminated. Recording of the ^{44}Ca from the irradiated targets for repeated irradiation will permit reducing the cost of using enriched ^{44}Ca.

LITERATURE CITED

1. J. Clark et al., Int. J. Appl. Rad. Isotopes, 23, 329 (1972).
2. M. Guillaume, Nucl. Instrum. Methods, 131, 185 (1976).
3. N. G. Gusev and P. P. Dmitriev, Quantum Radiation of Radioactive Nuclides (Handbook) [in Russian], Atomizdat, Moscow (1977).
4. P. P. Dmitriev et al., At. Energ., 46, No. 3, 185 (1979); 48, No. 2, 122 (1980); 48, No. 6, 402 (1980).
5. B. Cohen and E. Newman, Phys. Rev., 99, 723 (1955).
6. P. P. Dmitriev and M. V. Panarin, At. Energ., 46, No. 1, 53 (1979).
7. D. Williams and J. Irvine, Phys. Rev., 130, 259 (1963).

IMPLANTATION OF LOW-ENERGY HYDROGEN IONS IN LITHIUM

O. G. Voronkov, V. F. Zubarev,
and L. M. Frantseva

The possibility of using liquid lithium in controlled thermonuclear fusion systems for pumping large fluxes of nonthermal atoms and ions of hydrogen isotopes (having an energy in excess of tens of electron volts) by means of the implantation method was examined in [1–5]. The possibility of implantation of hydrogen ions with an energy above 2.5 keV per proton in liquid lithium can be considered as an experimentally established fact [1, 5]. However, this was not checked experimentally in the case of lower energies. We have attempted here to gain information on the implantation of hydrogen ions in lithium at an energy of 1.5 keV per proton. For work at energies below 3 keV, we had to modify the existing ion source [5]. This was necessary because, on the one hand, a reduction in the accelerating voltage causes a reduction in the optimum ion current to the target (i.e., the ion current corresponding to a minimal angular divergence), and, thus, a sensitivity loss in measuring the implantation factor, while, on the other hand, a low accelerating voltage produces a smaller discharge current in the source plasma, so that optimum focusing occurs under conditions of unstable arcing .[6]. These disadvantages are eliminated to a considerable degree by a source design incorporating an expansion chamber (expander) [7] and a small accelerating gap [6], which is shown in Fig. 1.

The plasma formed in the arc discharge between the lanthanum–hexaboride heating cathode 1, and the walls of the discharge chamber 2, emerges through the opening in anode 3. The an-
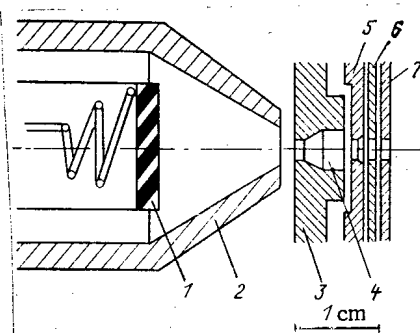
Fig. 1. Schematic diagram of the
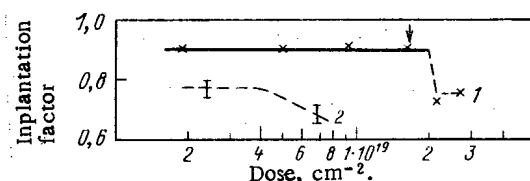ion source for producing low-energy
beams.

Fig. 2. Factor of hydrogen ion implantation in lithium as a
function of the proton dose (ion energy, 1.5 keV per proton):
————) and -----) implantation in liquid and solid lithium,
respectively. 1) Initial lithium temperature, 230°C; final
temperature, 130°C (the arrow indicates the time the heating
was switched off); 2) lithium temperature, 20°C.

ode ends with an expansion chamber, 4 [6]. The voltage between the anode 3 and the emission
lens 5 is equal to 200-400 V. The emerging ion beam is focused by an intermediate lens 6 (to
which a negative potential is applied) and the ground electrode 7. The accelerating voltage,
which determines the ion energy, is supplied to anode 3. The shape and dimensions of the ex-
pansion chamber are designed to ensure the plasma density at the exit opening of the emission
lens necessary for sharp beam focusing with stable arcing in chamber 2. The spacings between
lenses 5, 6, and 7 and their thicknesses were determined on the basis of the recommendations
given in [7]. We succeeded in providing an accelerating gap of 0.4-0.5 mm between the elec-
trodes.

As a result of additional focusing along the beam channel [5], such an ion source design
made it possible to produce, at a target located at 1.3 m from the source, H_2^+ ion currents of
up to 70-90 µA with an energy of 3 keV and a spot area of 0.1 cm^2. The surface area of the
spot was determined by visually observing the luminescence of quartz glass covered with a
molybdenum grid and measuring the surface area of the ionic etching spot on a stainless-steel
mobile slide, placed in the immediate vicinity of the target.

The procedure of filling the target with lithium and the method of measuring the implan-
tation factor have been described in [5]. The lithium target design was modified so as to re-
move the lithium crucible heaters from the vacuum and bring them out into the atmosphere. This
made it possible to reduce by almost one order of magnitude the background pressure in the
measuring chamber with the crucible heated to 250-300°C. The chamber walls remained cold. An
improved system for stabilizing the accelerating voltage and the separator magnet current main-
tained during prolonged irradiation the stability of the spot position on the target with an
accuracy not worse than 10% of the spot area.

The experiments were performed at 200-250°C with a current density of 0.5-0.9 mA/cm^2 and
a H_2^+ ion energy of 3 keV, which corresponded to the injection of protons with an energy of 1.5
keV [8]. The implantation was carried out in liquid, setting, and cold (room temperature)
lithium. The lithium pressed out into the crucible had a mirror surface and did not require
additional cleansing by scraping. The thickness of the lithium layer in the crucible amounted
to a few millimeters. A positive voltage (40-70 V) with respect to ground was applied to the
target in order to suppress secondary electron emission from the lithium surface.

574

A typical dependence of the implantation factor on the irradiation dose during one measurement cycle is shown in Fig. 2. The dose was calculated with respect to the target current, which remained constant, and the irradiation time, with an allowance for the number of protons per incident ion. At the points marked on the curve, the complete procedure of measuring the implantation factor was carried out by using the molybdenum slide [5]. In the intervals between these measurements, implantation was estimated with respect to the steadiness of the pressure rise in the chamber, caused by desorption from irradiated lithium, and the constancy of the beam current to the target.

When the proton irradiation dose reaches $\sim 2 \cdot 10^{19}$ cm^{-2}, the target heating is switched off, and lithium starts to cool under continued irradiation. The irradiation is stopped when the lithium temperature drops to 130°C, which is considerably below the crystallization temperature. The time of lithium crystallization is recorded with respect to the temperature, with respect to the increasing pressure rise in the chamber, and visually.

It is evident that implantation in liquid lithium occurs with constant efficiency and is independent of the temperature up to the melting point. After crystallization, the implantation factor drops sharply to 0.7-0.75. Implantation in cold (20°C) lithium occurs at the same level. After solidification, the metal surface changes from a shiny one to a dull, rough surface, and, as the ion beam is moved over the surface of solid lithium, it is possible to obtain implantation factors which differ by 0.1-0.15 from each other. This is possibly connected with ion reflection at glancing angles with respect to the roughnesses. The factor of hydrogen ion implantation in a "thick" liquid lithium film in the range from the melting point (180°C) to 250°C remains high, 0.9-0.94, for proton doses not lower than $2 \cdot 10^{19}$ cm^{-2}.

The authors are grateful to A. A. Panasenkov and Yu. M. Pustovoit for the useful consultations and their help.

LITERATURE CITED

1. S. Erents, G. McCracken, and P. Goldsmith, J. Phys. D. Appl. Phys., 4, 672 (1971).
2. B. Badger et al., UWFDM-68, Nucl. Eng. Dept., Univ. of Wisconsin (1974).
3. B. Badger et al., UWFDM-112, Nucl. Eng. Dept., Univ. of Wisconsin (1975).
4. E. V. Murav'ev, Vopr. At. Nauki Tekh., Ser. Termoyadernyi Sintez, No. 2 (6), 57 (1980).
5. O. G. Voronkov and V. F. Zubarev, in: Reports at the Second All-Union Conference on Engineering Problems Concerning Thermonuclear Reactors [in Russian], Vol. 4, NIIÉFA, Leningrad (1981), p. 217.
6. J. Copeland et al., Prib. Nauchn. Issled., No. 9, 101 (1973).
7. Th. Slyuters, in: Proc. Second Int. Conf. on Ion Sources, Vienna (1972), p. 190.
8. G. McCracken and J. Maple, Brit. J. Appl. Phys., 18, 919 (1967).

MEASUREMENT TECHNIQUES
Izmeritel'naya Tekhnika
Vol. 27, 1984 (12 issues) $520

MECHANICS OF COMPOSITE MATERIALS
Mekhanika Kompozitnykh Materialov
Vol. 20, 1984 (6 issues) $430

METAL SCIENCE AND HEAT TREATMENT
Metallovedenie i Termicheskaya Obrabotka Metallov
Vol. 26, 1984 (12 issues) $540

METALLURGIST
Metallurg
Vol. 28, 1984 (12 issues) $555

PROBLEMS OF INFORMATION TRANSMISSION
Problemy Peredachi Informatsii
Vol. 20, 1984 (4 issues) $420

PROGRAMMING AND COMPUTER SOFTWARE
Programmirovanie
Vol. 10, 1984 (6 issues) $175

PROTECTION OF METALS
Zashchita Metallov
Vol. 20, 1984 (6 issues) $480

RADIOPHYSICS AND QUANTUM ELECTRONICS
Izvestiya Vysshikh Uchebnykh Zavedenii, Radiofizika
Vol. 27, 1984 (12 issues) $520

REFRACTORIES
Ogneupory
Vol. 25, 1984 (12 issues) $480

SIBERIAN MATHEMATICAL JOURNAL
Sibirskii Matematicheskii Zhurnal
Vol. 25, 1984 (6 issues) $625

SOIL MECHANICS AND FOUNDATION ENGINEERING
Osnovaniya, Fundamenty i Mekhanika Gruntov
Vol. 21, 1984 (6 issues) $500

SOLAR SYSTEM RESEARCH
Astronomicheskii Vestnik
Vol. 18, 1984 (6 issues) $365

SOVIET APPLIED MECHANICS
Prikladnaya Mekhanika
Vol. 20, 1984 (12 issues) $520

SOVIET ATOMIC ENERGY
Atomnaya Energiya
Vols. 56-57, 1984 (12 issues) $560

SOVIET JOURNAL OF GLASS PHYSICS AND CHEMISTRY
Fizika i Khimiya Stekla
Vol. 10, 1984 (6 issues) $235

SOVIET JOURNAL OF NONDESTRUCTIVE TESTING
Defektoskopiya
Vol. 20, 1984 (12 issues) $615

SOVIET MATERIALS SCIENCE
Fiziko-khimicheskaya Mekhanika Materialov
Vol. 20, 1984 (6 issues) $445

SOVIET MICROELECTRONICS
Mikroėlektronika
Vol. 13, 1984 (6 issues) $255

SOVIET MINING SCIENCE
Fiziko-tekhnicheskie Problemy Razrabotki Poleznykh Iskopaemykh
Vol. 20, 1984 (6 issues) $540

SOVIET PHYSICS JOURNAL
Izvestiya Vysshikh Uchebnykh Zavedenii, Fizika
Vol. 27, 1984 (12 issues) $520

SOVIET POWDER METALLURGY AND METAL CERAMICS
Poroshkovaya Metallurgiya
Vol. 23, 1984 (12 issues) $555

STRENGTH OF MATERIALS
Problemy Prochnosti
Vol. 16, 1984 (12 issues) $625

THEORETICAL AND MATHEMATICAL PHYSICS
Teoreticheskaya i Matematicheskaya Fizika
Vol. 58-61, 1984 (12 issues) $500

UKRAINIAN MATHEMATICAL JOURNAL
Ukrainskii Matematicheskii Zhurnal
Vol. 36, 1984 (6 issues) $500

Send for Your Free Examination Copy

PEEL HER

RUSSIAN JOURNALS IN THE PHYSICA
AND MATHEMATICAL SCIENCES

AVAILABLE IN ENGLISH TRANSLATION

ALGEBRA AND LOGIC
Algebra i Logika
Vol. 23, 1984 (6 issues) $360

ASTROPHYSICS
Astrofizika
Vol. 20, 1984 (4 issues) $420

AUTOMATION AND REMOTE CONTROL
Avtomatika i Telemekhanika
Vol. 45, 1984 (24 issues) $625

COMBUSTION, EXPLOSION, AND SHOCK WAVES
Fizika Goreniya i Vzryva
Vol. 20, 1984 (6 issues) $445

COSMIC RESEARCH
Kosmicheskie Issledovaniya
Vol. 22, 1984 (6 issues).......................... $545

CYBERNETICS
Kibernetika
Vol. 20, 1984 (6 issues).......................... $445

DIFFERENTIAL EQUATIONS
Differentsial'nye Uravneniya
Vol. 20, 1984 (12 issues) $505

DOKLADY BIOPHYSICS
Doklady Akademii Nauk SSSR
Vols. 274-279, 1984 (2 issues) $145

FLUID DYNAMICS
Izvestiya Akademii Nauk SSSR,
Mekhanika Zhidkosti i Gaza
Vol. 19, 1984 (6 issues) $500

FUNCTIONAL ANALYSIS AND
ITS APPLICATIONS
Funktsional'nyi Analiz i Ego Prilozheniya
Vol. 18, 1984 (4 issues) $410

GLASS AND CERAMICS
Steklo i Keramika
Vol. 41, 1984 (6 issues) $590

HIGH TEMPERATURE
Teplofizika Vysokikh Temperatur
Vol. 22, 1984 (6 issues) $520

HYDROTECHNICAL CONSTRUCTION
Gidrotekhnicheskoe Stroitel'stvo
Vol. 18, 1984 (12 issues) ....

INDUSTRIAL LABORATORY
Zavodskaya Laboratoriya
Vol. 50, 1984 (12 issues) ....

INSTRUMENTS AND
EXPERIMENTAL TECHNIQUES
Pribory i Tekhnika Éksperimenta
Vol. 27, 1984 (12 issues) ....

JOURNAL OF APPLIED MECHANICS
AND TECHNICAL PHYSICS
Zhurnal Prikladnoi Mekhaniki i Tekhnicheskoi Fiziki
Vol. 25, 1984 (6 issues) $540

JOURNAL OF APPLIED SPECTROSCOPY
Zhurnal Prikladnoi Spektroskopii
Vols. 40-41, 1984 (12 issues) $540

JOURNAL OF ENGINEERING PHYSICS
Inzhenerno-fizicheskii Zhurnal
Vols. 46-47, 1984 (12 issues) $540

JOURNAL OF SOVIET LASER RESEARCH
A translation of articles based on the best Soviet research in the field of lasers
Vol. 5, 1984 (6 issues) $180

JOURNAL OF SOVIET MATHEMATICS
A translation of Itogi Nauki i Tekhniki and Zapiski Nauchnykh Seminarov Leningradskogo Otdeleniya Matematicheskogo Instituta im. V. A. Steklova AN SSSR
Vols. 24-27, 1984 (24 issues)........................ $1035

LITHOLOGY AND MINERAL RESOURCES
Litologiya i Poleznye Iskopaemye
Vol. 19, 1984 (6 issues) $540

LITHUANIAN MATHEMATICAL JOURNAL
Litovskii Matematicheskii Sbornik
Vol. 24, 1984 (4 issues) $255

MAGNETOHYDRODYNAMICS
Magnitnaya Gidrodinamika
Vol. 20, 1984 (4 issues) $415

MATHEMATICAL NOTES
Matematicheskie Zametki
Vols. 35-36, 1984 (12 issues)........................ $520